



RESEARCH ARTICLE

10.1029/2021JG006660

Key Points:

- Silicon isotope ratios of storm events within small catchments demonstrate site-specific biogeochemical and hydrological signatures
- Cross-site behavior was successfully described using a model combining fluid transit time distributions and multiple fractionation pathways
- Site-specific critical zone architecture remains the main control over stream silicon export signatures even under extreme precipitation conditions

Supporting Information:

Supporting Information may be found in the online version of this article.

Correspondence to:

N. M. Fernandez,
n.fernandez@cornell.edu

Citation:

Fernandez, N. M., Bouchez, J., Derry, L. A., Chorover, J., Gaillardet, J., Giesbrecht, I., et al. (2022). Resiliency of silica export signatures when low order streams are subject to storm events. *Journal of Geophysical Research: Biogeosciences*, 127, e2021JG006660. <https://doi.org/10.1029/2021JG006660>

Received 7 OCT 2021

Accepted 12 APR 2022

Author Contributions:

Conceptualization: J. Bouchez, J. L. Druhan
Data curation: L. A. Derry, J. Chorover, J. Gaillardet
Formal analysis: N. M. Fernandez
Funding acquisition: L. A. Derry, J. Chorover, J. Gaillardet
Investigation: N. M. Fernandez, J. Bouchez, J. L. Druhan
Methodology: N. M. Fernandez, J. Bouchez, J. L. Druhan
Project Administration: J. Chorover
Resources: L. A. Derry, J. Chorover, J. Gaillardet, I. Giesbrecht, D. Fries

© 2022, The Authors.

This is an open access article under the terms of the [Creative Commons Attribution License](#), which permits use, distribution and reproduction in any medium, provided the original work is properly cited.

Resiliency of Silica Export Signatures When Low Order Streams Are Subject to Storm Events

N. M. Fernandez^{1,2} , J. Bouchez³ , L. A. Derry^{2,3} , J. Chorover⁴ , J. Gaillardet³ , I. Giesbrecht^{5,6} , D. Fries⁷ , and J. L. Druhan^{1,3}

¹Department of Geology, University of Illinois at Urbana Champaign, Urbana, IL, USA, ²Department of Earth and Atmospheric Sciences, Cornell University, Ithaca, NY, USA, ³Université de Paris, Institut de Physique du Globe de Paris, CNRS, Paris, France, ⁴Department of Environmental Science, University of Arizona, Tucson, AZ, USA, ⁵Hakai Institute, Tula Foundation, Vancouver, BC, Canada, ⁶School of Resource and Environmental Management, Simon Fraser University, Burnaby, BC, Canada, ⁷School of Ocean and Earth Science, National Oceanography Centre Southampton, University of Southampton Waterfront Campus, Southampton, UK

Abstract Silicon stable isotope ratios ($\delta^{30}\text{Si}$) of over 150 stream water samples were measured during seven storm events in six small critical zone observatory (CZO) catchments spanning a wide range in climate (sub-humid to wet, tropical) and lithology (granite, volcanic, and mixed sedimentary). Here we report a cross-site analysis of this dataset to gain insight into stream $\delta^{30}\text{Si}$ variability across low-order catchments and to identify potential climate (i.e., runoff), hydrologic, lithologic, and biogeochemical controls on observed stream Si chemical and isotopic signatures. Event-based $\delta^{30}\text{Si}$ exhibit variability both within and across sites (−0.22‰ to +2.27‰) on the scale of what is observed globally in both small catchments and large rivers. Notably, each site shows distinct $\delta^{30}\text{Si}$ signatures that are preserved even after normalization for bedrock composition. Successful characterization of observed cross-site behavior requires the merging of two distinct frameworks in a novel combined model describing both non-uniform fluid transit time distributions and multiple fractionating pathways in application to low-order catchments. The combined model reveals that site-specific architecture (i.e., biogeochemical reaction pathways and hydrologic routing) regulates stream silicon export signatures even when subject to extreme precipitation events.

Plain Language Summary Periods of intense infiltration in the form of rainfall (storm events) or snowmelt push large volumes of dilute fluid through catchments, resulting in evacuation of dissolved solutes derived from weathering reactions. These events occur over short (daily or weekly) timescales, but these pulses of solutes released into small streams can represent a majority of total annual mass flux (from 40% to 70%). Despite their importance, storm events remain largely underrepresented in studies of weathering in watersheds due to challenges in obtaining high frequency measurements. Yet extreme events are expected to become more frequent in the future in response to a changing climate. In this study, we evaluate the dependence of weathering-derived solute export on hydrology and biogeochemical cycling through measurements of dissolved silicon and silicon stable isotope ratios of stream waters collected during seven significant infiltration events in six small catchments spanning different bedrock lithology and climates. Each catchment was found to have unique silicon chemical and isotopic export signatures reflecting site-specific subsurface water routing and combination of biogeochemical reactions. These signatures were found to be preserved despite the perturbation exerted by such enhanced infiltration and discharge. In this sense, catchments exhibit resilience, bending but not ceding to strong hydrologic forcing.

1. Introduction

Silicate weathering is a critical facet of Earth's surface dynamics, transforming and mobilizing mass to shape landscapes, supplying essential nutrients to a diversity of ecosystems, and regulating Earth's climate over geologic timescales through the drawdown of atmospheric CO₂. A principal objective of modern Critical Zone (CZ) science is to better constrain the ensemble of (bio)geochemical, climate (temperature, runoff, precipitation), and lithologic controls driving silicate weathering rates. Evaluating these factors, notably those that are climate-related (such as runoff and precipitation), has proven to be a difficult task due to strong coupling between physical and chemical erosion rates (Millot et al., 2002; Riebe et al., 2001, 2003; West et al., 2005) and first-order lithologic controls (Amiotte Suchet et al., 2003; Bluth & Kump, 1994; Garrels & MacKenzie, 1971; Meybeck, 1987). In

Supervision: J. Bouchez, J. L. Druhan
Visualization: N. M. Fernandez
Writing – original draft: N. M. Fernandez, J. Bouchez, J. L. Druhan
Writing – review & editing: N. M. Fernandez, J. Bouchez, J. Chorover, I. Giesbrecht, D. Fries, J. L. Druhan

this respect, the study of small, upland catchments hosting low-order streams offers an important opportunity to identify climate controls on silicate weathering. Low-order catchments are considered important silicate weathering “hotspots” (Bluth & Kump, 1994; Drever & Clow, 1995; Drever & Zobrist, 1992; McClain et al., 2003; Millot et al., 2002; Oliva et al., 2003; Stallard, 1985; Stallard & Edmond, 1983, 1987; White & Blum, 1995; White et al., 1999), while their size ($<100 \text{ km}^2$), generally homogenous lithology, and less diverse hydrologic characteristics makes them relatively simple systems (relative to higher order watersheds). Further, high physical erosion rates typically associated with small catchments (Dixon et al., 2009; Riebe et al., 2001; West et al., 2005) ensure a steady supply of fresh weatherable material accessible to meteoric fluids in the weathering zone, promoting and sustaining silicate weathering. In such a kinetically limited geomorphic regime (Riebe et al., 2017), (bio) geochemical reactivity and climate factors are the main drivers of silicate weathering rates, regulating both water delivery to the weathering zone and the extent of weathering reactions as dictated by kinetic and thermodynamic limitations (Maher, 2011).

Strong dependence on climate and hydrology implies that transient hydrologic events (“hot moments”, “storm events” or periods of high variability in discharge; McClain et al., 2003) should play a major role in small catchment silicate weathering fluxes. Indeed, storm events have been shown to disproportionately affect solute generation and transport dynamics at the catchment scale, constituting 40% to as high as 80% of the total annual rainfall and solute export fluxes (Larsen & Simon, 1993; Moatar et al., 2020; Raymond & Sayers, 2010; Yoon & Raymond, 2012). However, storm events are notoriously underrepresented in the geochemical literature due to challenges in high-frequency sampling; an area that has only recently seen significant progress with technological advancements like the River Lab (ExtraLab®, Floury et al., 2017). Such scarcity of high-resolution event data may have substantial consequences for our estimations of silicate weathering rates, which are determined primarily from long-term, low frequency (annual or seasonal) samples (Oliva et al., 2003; White & Blum, 1995). For example, a study of silica cycling dynamics in Siberian watersheds found spring flooding to account for 60–80% of annual silica export fluxes (Pokrovsky et al., 2013). Missing such hot moments could result in a significant under-estimation of observed silicate weathering rates. Further, while tracer evidence shows that the biogeochemical pathways that produce weathering-derived solutes can change during these hydrologic events, there is still much to learn about how these processes change with varying hydrologic pathways and transit times (Arora et al., 2020; Benettin, Bailey, et al., 2017; Cenki-Tok et al., 2009; Derry et al., 2005; Kurtz et al., 2011; Rose et al., 2018). Finally, the large fraction of the annual dissolved solute riverine budget represented in storm events strongly links these moments to long-term silicate weathering behavior, a connection that has been implied in recent studies (Knapp et al., 2020; Minaudo et al., 2019; Rose et al., 2018).

From this basis it becomes clear that storm events provide a unique opportunity to evaluate the relationship between silicate weathering and catchment hydrology. Activation of quiescent water stores and reaction pathways during these intensive drainage events offers a unique glimpse into silicate weathering dynamics within a catchment and the interplay between various water stores, biological cycling, and residence times contributing to observed stream chemistry (Dwivedi et al., 2018; McIntosh et al., 2017; White et al., 2019; Zapata-Rios et al., 2015). Stream solute concentration (C)-discharge (Q) relationships serve as an effective tool to decipher these internal catchment solute dynamics. However, the seemingly infinite combinations of hydrologic and (bio) geochemical pathways, mixing and storage mechanisms that can be invoked to generate equivalent observations complicates interpretation of stream chemical signals when total element concentrations are solely relied upon. This is consistent with longstanding observations and models illustrating low variance in geogenic solute concentrations across a large range of discharge rates (e.g., Anderson et al., 1997; Davis, 1964; Godsey et al., 2009; Kennedy, 1971; Scanlon et al., 2001). Such challenges can be alleviated through the complementary use of geochemical tools such as stable isotope ratios of weathering-derived elements (i.e., Li, Mg, Ca, B, Si, Fe, Cu, and Zn) that offer precise source signatures as well as indicators of the type and extent of biogeochemical reactions actively involved in solute cycling (Wiederhold, 2015). Silicon stable isotope ratios (denoted here as $\delta^{30}\text{Si}$) offer such diagnostics for the second most abundant element in Earth’s crust and are used frequently to infer and quantify solute fluxes associated with silicate weathering (Cardinal et al., 2010; Georg et al., 2006a, 2007, 2009; Hughes et al., 2011, 2012, 2013; Opfergelt & Delmelle, 2012; Pokrovsky et al., 2013; Riotti et al., 2018, etc.). Silicon stable isotopes can be fractionated by biological uptake, secondary mineral precipitation and adsorption reactions, thereby providing constraints on the relative contributions of these secondary processes to overall solute fluxes. Silicon stable isotopic shifts (${}^{30}\varepsilon = 10^3(\alpha - 1)$, Coplen, 2011) associated with these Critical Zone processes typically vary on the order of $-3.5\text{\textperthousand}$ (amorphous silica precipitation, Fernandez et al., 2019; Roerdink

et al., 2015) to $-0.33\text{\textperthousand}$ (uptake by vascular plants, Frick et al., 2020). Likewise, globally observed river $\delta^{30}\text{Si}$ values exhibit variability of $\sim 5\text{\textperthousand}$ (Frings et al., 2016) and are typically enriched in ^{30}Si relative to the bedrock and primary minerals comprising the surrounding lithology (De La Rocha et al., 2000; Ding et al., 2004; Georg et al., 2006a).

Those studies that have focused on temporal variation in riverine $\delta^{30}\text{Si}$ generally observe a decrease in dissolved Si and associated $\delta^{30}\text{Si}$ in rivers during periods of high discharge (Engström et al., 2010; Georg et al., 2006a; Pokrovsky et al., 2013; Riotte et al., 2018; Steinhoefel et al., 2017). Of these studies, none specifically targeted storm events and only two generated temporally resolved datasets to monitor seasonal variations in river $\delta^{30}\text{Si}$ (Engström et al., 2010; Pokrovsky et al., 2013). Seasonal stream $\delta^{30}\text{Si}$ variability from these efforts agreed with those observed globally, from $0.8\text{\textperthousand}$ (Engström et al., 2010) to $1.0\text{\textperthousand}$ – $1.5\text{\textperthousand}$ (Pokrovsky et al., 2013). To explain observed stream $\delta^{30}\text{Si}$ behavior as a function of discharge several of these studies (Engström et al., 2010; Georg et al., 2006a; Pokrovsky et al., 2013) have invoked a combination of rapid weathering reactions, notably *in situ* dissolution of low $\delta^{30}\text{Si}$ clay fractions in suspended sediments within streams, and two-component mixing between a high $\delta^{30}\text{Si}$, enriched dissolved Si soil/groundwater reservoir and a low $\delta^{30}\text{Si}$, dissolved Si depleted surface runoff. Other studies such as Ziegler, Chadwick, White, et al. (2005) and Steinhoefel et al. (2017) have proposed alternative explanations based on the seasonally driven interplay between shallow/soil water and deep, steady-state groundwater (baseflow) contributions to observed stream chemistry. In this framework, activation of soil water stores and associated reaction pathways occur as a result of increasing water to rock ratios during high-discharge periods, ultimately driving stream $\delta^{30}\text{Si}$ behavior. The systematically observed decrease in stream $\delta^{30}\text{Si}$ with increasing discharge is interpreted in this context to reflect clay or phytolith dissolution (a source of “light” ^{28}Si) promoted by high dissolved organic carbon (DOC) exports derived from extensive biological cycling during dry summer periods.

Each of the mechanisms described above were developed to explain individual catchments. Extension of such site-specific conceptual models to serve as a global framework for short-term Si catchment dynamics remains an open question, limited by a lack of any cross-site analyses for $\delta^{30}\text{Si}$ of small catchments on the scale of what has been done for solute concentrations (Godsey et al., 2009, 2019; Oliva et al., 2003; White & Blum, 1995). Cross-site comparison of Si concentrations and mass fluxes suggest the dominance of site-specific catchment processes such as hydrologic function and permeability structure (Ameli et al., 2017; Wlostowski et al., 2021), soil characteristics (Bluth & Kump, 1994; Oliva et al., 2003), and weathering intensity (Riebe et al., 2001), which together serve as a fundamental driver of cross-site variability (Godsey et al., 2019; Hunsaker & Johnson, 2017). However, cross-site comparisons using high-frequency storm event data are rare (Wlostowski et al., 2021) and virtually non-existent in the silicate weathering and silicon stable isotope literature. Thus, we are left with a critical knowledge gap regarding how stream Si fluxes and $\delta^{30}\text{Si}$ compositions vary between periods of quiescence and these high-discharge events, as well as across catchments. Ultimately, this gap in knowledge obscures our capacity to identify site-specific effects versus universal controls on silicate weathering fluxes.

In the present study, we present a novel high frequency dataset of aqueous Si concentrations and stable isotopes ($\delta^{30}\text{Si}$) for multiple storm events in multiple low-order streams, providing a first of its kind cross-site comparison of Si solute and isotope dynamics. We complement this dataset with new analyses of the germanium to silicon ratios (Ge/Si) in the same samples, to better distinguish the relative effects of clay formation and biological uptake on Si isotope fractionation. Seven storm events across six low-order catchments spanning sub-humid to wet tropical climates, sedimentary to granitoid lithologies, and various biomes were investigated as part of a cross-CZO collaboration (SAVI, *Science Across Virtual Institutes*) between French (OZCAR, Gaillardet et al., 2018), Canadian (Hakai Institute), and American (Brantley et al., 2017) Critical Zone networks. In the present study we leverage this unprecedented dataset to address three guiding questions:

1. How widely do storm event stream $\delta^{30}\text{Si}$ signatures vary across headwater catchments featuring distinct rock types, climate, and ecosystems?
2. Can storm events serve as proxies for long-term silicon isotope signatures?
3. What are the principal hydrological and (bio)geochemical controls on stream $\delta^{30}\text{Si}$ compositions?

In this pursuit, we focus principally on the analysis of these novel datasets between sites. Detailed analysis of Si–Q and $\delta^{30}\text{Si}$ –Q across each storm hydrograph presents a significant and compelling opportunity which will appear in subsequent publications. As a consequence, here we do not focus on variability of Si and $\delta^{30}\text{Si}$ within

Table 1
Catchment Characteristics

Site	Location	CZO network	Basin area (km ²)	Elevation (m)	Climate	Lithology	Biome	MAT ^a (°C)	MAP ^a (mm)	MAR ^a (mm)
La Jara ^b	New Mexico, USA	Jemez	3.3	2664–2934	Sub-humid	Rhyolite	Mixed conifer forest	5.1	670	456
Providence Creek (P303) ^c	California, USA	Southern Sierra	1.32	1731–2025	Mediterranean	Granodiorite	Mixed conifer forest	8.0 (3 to 19)	1015	281
Elder Creek ^d	California, USA	Eel River	16.78	400–700	Mediterranean	Mixed argillite, sandstone	Coniferous forest	11.0 (−8 to 32)	1900	1744
Sapine ^e	Mont-Lozère, FR	OZCAR	0.54	1150–1350	Mediterranean	Granodiorite	Coniferous forest	7.0 (−5 to 17)	2000	1120
Hakai (Kwakshua watershed 708) ^f	British Columbia, CAN	Hakai Institute	7.8	0–385	Perhumid, coastal temperate rainforest	Quartz diorite	Coniferous forest and wetlands	8.5	3228	2084
Quiock Creek ^g	Basse-Terre GDLP, FR	OZCAR	0.08	200–350	Wet tropical	Andesite	Caribbean tropical forest	25.0	3500	1130

^aMean annual temperature (MAT), mean annual precipitation (MAP), mean annual runoff (MAR). ^bMcIntosh et al. (2017), Orem & Pelletier (2016), Troch et al. (2021), Vázquez-Ortega et al. (2015), Zapata-Rios et al. (2015). ^cBales et al. (2018), Dixon et al. (2009), Hunsaker & Johnson (2017), Safeeq & Hunsaker (2016). ^dKim et al. (2014, 2017), Rempe & Dietrich (2014), Salve et al. (2012). ^eCognard-Plancq et al. (2001), Durand et al. (1992), Küßner (2018), Martin et al. (2003). ^fGiesbrecht et al. (2021), Korver et al. (2020), Oliver et al. (2017), Roddick (1983, 1996). ^gClergue et al. (2015), Dessert et al. (2015), Dessert et al. (2020), Fries et al. (2019), Gaillardet et al. (2011), Guérin et al. (2019).

individual sites over the course of a given storm event. As will be seen, the present cross-site analysis offers a substantial contribution within which future site-specific analysis may be contextualized.

2. Site Description

We present datasets across two continents (North America and Europe) and three countries (United States, France, and Canada). Of the six sites investigated, two are located on islands (Guadeloupe—a Caribbean Island and Calvert Island off the coast of British Columbia). The catchments are all small (0.08–17 km²) with first-to third-order drainage networks spanning a range of climates (tropical to sub-humid), lithologies (volcanic, granitic, and shale), and ecological biomes (Caribbean tropical to coastal temperate rainforest to temperate mixed conifer forests). The data analyzed derive from a distinct period of high fluid infiltration and drainage within the respective catchment. In five of these catchments, we report rainfall-driven events and in one a seasonal snowmelt event (La Jara Creek). A summary of catchment characteristics is presented in Table 1 and Figure 1. A brief description of individual sites and the respective hydrological events that were sampled for this study (Table 2) are discussed in the following subsections.

2.1. La Jara Creek (35°50'N–36°00'N, 106°24'W–106°37'W)

La Jara Creek Catchment (basin area = 3.3 km²) is a part of the Jemez Critical Zone Observatory (National Research Council, 2001; T. White et al., 2015) located in the Valles Caldera National Preserve (VCNP) in the Jemez Mountains within northern New Mexico (USA). The creek is part of the larger East Fork of the Jemez River basin draining a 21 km wide caldera formed ~1.25 Ma with an elevation of 2664–2934 m (McIntosh et al., 2017; Zapata-Rios et al., 2015). The climate is sub-humid with a bimodal annual precipitation pattern totaling 710 mm, where snowfall accounts for ~44% of the total precipitation (McIntosh et al., 2017). The vegetation is characterized as a mixed conifer forest at higher elevations containing Spuce-fir (*Picea pungens*), ponderosa pine (*Pinus ponderosa*), aspen (*Populus tremuloides*), and gambel oak (*Quercus gambelii*) and forest meadows and grasslands in the valley (Coop & Givnish, 2007; Muldavin et al., 2006).

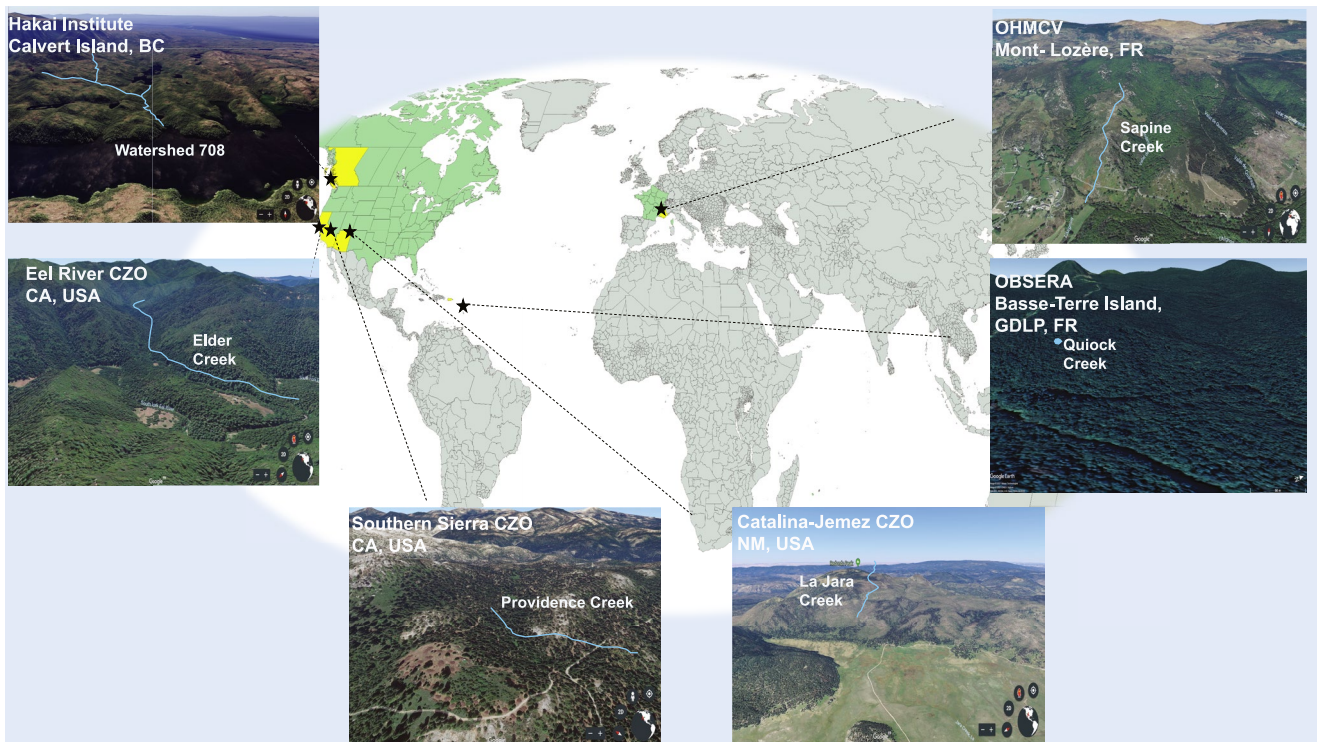


Figure 1. Description and location of sites where storm events were analyzed. Three sites are part of the American NSF-funded Critical Zone Observatories (Elder Creek, Eel River CZO; Providence Creek P301, Southern Sierra CZO; La Jara Creek, Catalina-Jemez CZO), two are part of the French Critical Zone infrastructure OZCAR (Quiock Creek, OBSERA; Sapine, OHMCV), and one is part of the Canadian Hakai Institute, Watershed 708.

Situated within a resurgent dome, the lithology of the La Jara Creek catchment (hereafter referred to as La Jara) is the most complex of all sites investigated in this study. In general, the lithology is largely dominated by Pleistocene aged Bandelier Tuff and fine-grained rhyodacite with primary mineral assemblages composed of Ca-clinophilite, alkali feldspar, cristobalite, albite, quartz and some minor accessory minerals such as apatite, hematite, zircon, titanite, ilmenite, and fayalite (Zapata-Rios et al., 2015). A deep regolith (42–27 m from ridge to base; Olyphant et al., 2016) and a relatively uniform (~1 m thick) soil layer overlies the mixed rhyolitic-sandstone bedrock (Moravec et al., 2020).

La Jara is a perennial stream where streamflow derives principally from shallow and deep groundwater flow paths rather than overland flow (Bales et al., 2006; Henderson & Shuman, 2010; McIntosh et al., 2017; Zapata-Rios et al., 2015). The hydrology is typical for snowmelt driven systems, with peak discharge occurring in late March–early April. Mean annual runoff for the 2017 year was 1.25 mm day^{-1} (Troc et al., 2021; Table 1). In this study, we analyzed a 2017 spring snowmelt event spanning 3 months from early March to Late May (Olshansky et al., 2018). Peak discharge during this event ($0.15 \text{ m}^3 \text{ s}^{-1}$) was roughly three times higher than the largest snowmelt event recorded over the previous 15 years (McIntosh et al., 2017).

2.2. Providence Creek, P301 (37°65'2"N, 119°20'55"W)

Located near Fresno, California (USA) in the Southern Sierra Nevada Mountains, Providence Creek is a second-order perennial stream draining the catchment designated P303 (basin area = 7.8 km^2) as part of the Kings River Experimental Watersheds (Hunsaker, 2013) within the Southern Sierra CZO network (National Research Council, 2001; White et al., 2015). This catchment resides at an elevation of 1731–2025 m, placing it within the rain–snow transition zone. The climate is Mediterranean with over 90% of the mean annual precipitation (1015 mm; O'Geen et al., 2018) taking place between October and April (Hunsaker & Johnson, 2017). Vegetation is predominantly mixed conifer forest (Bales et al., 2011; Hunsaker et al., 2012) dominated by white fir (*Abies concolor*) and ponderosa pine (*Pinus ponderosa*). Providence Creek (hereafter referred to as Providence)

Table 2
Storm Event Hydrology Characteristics

Site	Duration (MM/DD, YYYY)	Seasonal context (wet/ dry)	$V_{\text{event}}^{\text{a}}$ (m ³)	$V_{\text{annual}}^{\text{a}}$ (m ³)	$F_{\text{event}}^{\text{b}}$ (%)	Q_{max}	Q_{min}	Q_{avg}	$Q_{0.95}^{\text{c}}$ (m ³ s ⁻¹)	$Q_{0.50}^{\text{d}}$ (m ³ s ⁻¹)	$Q_{0.05}^{\text{e}}$ (m ³ s ⁻¹)	σ	$q_{\text{avg}}^{\text{f}}$	$q_{\text{max}}^{\text{g}}$	σ	$q^{*\text{h}}$ (mm day ⁻¹)
													Q_{max}	Q_{min}	Q_{avg}	$Q_{0.95}^{\text{c}}$ (m ³ s ⁻¹)
La Jara	3 months (03/13– 05/18, 2017)	Snowmelt event	547,425	88,800	61.6	0.125	0.026	0.077	0.03	2.23	21.44	0.02	2.03	3.26	0.56	2.62
Providence	19 h (01/08– 01/09, 2018)	Wet season	1451	167,783	0.86	0.35	0.0023	0.0071	1.8×10^{-4}	3.89×10^{-3}	0.052	0.01	1.34	2.22	0.53	2.9
Elder	7 days (01/05– 01/12, 2017)	Wet season	4,358,012	30,515,599	14.3	33.70	1.34	6.31	0.51	11.44	45.75	7.94	37.2	163	40.4	34.1
Sapine	5 days (10/12– 10/17, 2016)	Dry → wet	8516	326,934	2.60	0.054	4.26×10^{-4}	0.02	5.0×10^{-8}	1.0×10^{-5}	5.0×10^{-5}	0.01	3.23	8.35	2.15	2.7
Hakai (Watershed 708)	(E1) 2 days 09/16– 09/19, 2017)	Dry → wet	57,750	16,243,021	0.36	0.61	0.18	0.33	3.0×10^{-3}	0.28	1.74	0.13	3.68	6.76	1.45	1.2
	(E2) 7 days 10/14– 10/21, 2017)	Wet season	1,250,198	16,243,021	7.70	5.34	0.15	1.47	3.0×10^{-3}	0.28	1.74	1.08	16.2	59.2	11.9	10.4
Quiock	20 days (10/06– 10/20, 2015)	"Wet" tropical storm season	1447	27,594	5.20	0.030	1.50×10^{-4}	0.0028	3.04×10^{-6}	1.20×10^{-3}	0.01	0.005	2.08	26.6	5.85	8.6

^aEstimated through trapezoid integration method on event and long-term stream discharge hydrographs. ^bFraction of the total volume of water exported annually (V_{annual}) released during the storm event (V_{event}). ^cLow-flow conditions for given year where flood event took place; $Q_{0.95} =$ low flow discharge exceeded 95% of the time. ^dMedian flow conditions for given year where flood event took place; $Q_{0.50} =$ median flow discharge exceeded 50% of the time. ^eHigh-flow conditions for given year where flood event took place $Q_{0.05} =$ high flow discharge exceeded 5% of the time. ^fAverage runoff for the given storm event calculated by normalizing the average discharge to the respective basin area (see Table 1). ^gMaximum runoff of the storm event determined by normalizing maximum discharge to the basin area (see Table 1). ^hMaximum runoff of the respective storm event (q_{max}) normalized to the mean annual runoff (MAR). Normalization requires converting MAR to mm/day (see Table 1).

is underlain by granodiorite overlain by a relatively thick, partially weathered regolith (35 m for catchment P303; Holbrook et al., 2014) and thin soils (1.0–1.5 m).

Mean annual runoff is approximately 281 mm day⁻¹ (Hunsaker, 2019; Hunsaker et al., 2012; Table 1). Snow constitutes roughly 35%–60% of annual precipitation (Bales et al., 2018; Liu et al., 2013). Streamflow in Providence is largely supplied by deep (50%–75%) and shallow (~32%) subsurface flow with small contributions from overland flow (3%), mainly in the form of snowmelt (Bales et al., 2011). The storm event analyzed for this site took place in the winter of 2018 during the wet season. This event corresponded to a high precipitation period lasting 2 days (from Jan. 8–9, 2018).

2.3. Elder Creek (40°00'48"N, 122°33'00"W)

Elder Creek is a perennial, third-order stream that flows for 16 km within the Angelo Coast Range Reserve as part of the Eel River watershed and Critical Zone Observatory (ER-CZO, National Research Council, 2001; White et al., 2015) in Northern Mendocino County, California (US). Samples were taken from Elder Creek (hereafter referred to as Elder) next to the heavily monitored Rivendell site (Rempe & Dietrich, 2014; Salve et al., 2012), a thin, soil-mantled hillslope (average slope angle of 30°). Elder resides in a Mediterranean climate marked by warm, dry summers and cold, wet winters where average temperatures range from -8°C to 32°C. The mean annual precipitation is 1900 mm with rainfall concentrated in the months of October-April (Salve et al., 2012). The site is characterized by a densely vegetated coniferous forest (Hahm et al., 2017) of Douglas fir (*Pseudotsuga menziesii*) and Pacific madrone (*Arbutus menziesii*).

The lithology characterizing this site consists of tectonically folded mudstone dominated by turbidite sequences and interbedded lenses of sandstones and conglomerates as part of the Coastal Belt in the Franciscan Formation (McLaughlin et al., 2000). The bedrock primary mineral assemblages is a clay-rich shale where quartz, plagioclase, Fe-rich chlorite, illite, montmorillonite, smectite, and kaolinite are the main constituents (Gu et al., 2020; Kim et al., 2014). Between the shallow soil layer (0.5–0.75 m) and coherent bedrock lies a thick section of fractured, partially weathered regolith (ranging from 25 to 5 m deep from ridge to base of the hillslope; Salve et al., 2012). The deepest section of the weathered regolith is fully saturated with a water table that fluctuates by several meters in height throughout the year. Above the saturated zone the regolith is partially saturated, rich in reactive gases such as O₂ and CO₂ and hosts a deep root network (Tune et al., 2020).

Elder is supplied principally by subsurface drainage with no consistent observations of overland flow (Kim et al., 2014; Salve et al., 2012). Mean annual runoff for the year 2016–2017 was 4.78 mm day⁻¹ based on streamflow data from Dendra (formerly the Berkeley Sensor Database <https://dendra.science/orgs/erczo>; Table 1). The event reported in this study was an exceptional atmospheric storm that spanned a 10-day period in the middle of the wet season from Jan. 5–13, 2017, achieving runoff values 7.8 to ~34 greater than the mean annual runoff (Table 2).

2.4. Sapine Creek (44°37'N 3°82'W)

Located ~80 km from the Mediterranean Sea at an elevation between 1150 and 1350 m (Cognard-Plancq et al., 2001), Sapine Creek (hereafter referred to as Sapine) drains a small granitic catchment (basin area = 0.54 km²) of the southern flank of the Mont-Lozère and resides within the National Park of Cévennes in Southern France. This catchment has been continuously monitored since the 1980s by the *Observatoire Hydrométéorologique Méditerranéen Cévennes-Vivarais* (OHMCV), now part of the French Critical Zone research network, OZCAR (*Observatoires de la Zone Critique: Applications et Recherche*; Gaillardet et al., 2018).

The Mont-Lozère region experiences a Mediterranean climate with average temperatures between -5°C and 17°C and a mean annual rainfall of 2000 mm. Autumn and spring are characterized by periods of intense rain called “événements cévenols” that consist in flash flood events that can be particularly dangerous to nearby villages located downstream. Beech (*Fagus sylvatica*) forest make up the vegetation cover of the catchment (Küßner, 2018). The lithology is composed of porphyritic granodiorite and monzogranite (part of the Pont-de-Montvert-Borne complex) where large (up to 10 cm) orthoclase megacrysts and fine-grained andesine, potassium feldspar, biotite, and quartz make up its overall primary mineral assemblage (Küßner, 2018). A thin, highly

permeable soil layer (~0.6 m Cognard-Plancq et al., 2001; Marc et al., 2001), overlies a relatively deep, heterogeneous regolith layer (10 m thick).

Sapine is a perennial, first order stream hydrologically characterized by quick responses in discharge and stage height to rainfall (Martin et al., 2003). Mean annual runoff for the 2015–2016 years was 3.07 mm day⁻¹ (Küßner, 2018; Table 1). Notably, no development of overland flow from infiltration excess is observed during storm events at this site (Martin et al., 2003). The storm event analyzed in this study was the first of significance following the dry season, occurring over a one-week period from Oct. 11–18 in 2016. Long-term sampling was also analyzed for the purpose of this study, taken on a roughly bi-monthly basis over a 2 year period from 7 July 2013 to 31 March 2014 ($n = 8$).

2.5. Hakai (51°39'12.9672"N, 128°7'48.4032"W)

One of seven watersheds comprising the Hakai Institute's Kwakshua Watersheds Observatory recently integrated into the Critical Zone Exploration Network (CZEN, <https://www.czen.org/>), Kwakshua Watershed 708 is located in the northern section of Calvert Island off the central coast of British Columbia, Canada (Giesbrecht et al., 2021). Hereon referred to as "Hakai", this third-order, perennial stream drains a basin area of 7.8 km². Elevation ranges from sea level to 385 m (inland). Calvert Island is located in a perhumid coastal temperate rainforest. The ocean-moderated climate generally consists of cool and mild winters with mean annual precipitation ~3228 mm yr⁻¹ and mean annual temperature of ~8.5°C. Wet and dry seasons are less pronounced than those found in the other catchments investigated in this study, but generally span from September through April and May through August, respectively (Oliver et al., 2017). Short statured bog forests and wetlands make up the main vegetation cover (Thompson et al., 2016). Western red cedar (*Thuja plicata*), yellow cedars (*Chamaecyparis nootkatensis*), western hemlock (*Tsuga heterophylla*), and shore pine (*Pinus contorta*) are the dominant trees. Several shrubs, herbs, sedges, and bryophytes (e.g., *Sphagnum* spp.), are also present (Levy-Booth et al., 2019). A major feature of Kwakshua watersheds are that they represent a global "hotspot" for dissolved organic carbon yields to the ocean reaching 24.1 Mg C km⁻² in watershed 708 (Oliver et al., 2017). While yields of organic matter associated nutrients are high, inorganic nutrient yields are low enough (e.g., 59.6–72.6 kg Si(OH)₄ km⁻² yr⁻¹) to cause dilution in estuaries (St. Pierre et al., 2021).

Quartz diorite is the principal lithology on Calvert Island (Roddick, 1996), overlain by relatively thin (<1 m), organic-rich soils and a weakly developed regolith (Oliver et al., 2017). Mean annual runoff for Watershed 708 during the 2017 years was 5.71 mm day⁻¹ based on streamflow data available in the Hakai Metadata Catalog (Korver et al., 2020; Table 1). For this site, two storm events are reported which took place early in the wet season from September 16–19, 2017 and October 14–21, 2017, respectively.

2.6. Quiock Creek (16°17'N, 61°70'W)

Situated on Basse Terre Island as part of the Guadeloupe archipelago in the French West Indies, Quiock Creek is a small perennial, first-order tributary (basin area = 0.08 km²) of the Bras-David River. This site is part of the ObsERA CZO (OBSevatoire de l'Eau et de l'éRosion aux Antilles (Dessert et al., 2015; Lloret et al., 2011); and of the French National CZO network OZCAR (Gaillardet et al., 2018). Quiock Creek (hereafter referred to as Quiock) sits at an elevation of 200–350 m and is characterized by a wet tropical climate composed of a dry season from January to June and a wet, cyclonic season from July to December. Mean annual air temperature and rainfall are 5°C and 3500 mm, respectively. Vegetation consists of a dense, humid tropical forest categorized by a variety of tree and plant species such as Gommier (*Dacyrodes excelsa*), Ironwood (*Sloanea* spp.), *Cordia reticulata*, *Ammono caribaea*, *Tapura latifolia*, and sedges (*cyperaceae*) lined with sharp silica edges (Imbert et al., 1998).

The main lithology is Pleistocene andesitic pyroclastic deposits (Boudon et al., 1989; Clergue et al., 2015) overlain by a thick, strongly depleted soil (>15 m; Colmet-Daage & Bernard, 1979) profile with secondary minerals constituting roughly 95 wt.% of its bulk composition (Buss et al., 2010). The proximity of Quiock (~65 km) to the active Montserrat Volcano (located in the southern portion of Basse-Terre Island) and situated directly along the transatlantic path for Saharan dust plumes leads to significant input from volcanic ash and Saharan Dust, representing major sources of quartz and clays to the soil (Clergue et al., 2015; Dessert et al., 2020).

Hydrologically, Quiock is characterized by high evapotranspiration (60%–70%), a typical feature for tropical rainforests, and receives significant contributions from tropical storms and hurricanes, which can (as was the case for hurricane Rafael in October 2012) account for upwards of 5% of the total annual rainfall (Guérin et al., 2019; Zahibo et al., 2007). Mean annual runoff is 1130 mm (Fries et al., 2019; Guérin et al., 2019; Table 1). The event reported in this study took place during the wet season over a 3-week period from October 6–26, 2015 (Fries et al., 2019). The year 2015 was drier than the preceding years, with a mean annual throughfall input of ~2500 mm (Fries et al., 2019). The wet season for which the event took place was marked by major tropical storm, Erika, that touched down in late August and lead to extensive flooding and mudslides, causing major road damage on the Basse-Terre Island. This storm was followed by a category 1 hurricane Kate that struck Guadeloupe in early November, just after the sampling period in October.

3. Materials and Methods

3.1. Hydrometeorological Data

Annual and storm event rainfall intensity (mm h^{-1}) and stream discharge time series were collected from a range of meta-databases available via the institutions maintaining the respective CZO networks of each site. The French OZCAR network manages the Quiock (Guadeloupe) and Sapine (Mont-Lozère) sites, affording high-frequency hydro-meteorological data (5- and 30-min measurements, respectively) collected and distributed by the Observatoire de l'Eau et de l'éRosion aux Antilles (ObsERA: <https://webobsra.ipgp.fr>) and by the Observatoire Hydrométéorologique Méditerranéen Cévennes-Vivarais (OHMCV: <https://ohmcv.osug.fr>), respectively. The Hakai Institute provides 5-min stream discharge data through their Metadata Catalog (<https://hectate.hakai.org/geonetworks/srv/fre/catalog.search#/home>). For the U.S Critical Zone networks, high-frequency 15-min stream discharge and rainfall intensity data were obtained through the USGS National Water Information System (NWIS: <https://waterdata.usgs.gov/nwis>), CUAHSI Hydrologic Information System (HIS: <https://data.cuahsi.org>), and the respective CZO data repositories such as Dendra (formerly Berkeley Sensor Database) for the Eel River CZO (<https://dendra.science/orgs/erczo>) and the Climate and Hydrology Database Projects (CLIMDB/HYDROB: <https://climhy.lternet.edu>) sponsored through the NSF-LTER (Long Term Ecological Research) network, USGS, and US Forest Service. Further information regarding data collection and methodology for the respective sites can be found through the references and links provided above.

3.2. Elemental Analyses

Non-acidified, filtered ($0.22 \mu\text{m}$) stream water samples were analyzed by three laboratories for dissolved Si, major and minor cation (Na, K, Ca, Mg, Al, Sr) and anion (Cl^- , SO_4^{2-}) concentrations for all storm events. For La Jara, Hakai, and Providence creek chemical analyses were performed by the Arizona Laboratory for Emerging Contaminants (ALEC) using an Agilent 7700 quadrupole inductively coupled plasma spectrometer (Q-ICP-MS) at the University of Arizona, Tuscon, AZ (USA). Analytical QA/QC protocols were adapted from US EPA Method 200.8. Calibration standards were prepared from multi-element stock solutions (SPEX Certi-prep, Metuchen, NJ). Calibration curves include at least seven data points with correlation coefficients >0.995 . Quality control sample solutions are from an independent source, NIST SRM 1643e—Trace elements in water, or from High Purity Standards (Charleston, S.C.). Acceptable QC responses must be between 90% and 110% of the certified value (precision of $\pm 10\%$).

Sapine and Quiock, anion concentrations were determined through ion chromatography analyses at both ALEC and IPGP (Institut de Physique du Globe de Paris) using a Dionex ICS-6000 and Dionex DX120, respectively. Quiock major cation and dissolved silicon concentrations were measured by inductively coupled plasma-source mass spectrometry (ICP-MS; Thermo X-Series II) at the National Oceanographic Centre Southampton (NOCS). Synthetic multi-element standards prepared gravimetrically from high purity single element standard solutions were used for calibration. Certified reference material SLR-6 (river water) and IAPSO seawater were analyzed during the sample runs multiple times ($n = 8$) to determine the analytical precision ($\pm 5\%$ of certified values). Sapine major cation and dissolved silicon analyses were performed at IPGP by ICPMS (Agilent 7900 Q-ICP-MS) and UV-VIS spectrophotometry (Dionex UVD170U), respectively. For both analyses, instrumental precision ($\pm 5\%$) was determined and accuracy was checked using the certified river water reference standard SLRS-6.

3.3. Germanium Analyses

For Elder, Sapine, and Hakai storm events and the La Jara snowmelt, germanium (Ge) concentrations were analyzed at Cornell University using hydride-generation ICP mass spectrometry (HG-ICP-MS; Aguirre et al., 2017; Mortlock & Froelich, 1996) that included a custom HG sample introduction system, and a Thermo-Finnigan Element two ICP-MS. Natural water samples were prepared using a isotope dilution method where enriched ^{70}Ge spike solution is first added and then allowed to equilibrate for at least 48 hr at room temperature. Samples were spiked to a target $^{70}\text{Ge}/^{74}\text{Ge}$ ratio of 10, inferred from dissolved Si concentrations. For Ge concentration measurements, prepared samples were introduced into the hydride generation system along with a 4% NaBH_4 solution to reduce aqueous $\text{Ge}(\text{OH})_4$ to volatile GeH_4 . This volatile Ge phase is then passed through a gas-liquid-separation filter along with Ar as a carrier gas into the ICP-MS. Isotope dilution was used to quantify germanium using the $^{70}\text{Ge}/^{74}\text{Ge}$ ratio. Mass bias and signal drift were corrected via standard sample bracketing. Ge standards were measured at 5, 20, 50, 100, and 200 ng L $^{-1}$. Isotope dilution calculations were cross-checked using standard response curves generated at $m/z = 74$ for each Ge analysis. The contribution from the spike to m/z 74, with $^{70}\text{Ge}/^{74}\text{Ge}$ equal to 161.4, at $m/z = 74$ is insignificant ($\approx 0.1\%$). Analytical uncertainty on Ge concentration measurements at the Cornell University facilities is approximately 3% RSD (Aguirre et al., 2017; Derry et al., 2005; Kurtz et al., 2002, 2011; Lugolobi et al., 2010).

3.4. Silicon Stable Isotope Analyses

Stream samples were prepared for Si stable isotope analyses using a column chemistry protocol adapted from Van Den Boorn et al. (2006), Georg et al. (2006b), and Pringle et al. (2014). Si purification was conducted by loading 10–20 µg dissolved Si onto a pre-cleaned 1.8 mL BioRad AG50W-X12 cation-exchange resin bed in BioRad columns. Si was eluted by addition of 5 mL MQ-e water for a target concentration of 1–2 ppm (~ 9 –18 V). Approximately 70% of silicon is recuperated in the first elution step (2 mL MQ-e) with the remaining 30% recovered in the final elution step (3 mL MQ-e). The parent material for Elder Creek was also analyzed for the purpose of this study and was prepared using a modified alkali fusion technique developed by Georg et al. (2006a) described in detail by Fernandez et al. (2019).

The chemistry protocol outlined above involving a cation-exchange resin provides excellent Si yield, but fails to remove anionic species. Iso-baric anion matrix effects (i.e., SO_4^{2-} , DOC, NO_3^- , PO_4^{3-}) are known to introduce instrument mass bias in silicon isotope measurements of natural water samples (Dauphas et al., 2009; Hughes et al., 2011; Oelze et al., 2016). Rigorous evaluation of anion residual matrix effects conducted by Oelze et al. (2016) places the [anion]/[Si] molar ratio limit at 1, above which notable mass bias would be observed in Si isotope measurements. For the stream samples measured in this study all [anion]/[Si] ratios are < 1 with an average of 0.1 for $[\text{SO}_4^{2-}]/[\text{Si}]$. A notable exception are the Hakai samples where dissolved organic carbon content regularly exceeds 10 ppm. To remove this potentially significant mass bias, Hakai samples were subjected to alkali fusion following an adapted version of the protocol developed for the preparation of solid material for silicon isotope analyses (Georg et al., 2006a). The procedure involves an initial evaporation step of pre-weighed fluid consisting of a target 10–40 µg of Si that is dried down on a hot plate at 110°C in 15 mL Teflon vials until a target volume of ~ 1 mL is reached. Samples were then transferred with a pipette to cleaned Ag (silver) crucibles and dried down completely at 110°C. Half a tablet (i.e., 50 mg) of analytical grade NaOH was added to the Ag crucibles and subsequently fluxed at 720°C for 12 min in a muffled furnace. The fused product was then allowed to dissolve in PTFE vials containing 5 mL of ultrapure water for a target dissolved Si concentration of 2 ppm Si and then acidified with ultrapure HNO_3 to reach 2% HNO_3 concentration.

All silicon stable isotope analyses were performed on a Thermo Finnigan Neptune Plus MC-ICP-MS at the Institut de Physique du Globe de Paris. Sample introduction was in the form of a wet plasma using a SIS (Standard Introduction System), double Scott/cyclonic spray chamber and a 100 µL min $^{-1}$ Teflon® nebulizer. Measurements were run at medium resolution mode with a resolving power $M/\Delta M \sim 3300$ to reduce polyatomic interferences (notably the NO^+ interference on the ^{29}Si signal). To correct for magnet drift, a high-resolution peak centering was performed every hour to maintain a stable signal. Stable isotopic compositions are reported in standard per mil notation ($\delta^{29}\text{Si}$, $\delta^{30}\text{Si}$) based on blank-corrected ratios calculated through a standard bracketing method (Equation 1) using the silica sand internal standard (NBS-28, RM 8546):

$$\delta^{30}\text{Si} = \left[\frac{(^{30}\text{Si}/^{28}\text{Si})_{\text{sample}}}{\text{AVG}[(^{30}\text{Si}/^{28}\text{Si})_{\text{std-I}}, (^{30}\text{Si}/^{28}\text{Si})_{\text{std-II}}]} - 1 \right] \times 1000 \quad (1a)$$

$$\delta^{29}\text{Si} = \left[\frac{(^{29}\text{Si}/^{28}\text{Si})_{\text{sample}}}{\text{AVG}[(^{29}\text{Si}/^{28}\text{Si})_{\text{std-I}}, (^{29}\text{Si}/^{28}\text{Si})_{\text{std-II}}]} - 1 \right] \times 1000 \quad (1b)$$

where std-I and std-II correspond to the NBS-28 standard measured directly before and after the sample measurement. Repeated evaluation ($n = 400$) of the certified basalt standard BHVO-2 resulted in an appropriate value with long term precision of $-0.31 \pm 0.12\text{\textperthousand}$ (2SD). These results are consistent with previous measurements conducted at IPGP facilities ($-0.28 \pm 0.09\text{\textperthousand}$ (2SD), Pringle et al., 2014; Savage et al., 2013) and with reported values from the literature ($-0.30 \pm 0.14\text{\textperthousand}$ ($n = 133$), GeoReM Database: Jochum et al., 2016; Oelze et al., 2016). A three-isotope plot confirms mass-dependent fractionation for the samples analyzed in this study (Figure S1; $\delta^{29}\text{Si} = 0.54 \times \delta^{30}\text{Si}$, $R^2 = 0.98$), such that in the following only $\delta^{30}\text{Si}$ values are reported and discussed with a precision of 2SD derived from repeated measurements of individual samples ($n = 4$).

4. Results

4.1. Storm Event Characteristics and Relative Intensities

A majority of the storm events took place within and at the start of the wet season with the exception of La Jara, which was snowmelt driven. Mean runoff for all events was higher than the corresponding mean annual runoff (MAR; Table 1) for these streams. Three storm events (La Jara, Elder, and Quiock) displayed a maximum discharge higher than the 5% exceedance criterion defined from long-term discharge data (i.e., flow equaled or exceeded only 5% of the time (Table 2)). The storm event analyzed at Elder was the most extreme with regards to the historical record, corresponding to 14% of the total volume of water released during the year of sampling (Table 2). Mean and maximum discharge values for this event were ~ 7.8 and 34 times greater than mean annual flow, respectively. The first Hakai event was the most muted with the mean and maximum runoff barely exceeding the average annual runoff. The cumulative volume of water released during all sampled storm events represents on average 13% of the total annual export volume for the given catchments, with La Jara's snowmelt event being the largest (62%) and Hakai's first storm event (0.36%) being the smallest.

4.2. Dissolved Silicon, $\delta^{30}\text{Si}$, and Ge/Si Event Signatures

Dissolved Si concentrations and associated $\delta^{30}\text{Si}$ for all six catchments ($n = 155$) are summarized in Table 3 and illustrated in Figure 2 (see Supplementary for full dataset). Available long-term stream Si data for Sapine (this study), Elder (USGS NWIS, 2016; station 11475560), and La Jara (McIntosh et al., 2020) along with published data for Quiock (Gaspard et al., 2021) and Providence (Frings et al., 2021) are presented alongside the events for comparison. Stream Si concentrations (Figure 2a) during these high discharge events span roughly two orders of magnitude across sites from a minimum of $25 \mu\text{mol L}^{-1}$ measured at Hakai to a maximum of $1035 \mu\text{mol L}^{-1}$ measured at La Jara. Sapine and Hakai exhibited the tightest range in dissolved Si concentrations, reflecting a change of ~ 30 and $22 \mu\text{mol L}^{-1}$ throughout the course of the storm events, respectively. La Jara and Providence displayed the largest variability in dissolved Si concentrations with value ranges of ± 747 and $\pm 206 \mu\text{mol L}^{-1}$, respectively. Measured stream $\delta^{30}\text{Si}$ across all catchments (Figure 2b) shows a mean value of $+0.71 \pm 0.54\text{\textperthousand}$ where Quiock holds the lowest measured values ($-0.22 \pm 0.12\text{\textperthousand}$) and Providence the highest measured values ($+2.02 \pm 0.12\text{\textperthousand}$). All stream $\delta^{30}\text{Si}$ are elevated with respect to an average silicate bedrock value ($-0.28 \pm 0.15\text{\textperthousand}$, Savage et al., 2013). Within individual storm events, Quiock expressed the widest range in stream $\delta^{30}\text{Si}$ ($-0.22 \pm 0.21\text{\textperthousand}$ to $+0.45 \pm 0.14\text{\textperthousand}$) whereas Hakai Event 1 exhibited the smallest variations ($+0.38 \pm 0.09\text{\textperthousand}$ to $+0.60 \pm 0.13\text{\textperthousand}$). Figure 2 displays the sites ordered along a general climate gradient from sub-humid (La Jara) to wet, tropical (Quiock), illustrating a general trend toward more dilute stream dissolved Si and less overall variability. In contrast, stream $\delta^{30}\text{Si}$ lack any coherent trend along this climate gradient.

The La Jara, Providence, Elder, and Sapine storm events are found to mimic long-term variability in dissolved Si concentrations of these watersheds. Of these three sites La Jara exhibits the greatest variability ($288\text{--}1035 \mu\text{mol L}^{-1}$)

Table 3
Storm Event Silicon Chemistry Summary

N (samples)	La Jara		Providence		Elder		Sapine		Hakai		Quiock	All sites
	29	16	13	17	Event 1	Event 2	Both Events	60	20	155		
Dissolved Si (μmol/L)												
μ	476.5	458.4	327.9	55.6	33.0	34.2	33.9	83.6	200.0			
σ	228.7	61.1	31.2	7.7	6.5	4.9	5.4	8.7	219.7			
Min	288.2	343.9	259.8	45.3	24.7	26.2	24.7	61.4	24.7			
Max	1035.0	549.9	364.4	75.1	47.9	46.1	47.9	97.5	1035.0			
Median (50%)	376.1	477.8	336.1	55.2	31.0	30.4	32.8	84.6	73.0			
1st quartile (25%) ^a	324.8	402.4	327.5	49.2	29.0	30.4	30.2	79.4	35.1			
3rd quartile (75%) ^b	473.9	505.2	340.1	60.2	37.1	36.8	31.1	90.1	342.0			
At peak Q ^c	288.2	486.1	259.8	52.2	32.8	38.9	38.9	61.4	-			
At min Q ^d	328.3	465.0	362.9	75.1	25.7	32.2	32.2	89.9	-			
Q-weighted avg. ^e	464.3	448.6	303.3	53.0	33.4	34.2	34.1	68.0	-			
δ³⁰Si (‰)^f												
μ	0.76	1.92	1.14	0.32	0.52	0.45	0.47	0.21	0.71			
σ	0.10	0.12	0.13	0.17	0.06	0.10	0.10	0.17	0.53			
Min	0.55	1.70	0.87	0.02	0.38	0.19	0.19	-0.22	-0.22			
Max	0.94	2.03	1.34	0.55	0.60	0.68	0.68	0.45	2.27			
Median (50%)	0.76	1.95	1.13	0.37	0.54	0.45	0.47	0.25	0.54			
1st quartile (25%) ^a	0.68	1.87	1.07	0.17	0.50	0.39	0.42	0.13	0.39			
3rd quartile (75%) ^b	0.84	2.01	1.21	0.45	0.56	0.51	0.54	0.32	0.85			
At peak Q ^c	0.73	1.91	0.87	0.17	0.52	0.43	0.43	-0.21	-			
At min Q ^d	0.69	1.70	1.34	0.55	0.58	0.66	0.66	0.33	-			
Q-weighted avg. ^e	0.76	1.93	1.03	0.27	0.51	0.42	0.43	-0.09	-			
f_{diss}^{Si} (bedrock corrected dissolved Si)^h												
μ	0.49	0.29	0.11	0.15	0.79	0.92	0.88	NA	0.61			
σ	0.24	0.03	0.01	0.02	0.14	0.25	0.23	NA	0.37			
Min	0.23	0.21	0.09	0.11	0.44	0.21	0.21	NA	0.09			
Max	1.05	0.32	0.14	0.19	0.98	1.53	1.53	NA	1.53			
Median (50%)	0.40	0.30	0.11	0.15	0.80	0.93	0.91	NA	0.62			
1st quartile (25%) ^a	0.33	0.26	0.10	0.13	0.71	0.80	0.75	NA	0.28			
3rd quartile (75%) ^b	0.54	0.31	0.12	0.1	0.90	1.10	1.03	NA	1.00			
At peak Q ^c	0.37	0.31	0.12	0.11	0.84	0.86	0.86	NA	-			
At min Q ^d	0.23	0.30	0.11	0.15	0.62	0.89	0.62	NA	-			
Q-weighted avg.	0.48	0.28	0.12	0.15	0.91	0.99	0.90	I	-			
Δ³⁰_{diss-rock} (bedrock corrected δ³⁰Si) [%c]												
μ	0.92	2.14	1.53	0.55	0.75	0.68	0.70	0.39	0.94			
σ	0.10	0.11	0.13	0.17	0.06	0.10	0.10	0.20	0.55			
Min	0.71	1.93	1.26	0.25	0.60	0.42	0.42	0.02	0.02			
Max	1.10	2.26	1.73	0.78	0.83	0.91	0.91	0.68	2.50			
Median (50%)	0.92	2.17	1.52	0.60	0.73	0.68	0.70	0.45	0.77			

Table 3
Continued

	$\Delta_{\text{diss-rock}}^{30}$ (bedrock corrected $\delta^{30}\text{Si}$) [%]								
1st quartile (25%) ^a	0.84	2.10	1.46	0.40	0.77	0.62	0.65	0.32	0.62
3rd quartile (75%) ^b	1.00	2.24	1.60	0.68	0.79	0.74	0.77	0.51	1.01
At peak Q^c	0.89	2.14	1.26	0.40	0.75	0.66	0.66	0.02	-
At min Q^d	0.80	1.93	1.73	0.78	0.81	0.89	0.89	0.52	-
Q -weighted avg.	0.92	2.16	1.42	0.50	0.74	0.65	0.66	0.16	-

^aFirst quartile indicates 25% of the observations lie below this value. ^bThird quartile indicates that 75% of the observations lie below this value. ^cValue of DSi (μM) or $\delta^{30}\text{Si}$ (‰) at maximum discharge during either the storm event at the respective catchment or across all sites (noted here as “all sites”). ^dValue of DSi (μM) or $\delta^{30}\text{Si}$ (‰) at minimum discharge during either the storm event at the respective catchment or across all sites (noted here as All sites). ^eDissolved silicon concentration discharge-weighted average calculated as defined in Equation 2a. ^fNote all $\delta^{30}\text{Si}$ values report a precision of 2SD. ^gDissolved Si stable isotope discharge-weighted average calculated as defined in Equation 2b. ^hFraction of Si remaining in dissolved phase: mainland catchments calculated using Equation 4 with bedrock Si/Na ratios equal to 17.96 (Sapine; Küßner, 2018), 17.98 (Elder; Gu et al., 2020), 19.94 (Providence Creek; Hahm et al., 2014), and 12.38 (La Jara; Supplemental Materials, Section S.3). For Hakai we used Si/Ca ratios and normalization to bedrock following equivalent computation to Equation 4 based on bedrock Si/Ca value of 7.68 (Roddick, 1983, 1996). Quiock was assigned a value of 1.0 (see Section 4.3.2 for further details).

with respect to its long-term record ($146\text{--}565 \mu\text{mol L}^{-1}$, 2010–2013, McIntosh et al., 2017), which may be related to the unique characteristics of this spring snowmelt event. Elder, on the other hand, exhibits slightly less dissolved Si variability at the event-scale ($260\text{--}364 \mu\text{mol L}^{-1}$) relative to its long-term data ($184\text{--}300 \mu\text{mol L}^{-1}$, USGS NWIS, 2016; station 11475560). Event based $\delta^{30}\text{Si}$ data for Providence and Quiock are consistent with published data (Frings et al., 2021; Gaspard et al., 2021). For Sapine, stream $\delta^{30}\text{Si}$ variability from the event ($+0.02\text{‰}$ to $+0.55\text{‰}$) is greater than observed long-term values ($+0.17 \pm 0.05\text{‰}$ to $+0.30 \pm 0.06\text{‰}$, this study, Figure 2b). General agreement between event and historical stream dSi data indicates that storm events are informative proxies of long-term Si weathering signatures.

Four of the five Ge/Si datasets reported here were measured on the same fluid samples for the same storm events. These include Sapine, Elder, La Jara, and Hakai (Table S1). The La Jara snowmelt event displayed low fluid Ge/Si ratios ranging from 0.07 (minimum) to 0.15 (maximum) $\mu\text{mol mol}^{-1}$ and an average corresponding to $0.11 \mu\text{mol mol}^{-1}$ ($n = 23$). The Elder event fluid Ge/Si ratios remained relatively constant throughout the storm event with an average value of $0.28 \pm 0.03 \mu\text{mol mol}^{-1}$ ($n = 13$). Average fluid Ge/Si values for the Sapine and Hakai events correspond to $0.81 \pm 0.25 \mu\text{mol mol}^{-1}$ ($n = 30$) and $1.63 \pm 0.37 \mu\text{mol mol}^{-1}$ ($n = 63$, both events), respectively. A fifth dataset is also included for Providence based on 39 samples collected over approximately one year (Aguirre, 2019), yielding a flux-averaged fluid Ge/Si of $0.06 \pm 0.02 \mu\text{mol mol}^{-1}$. These samples are clearly distinct from the storm events reported thus far, but we show below that (a) these catchments appear to cluster closely among themselves (see Section 4.3.2) and (b) storm events display close agreement with longer-term datasets (Figure 2).

Discharge or q-weighted averages are calculated and presented in the subsequent figures (Figure 3 onwards) alongside the respective datasets to facilitate comparison across sites and storm events (e.g., Pokrovsky et al., 2013; Prokushkin et al., 2011). These discharge-weighted averages adjust the raw mean values to reflect their relative contributions to the total mass discharged during the event (Equation 2; Table 3):

$$\overline{[\text{DSi}]} = \frac{\sum (q_t \cdot [\text{DSi}])_t}{\sum q_t} \quad (2a)$$

$$\overline{\delta^{30}\text{Si}} = \frac{\sum (q_t \cdot [\text{DSi}] \cdot \delta^{30}\text{Si})_t}{\sum q_t \cdot [\text{DSi}]} \quad (2b)$$

where q_t is the measured stream runoff as a function of time (t) throughout the event duration, $\overline{[\text{DSi}]}$ and $\overline{\delta^{30}\text{Si}}$ represents the discharge-weighted mean for dissolved Si concentrations and stream Si stable isotope ratios, respectively. It is important to note that $\delta^{30}\text{Si}$ includes an additional dependence on the measured dissolved Si ($[\text{DSi}]$) as well. This approach essentially accounts for the relative intensities in the solute fluxes of the respective events. The overall discharge-weighted mean of stream $\delta^{30}\text{Si}$ values across all catchments is $0.70 \pm 0.61\text{‰}$. Across storm events, La Jara exhibits the highest $\overline{[\text{DSi}]}$ ($464 \mu\text{mol L}^{-1}$) and Hakai shows the lowest ($33.8 \mu\text{mol L}^{-1}$). Compar-

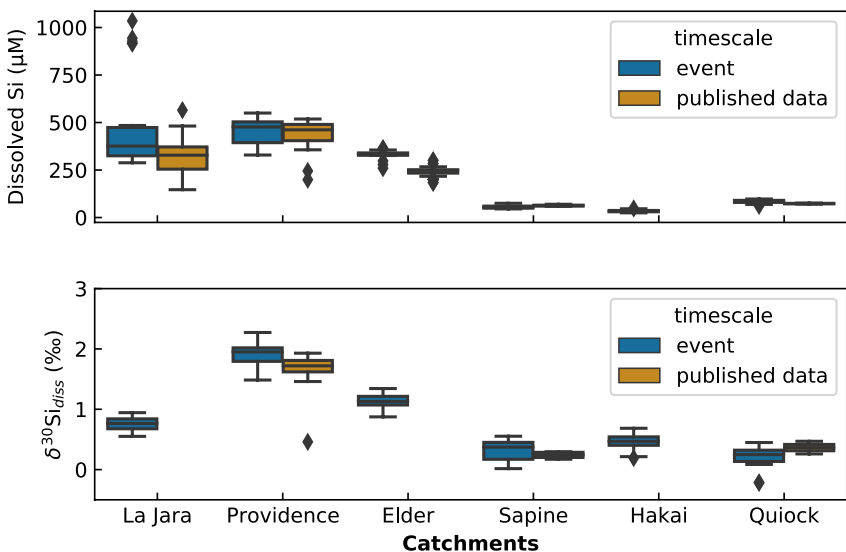


Figure 2. Box-and-whisker plots of stream dissolved Si concentrations (a) and $\delta^{30}\text{Si}$ (b) for each given site organized from left to right according to their respective climates from sub-humid (La Jara) to wet, tropical (Quiock). Box lengths represent the overall variability in dissolved Si and $\delta^{30}\text{Si}$ where the mean is depicted as a solid line within the box interior. Outliers are depicted as solid black diamonds. Published Si data (yellow) is compared against storm events (blue) for sites where such datasets are available La Jara (McIntosh et al., 2020), Providence (Frings et al., 2021), Elder (USGS NWIS, 2016; station 11475560), and Quiock (Gaspard et al., 2021). Sapine is an exception in this comparison and reflects long-term Si data measured for the purpose of this study.

ing individual measurements and discharge-weighted averages of stream $\delta^{30}\text{Si}$ against dissolved Si concentrations for all events (Figure 3) yields a weak positive correlation ($R^2 = 0.46$) bounded by a low dissolved Si ($<200 \mu\text{mol L}^{-1}$), low $\delta^{30}\text{Si}$ ($<+0.5\text{\textperthousand}$) end member describing Hakai, Quiock, and Sapine events and an elevated dissolved Si and $\delta^{30}\text{Si}$ end member consistent with Providence. With the exception of La Jara, which has several notable outliers, data points for individual events tend to cluster around their respective discharge-weighted averages with little overlap across sites. In the case of Hakai where two consecutive storm events were measured for the same

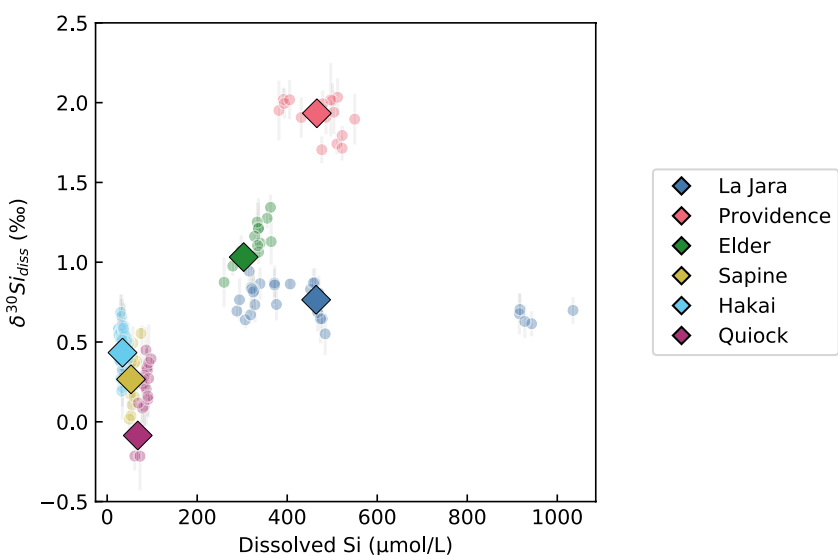


Figure 3. Stream $\delta^{30}\text{Si}$ plotted against dissolved Si concentrations for all sites. Individual measurements are shown as shaded circles whereas discharge-weighted averages (Equation 2) are represented by solid diamonds. Marine catchments (Quiock and Hakai) tend to plot at the lower $\delta^{30}\text{Si}$ and dissolved Si domain. Mainland catchments besides Sapine have higher $\delta^{30}\text{Si}$ and dissolved Si with Providence representing the upper bound. No definitive cross-site relationships are found between dissolved Si and associated $\delta^{30}\text{Si}$ values for the respective storm events. Error bars correspond to 2SD.

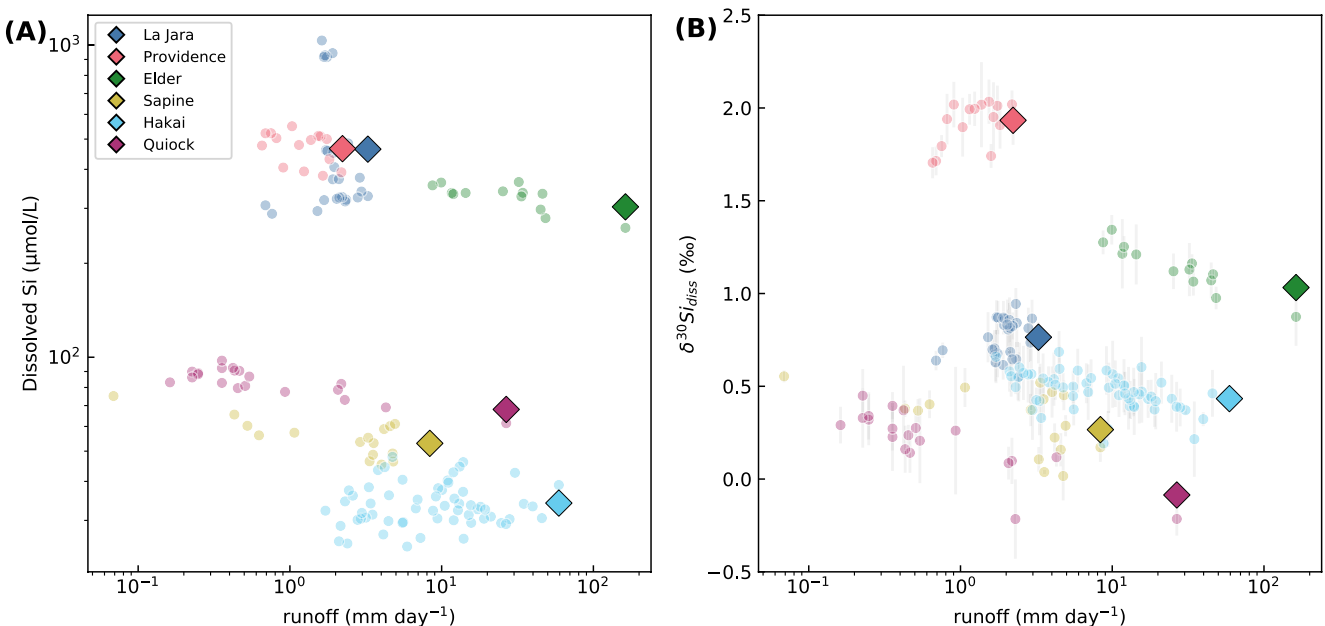


Figure 4. Dissolved Si and stream $\delta^{30}\text{Si}$ as a function of storm average runoff for each storm event. Shaded circles and diamonds correspond to individual sampling points and discharge-weighted averages (Equation 2), respectively. Across all sites, dissolved Si concentrations exhibit little sensitivity to runoff despite considerable variability in the latter, on the order of ~ 2 orders of magnitude (a). Silicon stable isotopes appear to capture intra-site variability, as shown for Elder with $\delta^{30}\text{Si}$ trending toward lower values with increasing runoff (b). For both dissolved Si and $\delta^{30}\text{Si}$, across-site trends as a function of runoff are negligible. Error bars correspond to 2SD.

year, stream $\overline{\text{DSi}}$ and $\overline{\delta^{30}\text{Si}}$ fall in the same range, together generating overall flux-weighted $\overline{[\text{DSi}]}$ and $\overline{\delta^{30}\text{Si}}$ signatures for Hakai of $34 \pm 5 \mu\text{mol L}^{-1}$ and $+0.42 \pm 0.10\text{\textperthousand}$, respectively.

Stream dissolved Si and $\delta^{30}\text{Si}$ show no systematic cross-site trend as a function of discharge (Figure 4). In Si-Q space, dissolved Si concentrations appear to remain relatively constant for a given site despite as much as two orders of magnitude variations in discharge (Figure 4a). There is no apparent relationship between Si and storm discharge. For example, Elder illustrates one of the highest discharges, yet produces one of the largest Si concentrations. In $\delta^{30}\text{Si}$ -Q space, we note a similar lack of correlation. Further, the lowest storm discharge is associated with the largest $\delta^{30}\text{Si}$.

4.3. Data Adjustment

Two corrections were applied to our storm event dataset prior to further analysis. These were made to address the influence of two external factors: (1) marine aerosols accompanying rainwater and (2) catchment lithology. Here we outline the respective data treatment methods implemented in this study and provide context relevant to the following discussion.

4.3.1. Atmospheric Corrections

Atmospherically-derived marine (sea salt) inputs can be a major source of dissolved cations to catchments situated close to oceans and seas (Chadwick et al., 1999; Derry & Chadwick, 2007; Stallard & Edmond, 1981). Four sites in our compilation are located in such areas. Hakai and Quiock are island catchments in the Pacific Ocean and Caribbean Sea, respectively, while Sapine and Elder reside ~ 80 km from the Mediterranean Sea in South-eastern France and ~ 15 – 20 km from the Pacific Ocean in Northern California, respectively. To remove potential rainwater aerosol contributions, a commonly employed method was implemented where stream Cl^- concentrations serve as a metric for atmospheric input (Equation 3; Gaillardet et al., 1999):

$$[X]^* = [X]_{\text{meas}} - \left(\frac{X}{\text{Cl}^-} \right)_{\text{rain}} \cdot [\text{Cl}^-]_{\text{meas}} \quad (3)$$

Here elemental seawater ratios ($(X/\text{Cl}^-)_{\text{rain}}$, Gaillardet et al., 1999; Riley and Tongudai, 1967; Stallard 1980) are used alongside stream Cl^- concentrations to infer the atmospheric contribution to measured stream water concentrations (where X corresponds to major cations Na^+ , Mg^{2+} , K^+ , Ca^{2+} and anion SO_4^{2-}). For island sites Hakai and Quiock, routine observations of Ca/Cl rainwater ratios exceeding that of seawater (Keresztesi et al., 2020; Derry & Chadwick, 2007; NADP (NRSP-3), 2020; Vet et al., 2014) are accommodated in further calculations (Section 4.3.2) by implementing a Ca/Cl ratio 1.5 times that of seawater. No such correction is required for Si and Ge, given the scarcity of these elements in wet deposition. Application of this method to stream dissolved cation concentrations would be compromised in the event that Cl -rich evaporites are present in the catchment, or in the case of hydrothermal inputs. However, prior geochemical and mineralogical characterization shows no such evidence for the sites included in this study (Buss et al., 2010; Frings et al., 2021; Gu et al., 2020; Küßner, 2018; Liu et al., 2008; Uhlig et al., 2017; Vázquez-Ortega et al., 2015; Zapata-Ríos et al., 2015). Correcting major cation stream chemistry for marine aerosol input accounts for most of the dissolved cation flux for the island catchments, Quiock and Hakai, with Na and Mg the most heavily impacted (~86%–100%; Table S1). In these settings, Ca appears to be the least impacted by atmospheric contributions accounting for 48% (Quiock) and 20% (Hakai) of the stream flux. Because of the extreme effect on Na in these settings, an alternative parent lithology correction was implemented for the island catchments (discussed further below, Section 4.3.2). Sapine is similarly impacted by aerosol input, although to a lesser extent. For Na and Mg, atmospheric contributions constituted on average 61% and 30% of the total dissolved stream budget, respectively. Despite being situated relatively close to the Northwestern California coastline, Elder is more comparable with the remaining sites further inland (La Jara, Providence), displaying only minor effects from atmospheric inputs (1%–26%).

Silicon is generally not included in these corrections due to its naturally low abundance in seawater ($58 \pm 49 \mu\text{M}$, De La Rocha et al., 2000) compared to the major ions (Na^+ , Ca^{2+} , Mg^{2+} , K^+ , Cl^- , SO_4^{2-}). Nevertheless, this does not exclude the possibility of atmospheric contributions to dissolved silicon budgets in catchments. Rather, other potentially prevalent atmospheric sources through dry deposition may be considered, such as North African (Engelstaedter et al., 2006) or Asian (Kurtz et al., 2001) dust inputs, which can be significant. For example, Quiock receives total dust fluxes of $100 \text{ kg ha}^{-1} \text{ yr}^{-1}$ owing to its position along the westward trajectory of the Saharan dust plume (Clergue et al., 2015). Geochemical tools such as radiogenic Sr isotopes ($^{87}\text{Sr}/^{86}\text{Sr}$) have been used frequently to constrain dust inputs (Dessert et al., 2020; Dia et al., 2006; Kennedy et al., 1998; Pett-Ridge, 2009; Stewart et al., 2001; Van der Hoven & Quade, 2002). However, applying dust corrections to stream chemistry presents a unique set of challenges due to limited information on dust dissolution kinetics and spatiotemporal variability in dust deposition and accumulation within the critical zone. From the handful of studies available on this subject, laboratory-based dissolution experiments suggest that dust contributions to the dissolved load can range between 1% and 10% depending on particle size, pH, and chemical affinity (Guerzoni et al., 1999). Without sufficient information to properly correct for dust inputs, we proceed under the assumption that this external pathway exerts a minor effect on our dissolved Si data.

4.3.2. Normalization of Stream Si Abundance and Parent Lithology Corrections

Dissolved Si concentrations alone do not represent relevant information in terms of Si release to and scavenging from solution as these raw concentrations are also influenced by dilution and/or evaporative effects. For this reason, the concentration of a solute of interest is often normalized to that of another element presenting conservative behavior, that is, one that is insensitive to processes that scavenge solutes from solutions. Here we use Na as a conservative element (Gaillardet et al., 1999) and examine stream dissolved Si/Na ratios to inform Si mass transfers.

Stream dissolved Si/Na ratios are also strongly influenced by source rock composition, which can obscure the effects of other relevant weathering parameters such as temperature, precipitation, and runoff (Edmond et al., 1995; Gaillardet et al., 1999; Huh et al., 1998). Application of a correction for the mostly mono-lithological small catchments presented in this work permits us to evaluate source rock controls across sites and to distinguish these differences from those caused by hydrology (runoff, fluid transit times) and reactivity (fractionating biogeochemical processes). Consequently, we further correct stream dissolved Si/Na molar ratios from bedrock effects by normalizing them to the Si/Na molar ratio of the corresponding bedrock, leading to the definition of $f_{\text{diss}}^{\text{Si}}$ (Equation 4, Brichau et al., 2008; Georg et al., 2006a; Gíslason et al., 1996; Stallard, 1980):

$$f_{\text{diss}}^{\text{Si}} = \frac{(\text{Si}/\text{Na})_{\text{stream}}}{(\text{Si}/\text{Na})_{\text{bedrock-qtz}}} \quad (4)$$

where Na^* refers to Na concentrations corrected for atmospheric contributions (Section 4.3.1). Following approaches from prior work (Hughes et al., 2013), a quartz correction was performed on bedrock Si concentrations to account for the non-stoichiometric dissolution of the primary mineral assemblage where Si is preferentially released from more reactive plagioclase and feldspars whereas quartz is relatively inert. A full description of the bedrock compositions used for each site and the quartz correction procedure is provided in Supplemental Materials (Table S2; Equation S.1). An $f_{\text{diss}}^{\text{Si}}$ value of one indicates congruent release of Si and Na from rock to streams. Conversely, an $f_{\text{diss}}^{\text{Si}} < 1$ indicates that dissolved Si has been scavenged by secondary processes, such as clay formation (Ziegler, Chadwick, White, et al., 2005) or biologic uptake (Opfergelt et al., 2010); $f_{\text{diss}}^{\text{Si}}$ values above 1 might indicate unaccounted-for Si supply by external sources, like dust, anthropogenic effects, or hydrothermal input. As explained in Section 4.3.1, correction for atmospheric sources of Na at the two island sites of Hakai and Quiock leads to Na^* values very close to 0, thereby resulting in large uncertainties on $f_{\text{diss}}^{\text{Si}}$ at these sites when using Equation 4. As a consequence, at these sites we estimate $f_{\text{diss}}^{\text{Si}}$ based on atmospheric input-corrected Ca rather than Na. Though Na is generally preferable, we note in Section 4.3.1 that Ca appeared to be less impacted by atmospheric inputs at these two sites.

The quartz-corrected $(\text{Si}/\text{Na})_{\text{bedrock-qtz}}$ ratio for each of the sites was determined based on the extent of available information for each respective bedrock chemical composition. A value of 17.98 was applied for Elder (Gu et al., 2020), 14.94 for Providence (Hahm et al., 2014), 1844 for Quiock (Buss et al., 2010), and 12.38 for La Jara (see Supplementary Material, Table S2; Broxton et al., 2007; Wilcock et al., 2013). A value of 17.96 was used for Sapine (Küßner, 2018). For Hakai, the quartz-corrected $(\text{Si}/\text{Ca})_{\text{bedrock-qtz}}$ ratio is 7.68 (Roddick, 1983, 1996). We note that in any given catchment, heterogeneity of bedrock mineralogical composition could produce a wide range of $f_{\text{diss}}^{\text{Si}}$ values, which we have encapsulated by using an average bedrock Si/Na in Equation 4. Fortunately, the drainage networks feeding these streams are already averaging over lithological heterogeneity across the catchment. Hence, the temporal variability in $f_{\text{diss}}^{\text{Si}}$ observed over the course of a storm event may (in part) reflect the diversity of lithological contributions, such that this variability can be used as an estimate of uncertainty in $f_{\text{diss}}^{\text{Si}}$.

This normalization of our storm events generated $f_{\text{diss}}^{\text{Si}}$ values that were all substantially less than 1 in the four non-island catchments, indicating that approximately 46% (La Jara) to 82% (Elder) of Si solubilized from bedrock is missing from the dissolved load. For Hakai, the alternative definition for $f_{\text{diss}}^{\text{Si}}$ produces an average value of 0.90 and appears to reflect a reasonable representation of this organic-rich, high-weathering intensity system in which the majority of solubilized Si is expected to be exported in solution. Based on the same modified version of Equation 4 using Ca instead of Na, Quiock returns values consistently > 1.0 , with an average of 1.9 using a seawater Ca/Cl ratio in Equation 4, and even higher values if we use $1.5 \times$ the seawater ratio. We attribute these unrealistically high $f_{\text{diss}}^{\text{Si}}$ values to bias inherent to the method of calculation (e.g., rock source composition, possible incorporation of Ca into the biomass), and take this estimation as confirmation that this system is exporting the entirety of dissolved Si released by silicate weathering. We resolve the issue by only reporting the flux-average values for Quiock in the remainder of our analyses using an $f_{\text{diss}}^{\text{Si}} = 1.0$ as a representative of congruent export of dissolved Si. Furthermore, we note that these $f_{\text{diss}}^{\text{Si}}$ values above 1, although possibly deriving from uncertainty inherent to our approach, can also to some extent reflect the actual release of Si from critical zone compartments (regolith and/or biota) during the sampled storm events. Regardless, the principal observation that can be drawn from our $f_{\text{diss}}^{\text{Si}}$ estimates at these two island sites is a near-congruent release of dissolved Si at the catchment scale.

Stream Si isotopes ratios are also partly controlled by source rock composition, and similarly require correction leading to the parameter $\Delta^{30}\text{Si}_{\text{diss-rock}} = \delta^{30}\text{Si}_{\text{diss}} - \delta^{30}\text{Si}_{\text{bedrock}}$. A value of $\Delta^{30}\text{Si}_{\text{diss-rock}} = 0$ suggests isotopically congruent primary mineral weathering as a primary control on stream $\delta^{30}\text{Si}$ while $\Delta^{30}\text{Si}_{\text{diss-rock}} > 0$ implies enrichment most likely driven by fractionating pathways such as secondary weathering or biological cycling. Granitoids and Upper Continental Crust (UCC) $\delta^{30}\text{Si}$ values systematically lie within a tight range (Savage et al., 2013), implying that primary mineral compositions are relatively uniform. Thus, bulk bedrock values are good approximations for the $\delta^{30}\text{Si}$ of congruently dissolving minerals. Local granitoid bedrock $\delta^{30}\text{Si}$ values were approximated by the average granitic ($-0.23 \pm 0.15\text{\textperthousand}$, Savage et al., 2012) and rhyolitic ($-0.16 \pm 0.04\text{\textperthousand}$, Savage et al., 2011) compositions for Sapine, Hakai, Providence, and La Jara (Table 1). The mixed-shale lithology characterizing Elder was measured directly for this study ($-0.39 \pm 0.06\text{\textperthousand}$). The $\delta^{30}\text{Si}$ composition chosen for Quiock's andesite lithology ($-0.23 \pm 0.09\text{\textperthousand}$) derives from Opfergelt et al. (2012). Observed $\Delta^{30}\text{Si}_{\text{diss-rock}}$ for all reported storm events are greater than 0 (Table 3) and display wide variability. Across catchments these values range from

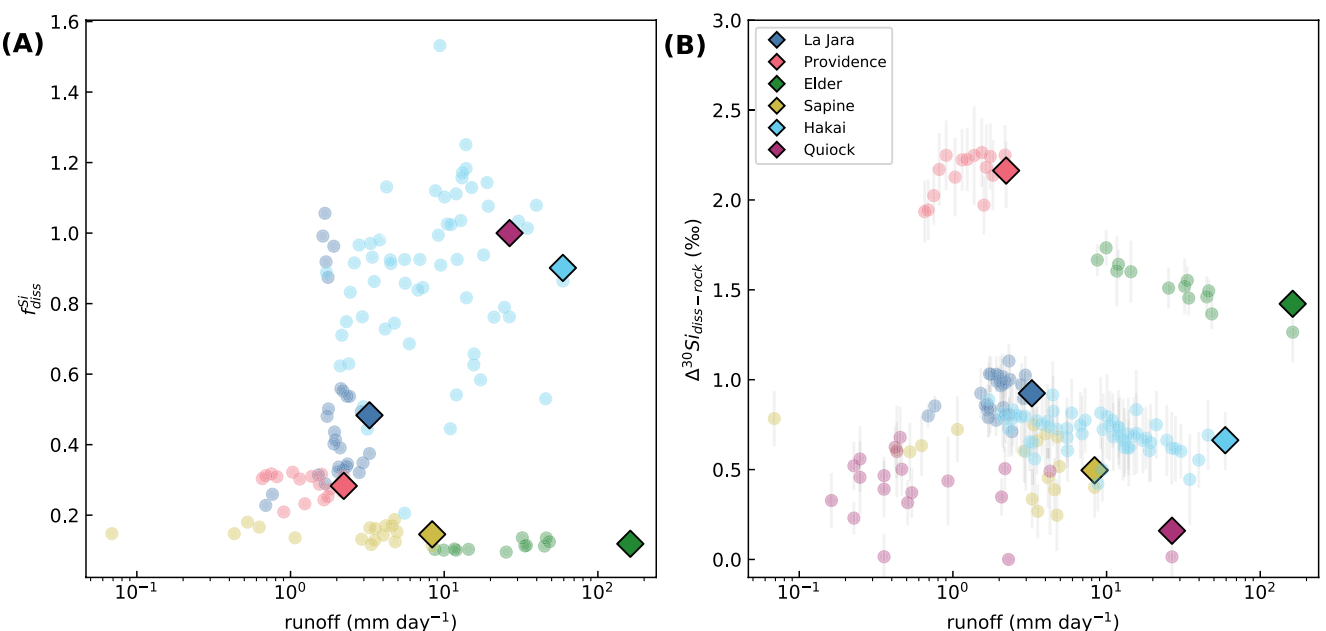


Figure 5. Normalized dissolved Si concentration ($f_{\text{diss}}^{\text{Si}}$, Equation 4 using Ca instead of Na for Hakai) and stream $\delta^{30}\text{Si}$ ($\Delta^{30}\text{Si}_{\text{diss-rock}} = \delta^{30}\text{Si}_{\text{diss}} - \delta^{30}\text{Si}_{\text{bedrock}}$) as a function of runoff for each storm event. Shaded circles and diamonds correspond to individual sampling points and discharge-weighted averages (Equation 2), respectively. Note that $f_{\text{diss}}^{\text{Si}}$ is set to 1 for Quiock, given the consistent values >1.0 returned by our analysis (Section 4.3.2). Correcting for bedrock does not yield any underlying global relationship across sites. However, two distinct groups appear in $f_{\text{diss}}^{\text{Si}}$ versus runoff space (a), corresponding to storm events in mainland catchments (Providence, La Jara, Elder, and Sapine) and those of the island catchments (Quiock, Hakai). Accounting for the bedrock in $\Delta^{30}\text{Si}_{\text{diss-rock}}$ versus runoff space results in a negligible change in the overall pattern and scatter observed across sites (Figure 4b). Error bars correspond to 2SD.

$+0.01 \pm 0.23\%$ (Quiock) to $+2.26 \pm 0.19\%$ (Providence) and within individual events (e.g., $+0.01 \pm 0.23\%$ to $+0.68 \pm 0.17\%$ for the Quiock storm event). In order to better appraise Ge versus Si enrichment in stream compared to the initial composition provided by rock dissolution, we also normalize dissolved Ge/Si ratios to the source rock Ge/Si ratio ($(\text{Ge/Si})_{\text{diss}} / (\text{Ge/Si})_{\text{rock}}$). In the absence of further constraints on local bedrock Ge content, we use an invariant $(\text{Ge/Si})_{\text{rock}}$ ratio of $1.5 \mu\text{mol mol}^{-1}$, consistent with values reported in Baronas et al. (2020), Edmond et al. (1995), and Rudnick & Gao (2013). All $f_{\text{diss}}^{\text{Si}}$ and $\Delta^{30}\text{Si}_{\text{diss-rock}}$ values are summarized for each site in Table 3 (compiled results, including $(\text{Ge/Si})_{\text{diss}} / (\text{Ge/Si})_{\text{rock}}$ values, can be found in the Supplementary).

5. Discussion

We observe no universal relationship between dissolved Si or $\delta^{30}\text{Si}$ as a function of runoff across our seven storm events and six low-order catchments. We now seek to determine why this is the case and to identify the common variable(s) responsible for observed intersite variability in stream Si chemistry. Toward this objective, we present a rigorous evaluation of possible lithologic, climate, hydrologic, kinetic and biologic controls. We explore how the inherent critical zone architecture and functionality of a given site can generate unique chemical and isotopic signals, and highlight the utility of high frequency, storm event datasets compared to those more commonly reported over annual or monthly resolutions (Bluth & Kump, 1994; Dessert et al., 2003; Gaillardet et al., 1999; Godsey et al., 2019, 2009; Oliva et al., 2003; West et al., 2005; White & Blum, 1995).

5.1. Absence of a Direct Control by Storm Runoff on Si Chemistry

Accounting for catchment lithology (see Section 4.3.2, Table 3) creates a pronounced distinction between the trends observed in raw (Figure 4a) and bedrock-corrected (Figure 5a) stream Si concentrations as a function of runoff. Uncorrected dissolved Si concentrations are highly scattered as a function of runoff with Providence, La Jara, and Elder grouping at the upper bound of dissolved Si concentrations while the remaining sites (Sapine, Hakai, and Quiock) group toward the lower bound. This observed scatter changes when the bedrock correction is applied, revealing a rather stark grouping between mainland and island catchments. Within the mainland

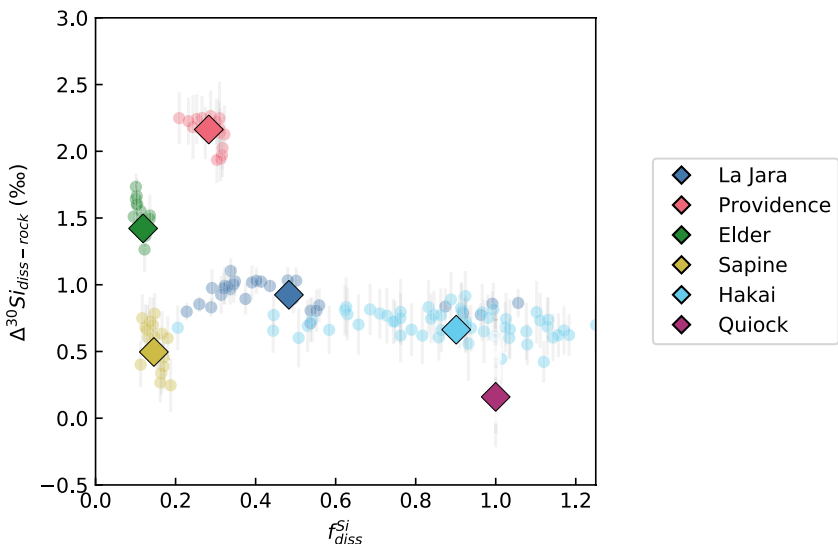


Figure 6. Bedrock-corrected stream $\delta^{30}\text{Si}$ ($\Delta^{30}\text{Si}_{\text{diss-rock}} = \delta^{30}\text{Si}_{\text{diss}} - \delta^{30}\text{Si}_{\text{bedrock}}$) versus dissolved Si ($f_{\text{diss}}^{\text{Si}}$, Equation 4, using Ca instead of Na for Hakai, and setting $f_{\text{diss}}^{\text{Si}}$ to 1.0 for Quiock; see Section 4.3.2) relationships across sites. Bedrock $\delta^{30}\text{Si}$ and (Si/Na) values are taken from the literature (see Section 4.4.2) apart from the Elder Creek mixed sedimentary bedrock $\delta^{30}\text{Si}$ ($-0.39 \pm 0.06\text{\textperthousand}$), which was measured directly for the purpose of this study. Accounting for the lithology does not considerably change the overall pattern observed in uncorrected $\delta^{30}\text{Si}$ versus dissolved Si space (Figure 3). Error bars correspond to 2SD.

catchments (Providence, La Jara, Sapine, and Elder), lower flux-weighted $f_{\text{diss}}^{\text{Si}}$ are generally associated with higher runoff rates, though individual data points display significant scattering about this apparent trend. In contrast, the island catchments (Hakai and Quiock) export nearly the entirety of dissolved Si expected to be released from bedrock ($f_{\text{diss}}^{\text{Si}} \sim 1$) and Hakai shows little sensitivity to runoff. Bedrock-corrected $\Delta^{30}\text{Si}_{\text{diss-rock}}$ values (Figure 5b) illustrate virtually no distinction from uncorrected values (Figure 4b) and remain relatively invariant as a function of discharge.

Storm events from different sites do not overlap in $f_{\text{diss}}^{\text{Si}}$ versus $\Delta^{30}\text{Si}_{\text{diss-rock}}$ space (Figure 6). Rather, the dataset is principally distinguished by individual catchments even after correction for atmospheric inputs and lithology. Hence, individual catchment properties clearly produce distinct solute and stable isotope signatures. Further, we find no unique relationship across catchments between $f_{\text{diss}}^{\text{Si}}$ and $\Delta^{30}\text{Si}_{\text{diss-rock}}$: a range of catchments display similar $f_{\text{diss}}^{\text{Si}}$ values of 0.2–0.3, with widely varying (by ~2%) $\Delta^{30}\text{Si}_{\text{diss-rock}}$ values (Providence, Sapine, and Elder), while catchments with similarly low $\Delta^{30}\text{Si}_{\text{diss-rock}}$ values (<1%) are characterized by very different $f_{\text{diss}}^{\text{Si}}$ (Sapine, La Jara, Hakai, and Quiock).

We note the existence of Si isotope fractionation at Hakai ($\Delta^{30}\text{Si}_{\text{diss-rock}}$ around 0.7%) despite apparent congruent release of Si from bedrock ($f_{\text{diss}}^{\text{Si}}$ close to 1; Figure 6). In principle, this apparent contradiction could be explained by a bias in the estimate of $\delta^{30}\text{Si}_{\text{rock}}$, for example, due to preferential dissolution of some minerals of heavy Si isotope composition. However, we are not aware of the existence of such heavy Si isotope enrichment in specific minerals of granitoid rocks (Savage et al., 2011, 2012). Incongruent release of heavy Si isotopes during mineral dissolution also offers an unlikely candidate to explain higher-than-bulk $\delta^{30}\text{Si}_{\text{rock}}$ values, as such a phenomenon is expected to occur mostly during incipient weathering and thus should not be expressed at a high-weathering intensity like Hakai.

In total our observations (Figure 6) are at odds with a unique fractionation mechanism and mass balance model for Si isotopes across our six catchments. We now turn to consideration of a variety of hydrologic and chemical factors that could underly these observations.

5.2. Hydrologic and Chemical Controls

Thus far we have demonstrated that these headwater storm events are representative of overall solute export dynamics in these streams (Figure 2). We now explore a series of simple scenarios to explain the cross-site

variability in this export record. First, we ask if this variability is controlled by binary mixing as suggested in previous studies of Si isotope fractionation at individual sites. Next, we consider the distinction among variable hydrologic transit time distributions, and finally the possibility of multiple fractionating processes.

5.2.1. End Member Mixing

Mixing controls are frequently invoked in the silicate literature to explain $\delta^{30}\text{Si}$ behavior as a function of discharge in a variety of locations (Engström et al., 2010; Georg et al., 2006a; Riote et al., 2018; Steinhoefel et al., 2017). In this framework, stream $\delta^{30}\text{Si}$ variability is driven by the interplay between a constant deep groundwater (baseflow) supply and varying contributions from soil waters. During dry periods, when discharge rates are low, stream $\delta^{30}\text{Si}$ is driven by baseflow. This end member experiences long contact times with fresh weatherable primary minerals, generating groundwater $\delta^{30}\text{Si}$ close to, but slightly elevated with respect to the bedrock composition due to the balance between primary mineral dissolution and the precipitation of secondary minerals more favorably formed at near-surface conditions. Soil solutions during these periods are typically elevated ($\delta^{30}\text{Si} >$ groundwater) due to low water/rock ratios favoring the formation of secondary clays and the additional effects of biological activity characterized by extensive plant cycling and uptake of dissolved Si. Following this framework, the first flush coming out of the dry season should drive stream $\delta^{30}\text{Si}$ to more elevated values with increasing discharge as a result of the mobilization of these enriched $\delta^{30}\text{Si}$ pools in the soil. This flushing should theoretically be associated with dilution in dissolved Si as a result of lower soil water Si concentrations. In contrast, the wet season is marked by more frequent high discharge events, increased water/rock ratios in the soil triggering clay and phytolith (or litter) dissolution and releasing light ^{28}Si back into soil waters (Steinhoefel et al., 2017). The result is lower soil water $\delta^{30}\text{Si}$, such that increased contributions from soil water to the stream should drive $\delta^{30}\text{Si}$ to lower values during periods of high discharge. Clay dissolution taking place within the stream has also been put forth as a potential low $\delta^{30}\text{Si}$ source in the binary mixing schematic, the extent of which depends on the suspended sediment load and clay content (Georg et al., 2006a).

Extrapolation of this end member framework to the global scale of our $\delta^{30}\text{Si}$ observations may not necessarily be expected to succeed. However, given the commonality of this approach in application to riverine $\delta^{30}\text{Si}$ analysis, we begin by considering whether mixing of two end members, common to all sites, could underlie our observed cross-site $\delta^{30}\text{Si}$ behavior. Binary mixing is tested by comparing $\Delta^{30}\text{Si}_{\text{diss-rock}}$ against $1/f_{\text{diss}}^{\text{Si}}$ (Figure 7a; Equation 4). Indeed, given that $1/f_{\text{diss}}^{\text{Si}}$ scales with $(\text{Na/Si})_{\text{diss}}$, binary mixing in the $\Delta^{30}\text{Si}_{\text{diss-rock}} - 1/f_{\text{diss}}^{\text{Si}}$ space should result in a straight line. No clear cross-catchment relationship is observed in this mixing space. Intra-site trends are difficult to parse, particularly among the four continental catchments. This observation is not necessarily in contradiction to the typical expectation from prior site-specific studies (described above). However, we find that there is no universal emergence of (1) a high $\delta^{30}\text{Si}$, low dissolved Si (or high $\Delta^{30}\text{Si}_{\text{diss-rock}}$, low $f_{\text{diss}}^{\text{Si}}$) shallow soil water pool and (2) a deep, low $\delta^{30}\text{Si}$, high dissolved Si (low $\Delta^{30}\text{Si}_{\text{diss-rock}}$, high $f_{\text{diss}}^{\text{Si}}$) groundwater pool that can explain our data across several sites. Altogether, mixing between internal $\delta^{30}\text{Si}$ stores is anticipated to play a role in observed site-specific variability, but lack of a systematic relationship across sites discredits the possibility of globally consistent $\delta^{30}\text{Si}$ soil and groundwater end members governing cross-site behavior.

5.2.2. Hydrologic Routing

We next consider the possibility that the fluid solute signatures measured in these six catchments all reflect varying degrees of a common fractionating reaction which removes Si from solution and enriches the remaining $\Delta^{30}\text{Si}_{\text{diss-rock}}$, as is typical of secondary mineral formation (Fernandez et al., 2019). We employ a simplifying assumption that this reaction proceeds via an isotopic distillation process, as has been previously applied to common isotopic signatures (e.g., $\delta^{30}\text{Si}$, $\delta^7\text{Li}$, $\delta^{26}\text{Mg}$) of weathering (Baronas et al., 2018; Dellinger et al., 2015; Georg et al., 2007; Tipper et al., 2012). The relationship between Si lost from solution due to vegetation cycling and/or secondary mineral accumulation ($f_{\text{diss}}^{\text{Si}}$) and the resulting observable fractionation of $\Delta^{30}\text{Si}_{\text{diss-rock}}$ from some nominal starting value of fluid near equilibrium with bedrock is then given by a simple Rayleigh equation:

$$\Delta^{30}\text{Si}_{\text{diss-rock}} = 1000 \cdot (\alpha_x - 1) \cdot \ln(f_{\text{diss}}^{\text{Si}}) \quad (5)$$

where $f_{\text{diss}}^{\text{Si}}$ corresponds to the same definition as above (Equations 4 and 5) and α_x corresponds to the fractionation factor associated with either secondary mineral precipitation (α_{sec}) or plant uptake (α_{upt}). This model creates one trajectory of coupled fluid $f_{\text{diss}}^{\text{Si}}$ and $\Delta^{30}\text{Si}_{\text{diss-rock}}$ evolution for all water exported from a given catchment (Figure 7b). In this application we use α_x values derived from experiments rather than from field data. Alternative

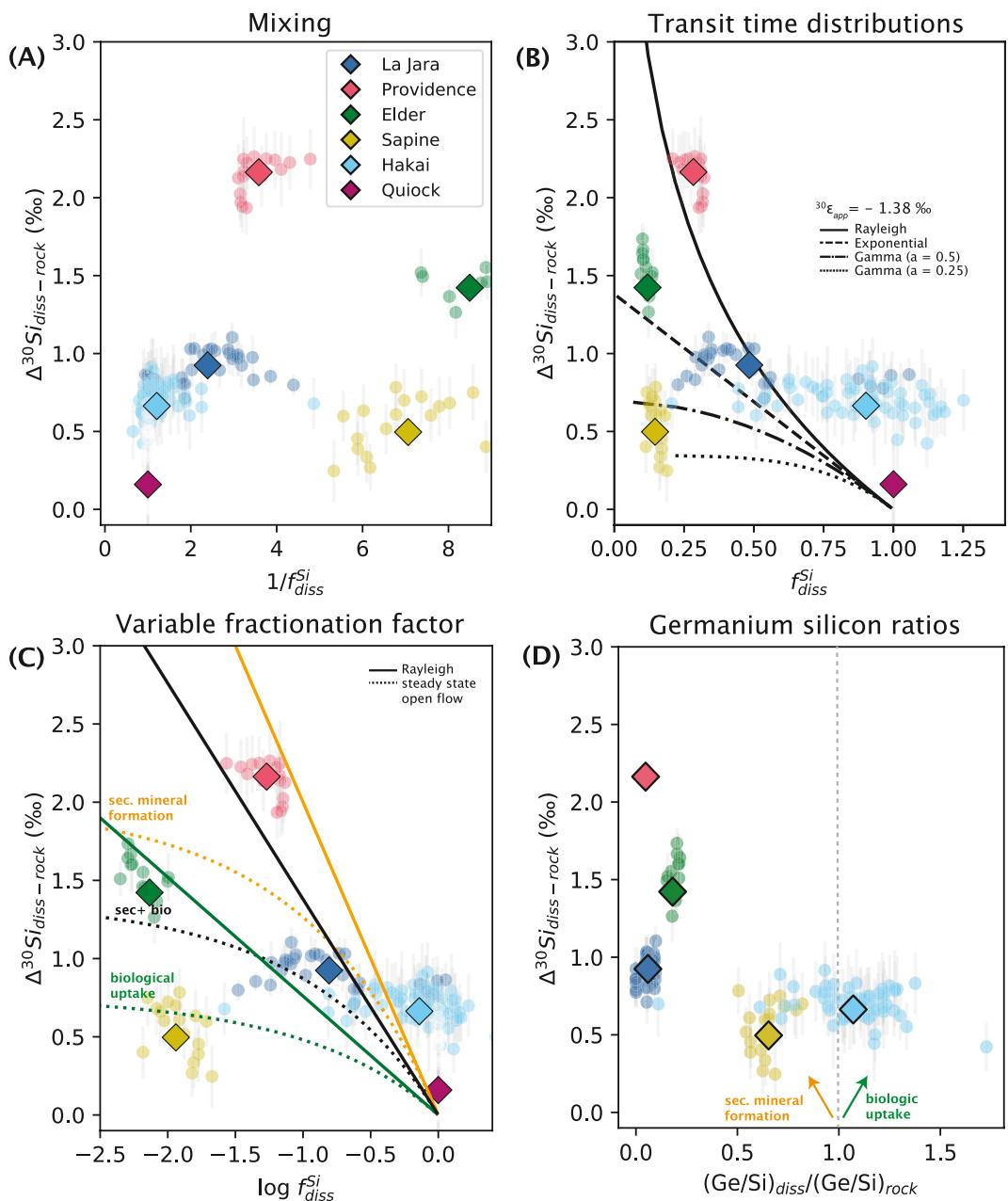


Figure 7.

frameworks, such as open-flow through models (Bouchez et al., 2013) utilize the difference in isotope signatures between clays (or organic material) and waters, as measured in the field, as an estimate of the fractionation factor. However, in the Rayleigh model, the difference between solution and the bulk of neo-formed solids (i.e., the cumulative product) is not an accurate estimate of the isotope fractionation factor. Rather, the fractionation factor in a distillation model manifests as the difference in isotopic ratio between dissolved Si (the reactant) and an instantaneously formed solid, which is often challenging to measure in the field due to differences in the timescales of formation of solid and solute isotope signatures. We return later to comparison between the Rayleigh approach and other widely applied models, as well as to the various ways isotope fractionation factors can be estimated for such models.

Simply applying this basic Rayleigh distillation model (Equation 5) to our data carries the assumption that all fluid spends an equivalent amount of time traveling through the watershed and arriving in the stream, for

example, a “plug” or “piston” flow system. Deviation from this basic model among our six catchments is then introduced through differences in the distribution of fluid travel times through a given watershed. These non-uniform travel time distributions (TTDs) offer a collective representation of the variety of pathways water may take in passing through the critical zone into the drainage network of a given landscape. In practice it is commonly observed that most of the fluid discharging into these fluvial drainage networks took relatively short (or fast) pathways through the watershed, while some smaller amount took much longer (Hornberger et al., 2001; Maluszewski & Zuber, 1996; McGuire & McDonnell, 2006). This leads to TTD functional forms that are typically weighted toward relatively young water but feature long tails which integrate a small portion of much longer transit times. Common examples include exponential and gamma functions (e.g., Gabrielli et al., 2018; McGuire & McDonnell, 2010).

Convolution of these non-uniform TTDs with the chemical reactions that supply geogenic solutes from water-rock interactions results in relatively “muted” or dilute concentrations relative to a piston-flow system (Maher, 2010, 2011). This is due to the relatively large proportion of young (i.e., less reacted) water sampled by these TTD functions. In relation to the present analysis, exponential and gamma TTDs would produce a relatively larger $f_{\text{diss}}^{\text{Si}}$ (i.e., less evolution from the bedrock-equilibrated concentration, Equation 4) than the corresponding piston-flow model for a given mean fluid travel time. Similarly, these TTDs may be applied to an isotopically fractionating reaction. Convolution of an exponential TTD with a fractionating first-order irreversible reaction produces a closed-form expression which is essentially a modification to the Rayleigh model (Druhan & Maher, 2017), given here in terms relevant to the present silicon isotope analysis:

$$\Delta^{30}\text{Si}_{\text{diss-rock}} = 1000 \cdot \left[\frac{1}{\alpha_x + f_{\text{diss}}^{\text{Si}} \cdot (1 - \alpha_x)} - 1 \right] \quad (6)$$

This particular function is based on a convolution integral combining a first-order irreversible reaction with an exponential TTD. Those familiar with common isotope fractionation models may note that Equation 6 is functionally similar to the evolution of a closed system, such that the reactant and product pools are always offset by $\epsilon = 1000 \cdot (\alpha_x - 1)$. We caution that this is simply a result of the use of a reaction rate law that is first order and irreversible. One should not expect that all fractionating reactions would convolve with an exponential TTD to produce this functional form. Similarly, convolution of the same first-order irreversible reaction with a different choice of TTD produces a different solution. In the case of the gamma TTDs, a closed form expression is not achievable, and the integral is calculated numerically (Druhan & Maher, 2017).

For the present application, we select a value of $\alpha_x = 0.9986$ ($\epsilon_x = -1.38\text{‰}$) that represents average contributions from both secondary weathering and biological cycling (discussed further Section 5.2.3). The results (Figure 7b) are a suite of $\Delta^{30}\text{Si}_{\text{diss-rock}}$ versus $f_{\text{diss}}^{\text{Si}}$ trajectories that distinguish among the six catchments. Within this framework, Providence closely adheres to a piston-flow model (Equation 5), which would suggest a relatively uniform fluid travel time through this system. The Elder storm was the most extreme event captured in our

Figure 7. Evaluation of end member mixing, hydrologic routing, and fractionation pathway controls across storm events. Shaded circles and diamonds correspond to individual sampling points and discharge-weighted averages (Equation 2), respectively. For Quiock, given the congruent export of dissolved Si from the system suggested by our analysis, we set $f_{\text{diss}}^{\text{Si}}$ to 1.0. The presence of a global end member mixing (Section 5.3) is refuted as a possible explanation for cross-site differences (a). Application of various travel time distributions (b) ranging from “plug” or “piston” flow (analogous to Rayleigh distillation along a given flow path, Equation 5) to exponential (Equation 6) to gamma (Section 5.2.2) accurately capture observed stream $\Delta^{30}\text{Si}_{\text{diss-rock}}$ for the mainland catchments, whereas release of dissolved Si at the two island catchments are too congruent to be accurately evaluated through such an approach. Reactivity (c) was evaluated through the application of “steady-state open-flow through” (solid lines, Equation 7) and “Rayleigh” (dashed lines, Equation 5) isotope mass balance models. Here we show three possible scenarios: (1) 100% net secondary mineral formation (orange dashed and solid lines) with a fractionation factor (ϵ_{30}) equal to laboratory derived values of -2.00‰ (Fernandez et al., 2019; Geilert et al., 2014; Roerdink et al., 2015; Yanhe et al., 1995; Ziegler, Chadwick, Brzezinski, et al., 2005); (2) 100% net biological uptake (green dashed and solid lines) with ϵ_{30} reflecting the average of estimates determined by prior studies ($-0.76 \pm 0.42\text{‰}$, Ding et al., 2008; Frick et al., 2020; Opfergelt et al., 2010; Sun et al., 2008, 2016); and (3) a 50/50 scenario where net secondary clay formation and biological uptake have equal contributions (black dashed and solid lines), which is adjusted in the steady-state open-flow through model by setting $f_{\text{diss}}^{\text{Si}} = f_{\text{bio}}^{\text{Si}}$ (Equation 7) while in the Rayleigh-model this is represented by an effective fractionation factor that represents an average between the two ($\epsilon_{30} = -1.38 \pm 0.52$). Providence is the only storm event that is compatible with piston-flow behavior coupled with a Rayleigh model, through a scenario in which only secondary clays are forming. The rest of the storm events appear to display more steady-state open flow through behavior, but this is less established. Error bars correspond to 2SD. An independent metric, $(\text{Ge/Si})_{\text{diss}} / (\text{Ge/Si})_{\text{rock}}$ (Section 4.3.2), (d) is afforded by germanium (Ge) measurements from Sapine, Elder, La Jara and Hakai along with prior measurements for Providence (Aguirre, 2019). Both flux-averaged and individual measurements are shown for La Jara, Sapine, Elder, and Hakai. Only the flux-averaged value is given for Providence since the Ge/Si ratios do not directly correspond to the same storm event. A dashed vertical line indicates the direction of Ge/Si partitioning in the fluid phase when dissolved Si is scavenged from solution due to secondary mineral precipitation and biological uptake.

dataset (Section 2.3) and would be anticipated to source a substantial portion of discharge from very short fluid travel times. This is consistent with the exponential TTD (Equation 6), which strongly weights these short residence times and shows good agreement with the Elder $\Delta^{30}\text{Si}_{\text{diss-rock}}$ versus $f_{\text{diss}}^{\text{Si}}$ values for the same $\alpha_x = 0.9986$. Finally, two common choices of gamma distributions are provided (Maher, 2011) distinguished by their shape factor, a . As the value of the shape factor decreases, the tail of the TTD becomes more pronounced and thus the range over which fluid travel times are sampled becomes larger. In this application the La Jara system appears to agree closely with a gamma TTD subject to a shape factor of $a = 0.5$, notably including the anomalous high $f_{\text{diss}}^{\text{Si}}$ values that appeared at the end of the storm event. Sapine appears to fall closer to gamma TTD with a shape factor of $a = 0.25$, suggesting an overall broader distribution in fluid residence times. Since the two island catchments have high $f_{\text{diss}}^{\text{Si}}$ values that essentially indicate congruent release of Si, meaningful evaluation of TTD effects are impeded. However, we do note that these two catchments, particularly Quiock, produce $f_{\text{diss}}^{\text{Si}}$ and $\Delta^{30}\text{Si}_{\text{diss-rock}}$ values that essentially mark the starting point of unfractionated fluid in the Rayleigh model space.

Clearly many factors complicate the evaluation of these TTDs as distinguishing features governing $\Delta^{30}\text{Si}_{\text{diss-rock}}$ signatures among our six catchments. These storm events are by definition transient periods of heightened discharge, and thus the underlying rates of fluid transport are time-variable. Recent efforts have focused on Storage Selection (SAS) functions and related frameworks that allow for this unsteady behavior (Benettin, Soulsby, et al., 2017; Harman, 2015; Van Der Velde et al., 2012), but parameterization of these models requires calibration against extensive datasets of tracer concentrations. Furthermore, it is highly unlikely that the $\Delta^{30}\text{Si}_{\text{diss-rock}}$ signatures of these catchments result from a single fractionating pathway (discussed further, Section 5.2.3). Nevertheless, our results show good agreement between the watershed datasets and modeled isotope signatures based on a single underlying fractionation factor and a range of common TTDs often applied to describe watershed transit times. Upon this basis, we cannot rule out an explanation for the intra-site variability observed in our lithology-corrected datasets originating from distinctions in the hydrologic routing of fluid through these catchments. As more constraints on hydrological flowpaths become available for these locations thanks to future research at the Critical Zone Observatories, convolution with fractionating reactions to model isotopic datasets such as ours presents a compelling opportunity to test this hypothesis. Importantly, until now this analysis of our cross-site Si isotope dataset in terms of variability in hydrological routing has relied on an invariant isotope fractionation factor thought to reflect equivalent roles of clay formation and biological uptake at all sites. However, and as discussed in the next section, our data clearly indicate that the role of these different fractionation pathways differs from site to site.

5.2.3. Multiple Fractionating Pathways

We next turn to the role of multiple fractionating pathways in producing our observed stream Si fluxes and $\delta^{30}\text{Si}$ ratios across these six catchments and seven storm events. In doing so, we effectively hold the influence of fluid TTDs fixed (Section 5.2.2) and explore variability in the fractionation factor(s) and fractionating process(es) that may impact site-specific behavior. In addition to the Rayleigh model, we utilize a steady-state open flow through model (Bouchez et al., 2013) where stable isotope ratios are predicted based on input and output solute fluxes between three biogeochemical processes characterizing the weathering zone: biological cycling, bedrock dissolution, and secondary mineral formation. In this framework, $\delta^{30}\text{Si}$ of the dissolved load exiting a given catchment can be described based on the mass transfer of Si between congruent dissolution of primary minerals, the formation of secondary minerals, or uptake via vascular plants. The latter two processes (secondary minerals and biological uptake) are the principal fractionating mechanisms for $\delta^{30}\text{Si}$ where their respective fractionation factors dictate the magnitude of dissolved Si isotopic partitioning. The original Bouchez et al. (2013) formulation is expressed here for Si stable isotopes:

$$\Delta^{30}\text{Si}_{\text{diss-rock}} = f_{\text{sec}}^{\text{Si}} \cdot -\varepsilon_{\text{sec}} + f_{\text{bio}}^{\text{Si}} \cdot -\varepsilon_{\text{upt}} \quad (7a)$$

$$1 - f_{\text{diss}}^{\text{Si}} = f_{\text{sec}}^{\text{Si}} + f_{\text{bio}}^{\text{Si}} \quad (7b)$$

where $\Delta^{30}\text{Si}_{\text{diss-rock}}$ corresponds to bedrock-corrected stream $\delta^{30}\text{Si}$ values and ε_{sec} and ε_{upt} correspond to the associated fractionation factors (given in epsilon notation) for secondary mineral precipitation and plant uptake by the biosphere, respectively. The relative proportions of secondary mineral precipitation and biological uptake to the overall amount of Si removed from the dissolved load ($1 - f_{\text{diss}}^{\text{Si}}$) is represented by $f_{\text{sec}}^{\text{Si}}$ and $f_{\text{bio}}^{\text{Si}}$, respectively. Note $f_{\text{diss}}^{\text{Si}}$ still remains consistent with Equations 4 and 5 as the bedrock-normalized dissolved Si concentration,

serving as a proxy for the amount of Si remaining in the fluid from some nominal bedrock-equilibrated starting point. Importantly, within this framework $\Delta^{30}\text{Si}_{\text{diss-rock}}$ depends linearly on the removal terms $f_{\text{sec}}^{\text{Si}}$ and $f_{\text{bio}}^{\text{Si}}$, as it would in the so-called "closed-system" model. Nevertheless, we stress that this linear dependency is obtained from a very different set of assumptions regarding the transfer of elements within the modeled system, which are those of an open-flow through system rather than those of a closed system lacking any export of matter out of the Critical Zone, for example, by erosion. One merit of this modeling approach is that it explicitly considers the possibility for mineral dissolution (both primary and secondary) to occur all along flowpaths in the weathering systems, where the Rayleigh model assumes that mineral dissolution occurs only where the fluid acquires its "starting" composition. However, the open-flow through model neglects any spatial separation between these different processes, and considers that the entirety of the fluid contained in the weathering system is well mixed at all times. Therefore, for the sake of their simplicity, both model types feature assumptions that somewhat contradict field observations, such that their capability to explain data needs to be systematically examined, when possible, as done in the present study. Regardless of their different sets of underlying assumptions, the basic principle in both the Rayleigh (Equation 5) and open flow through (Equation 7) approaches is that each sample taken during a given storm reflects progression of a (set of) reaction(s) subject to mass balance. In all these approaches, storm flow is assumed to nominally evacuate water, the composition of which is acquired from a relatively consistent set of weathering reactions over a time scale that is much longer than that of the flood itself.

Three fractionation scenarios are considered (1) 100% secondary mineral formation, (2) 100% plant uptake, and (3) 50/50 contributions from both secondary weathering and biological cycling. The fractionation factors implemented for these scenarios correspond to the average of previously published laboratory-derived values yielding ϵ_{sec} of $-2.00\text{\textperthousand}$ (Fernandez et al., 2019; Geilert et al., 2014; Roerdink et al., 2015; Yanhe et al., 1995; Ziegler, Chadwick, Brzezinski, et al., 2005) and an ϵ_{bio} of $-0.76\text{\textperthousand}$ (Ding et al., 2008; Frick et al., 2020; Opfergelt et al., 2010; Sun et al., 2008; Sun et al., 2016). As for the application of the Rayleigh model above, here these parameter values are restricted to fractionation factors determined through controlled laboratory experiments. Such an approach is necessary in multi-component isotope-enabled numerical reactive transport models (Druhan et al., 2019 and citations therein) and has been recently leveraged to successfully describe $\delta^7\text{Li}$ weathering dynamics in unit hillslopes (Golla et al., 2021). The combined apparent fractionation factor ($\epsilon_{\text{app}} = -1.38\text{\textperthousand}$) is determined from taking the average of the entirety of the known values for both fractionating pathways and is consistent with the value used in the Rayleigh (Equation 5) and TTD (e.g., Equation 6) models presented in Section 5.2.2.

Application of the open-flow through and Rayleigh models to the storm event data is presented in $\Delta^{30}\text{Si}_{\text{diss-rock}}$ versus $\log(f_{\text{diss}}^{\text{Si}})$ space (Figure 7c), where Rayleigh distillation now appears as a straight line. All three fractionation factors are considered, and generally appear to distinguish between the cross-site $\Delta^{30}\text{Si}_{\text{diss-rock}}$ versus $f_{\text{diss}}^{\text{Si}}$ datasets. Providence again exhibits Rayleigh-distillation behavior that is closely bounded by the cumulative apparent fractionation factor ($\epsilon_{\text{app}} = -1.38\text{\textperthousand}$) and the secondary mineral formation fractionation factor ($\epsilon_{\text{sec}} = -2.00\text{\textperthousand}$). The remaining mainland catchments (La Jara, Elder, and Sapine) all display behavior which is more consistent with the Bouchez et al. (2013) compartmental model. Elder and La Jara fall within the envelope between ϵ_{app} and ϵ_{sec} , whereas Sapine lies closer to the plant uptake value ($\epsilon_{\text{upt}} = -0.76\text{\textperthousand}$). The two island catchment storm events (Hakai, Quiock) are again exporting dissolved Si consistent with the net input to these systems and reflect correspondingly minimal fractionation, thus obscuring interpretation based on these model frameworks. However, we note that the combination of high $f_{\text{diss}}^{\text{Si}}$ and low $\Delta^{30}\text{Si}_{\text{diss-rock}}$ values at these two sites is consistent with the inferences made by Bouchez et al. (2013) from the open-flow through model that the preservation (or erosion) of fractionated secondary materials such as clays or litter, leading to lower $f_{\text{diss}}^{\text{Si}}$ values, is a pre-requisite for the expression of isotope fractionation in streams.

In comparison with the prior TTD analysis (Section 5.2.2), this similarly reasonable agreement poses a basic question: is it more realistic to expect that six catchments hosting low-order streams could differ in their overall $\delta^{30}\text{Si}$ fractionation factors by $>1.0\text{\textperthousand}$ or differ in the functional form of their fluid TTDs? Plausible arguments can be made for both, or some combination of the two. We note that the La Jara system is sub-humid and the event corresponds to spring snowmelt, suggesting conditions that would not normally support biological uptake as the primary fractionating pathway. Conversely, biological uptake could be anticipated to affect Si isotope fractionation at the two Island catchments, Hakai and Quiock. The former is characterized by limited secondary mineral formation most likely impacted by high organic-rich (i.e., DOC) interstitial waters that can hamper clay formation

(Oliver et al., 2017), while the latter is located in a highly productive tropical forest developed on a strongly cation-depleted soil (Buss et al., 2010; Clergue et al., 2015; Dessert et al., 2020). However, the data from both of these systems appears to indicate only minor net effects of vegetative cycling, which are not extensive enough to impact $f_{\text{diss}}^{\text{Si}}$, maybe due to complete recycling of Si from litter (Schuessler et al., 2018). In the $\delta^{30}\text{Si}$ - $f_{\text{diss}}^{\text{Si}}$ space the Sapine data fall below even the lowest models presented for the assessment of multiple fractionating pathways, lending support to our earlier inference of hydrologic routing as a primary control, as indicated by the close agreement of the gamma TTDs to the La Jara and Sapine storm events (Section 5.2.2, Figure 7b). We further note the important role of hydrologic routing in the extremity of the Elder event, where very large discharge volumes and rapid fluid transit could potentially overprint the evacuation of geochemically evolved fluid to the stream.

Further support for inter-site differences in fractionating and hydrologic pathways as the dominant control on observed Si isotope values is provided by the ratio of germanium (Ge) to silicon, for which data are available in five of our catchments (four of which have been measured in this study, Section 4.2). Germanium acts as a pseudo-isotope for silicon and the Ge/Si ratio partitions between pools in a similar fashion to $\delta^{30}\text{Si}$ when Si is scavenged from solution due to secondary mineral formation. However, the elemental equivalent of the isotope fractionation factor called the partition coefficient (denoted $K_D = \frac{(\text{Ge}/\text{Si})_{\text{product}}}{(\text{Ge}/\text{Si})_{\text{reactant}}}$) is in this case inverted, leading to lower fluid Ge/Si ratios and enriched secondary mineral Ge/Si ratios as the reaction proceeds (Aguirre et al., 2017; Ameijeiras-Mariño et al., 2017; Baronas et al., 2020, 2018; Gaspard et al., 2021; Kurtz et al., 2002; Lugolobi et al., 2010; S. Opfergelt et al., 2010; Perez-Fodich & Derry, 2020; Qi et al., 2019; Scribner et al., 2006). In contrast, evidence based primarily on phytoliths suggests Si uptake by vegetation strongly discriminates against Ge, causing the remaining fluid Ge/Si ratio to increase (Blecker et al., 2007; Derry et al., 2005; Meek et al., 2016). However, we note a recent study reporting whole plant Ge/Si ratios which suggests the capacity for no discrimination, and in some cases even preferential Ge uptake (Frings et al., 2021). Partitioning of Ge relative to Si across fluids, clays and vegetation creates quite pronounced signatures, and critically, should adhere to the same underlying fractionating effects and be subjected to the same TTDs as the $\Delta^{30}\text{Si}_{\text{diss-rock}}$ data.

From this basis, a direct comparison between stream $(\text{Ge}/\text{Si})_{\text{diss}}/(\text{Ge}/\text{Si})_{\text{rock}}$ versus $\Delta^{30}\text{Si}_{\text{diss-rock}}$ offers an independent opportunity to assess the role of multiple fractionation pathways (Figure 7d). Hakai's $(\text{Ge}/\text{Si})_{\text{diss}}/(\text{Ge}/\text{Si})_{\text{rock}}$ ratio of ~ 1.0 is in agreement with the $\Delta^{30}\text{Si}_{\text{diss-rock}}$ and $f_{\text{diss}}^{\text{Si}}$ results and further supports our inference that this system is exporting the entirety of Si expected to be released from bedrock. We note that a recent limited dataset of $(\text{Ge}/\text{Si})_{\text{diss}}$ reported for Quiock would also translate to stream $(\text{Ge}/\text{Si})_{\text{diss}}/(\text{Ge}/\text{Si})_{\text{rock}}$ values of ~ 1.0 (Gaspard et al., 2021), consistent with a congruent weathering signature. The remaining four catchments (Providence, Elder, and Sapine and La Jara) all exhibit $(\text{Ge}/\text{Si})_{\text{diss}}/(\text{Ge}/\text{Si})_{\text{rock}}$ ratios that require secondary clay formation as a dominant process impacting Si exports at these sites (Figure 7d). For Providence and Elder, a dominant effect of clay formation is consistent with the $\Delta^{30}\text{Si}_{\text{diss-rock}}$ data and do not offer any further distinction between the effects of TTDs (Section 5.2.2) and variable fractionation models (Section 5.2.3). In Sapine and La Jara, stream $(\text{Ge}/\text{Si})_{\text{diss}}/(\text{Ge}/\text{Si})_{\text{rock}}$ ratios are far too low to be describable by a system in which Si is predominantly cycled by vegetation which exhibits Ge discrimination, lending support to the model laid out in Figure 7b for gamma TTDs (Section 5.2.2) rather than strong vegetation cycling (Section 5.2.3).

In total, the Ge/Si ratios of these samples offer an independent proxy for the pathways by which silica is mobilized and retained in low order catchments. These data indicate that our interpretations based on Si isotopes alone are generally robust. Both Hakai and Quiock reflect $\Delta^{30}\text{Si}_{\text{diss-rock}}$ and $(\text{Ge}/\text{Si})_{\text{diss}}/(\text{Ge}/\text{Si})_{\text{rock}}$ ratios typical of (near-)congruent silica exports. This is consistent with other work suggesting congruent weathering in an independent catchment at the Hakai site (Nelson et al., 2021). The remaining catchments appear to be dominated by secondary clay formation. However, the inclusion of Ge/Si as an independent check cannot definitively rule out either variation in fluid TTDs or variability in the fractionation factor as an underlying contributor to the $\Delta^{30}\text{Si}_{\text{diss-rock}}$ signatures of these low-order streams. Rather, it appears both models are required in order to fully explain our observations.

5.3. A Combined Model

Our data-model comparisons suggest that a combination of unique TTDs and fractionation factors influence the distribution of storm event silica solute signatures across these six catchments. We thus suggest that a combined

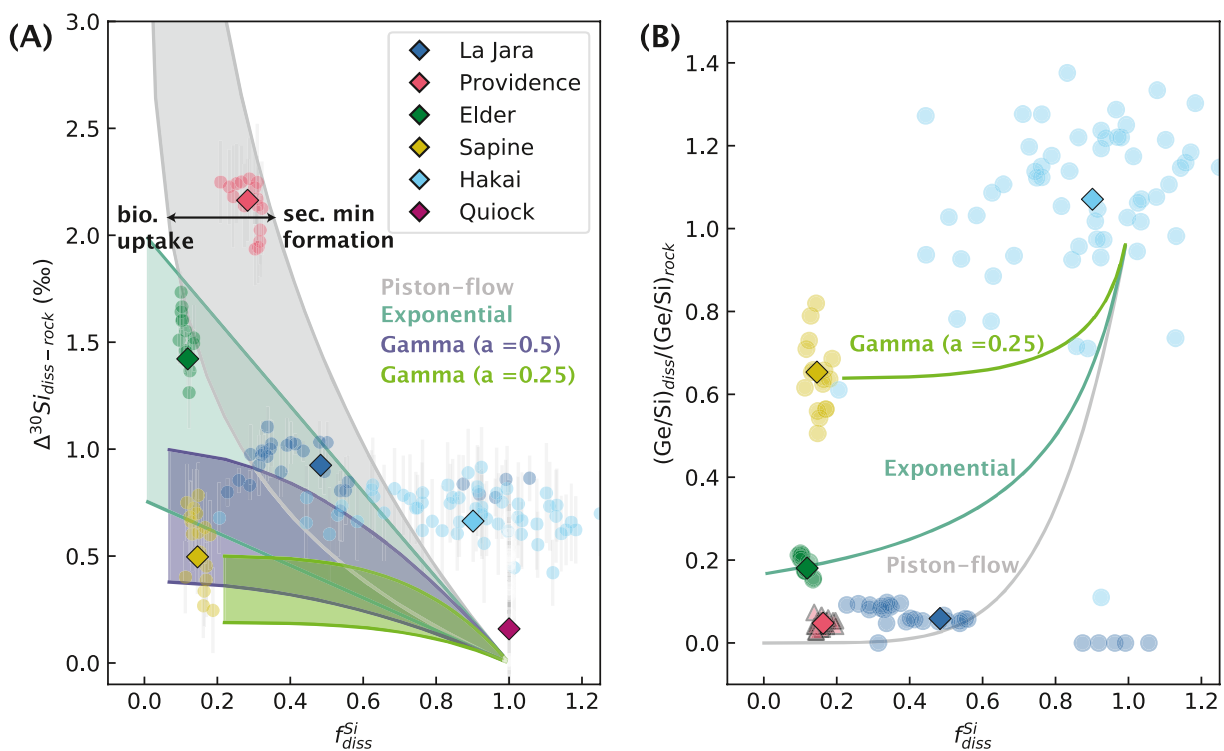


Figure 8. (a) Combined fractionation model with uniform (piston-flow) and non-uniform (exponential and gamma) transit time distributions where the bounds represent 2° clay formation (upper bound) and biological uptake (lower bound) reaction pathways with their respective fractionation factors, $\alpha_{\text{sec}} = 0.9980$ (${}^{30}\epsilon_{\text{sec}} = -2.00\text{\textperthousand}$) and $\alpha_{\text{bio}} = 0.99924$ (${}^{30}\epsilon_{\text{bio}} = -0.76\text{\textperthousand}$). Discharge-weighted averages for each site are shown as filled in diamonds and error bars correspond to 2SD. Application of this combined model yields distinct ranges of values that capture observed $\Delta^{30}\text{Si}_{\text{diss-rock}}$ variability across sites. (b) The same model framework is applied to Ge/Si ratios with partition coefficients for secondary clay formation ($K_D = 6.0$) and biologic uptake ($K_D = 0.005$) (see Section 5.3 for further details). Across both $\delta^{30}\text{Si}$ (a) and Ge/Si (b) plots, for Providence, Sapine and Elder, 100% of net fractionation is attributed to secondary clays. La Jara Ge/Si values are far lower than what would be anticipated given the $\Delta^{30}\text{Si}_{\text{diss-rock}}$ of this site. Hakai is essentially exporting ~90% of Si expected to be released from bedrock and correspondingly shows little partitioning in Ge/Si relative to bedrock.

modeling approach offers a more realistic and comprehensive means of encapsulating the effects of hydrology and biogeochemical reactions reflected in our global event-based dataset.

The two models (Sections 5.2.2 and 5.2.3) are combined by defining solution spaces for each of the four TTDs using upper (secondary mineral precipitation) and lower (vegetation) bounds for the corresponding fractionation factor (Figure 8a). Within the range of $f_{\text{diss}}^{\text{Si}}$ and $\Delta^{30}\text{Si}_{\text{diss-rock}}$ delineated by our datasets this combined model produces clear distinctions in the range of values that each TTD envelope can encapsulate. Both Elder and La Jara fall within a range defined by the exponential TTD (Equation 6), suggesting that the Elder system is strongly impacted by secondary mineral formation relative to vegetation. Sapine is quite muted in isotopic enrichment, resulting in close agreement with the gamma TTDs. For the two shape factors tested, Sapine also appears to correspond to strong secondary mineral precipitation effects given a shape factor of 0.25, though other combinations of gamma TTD could be expected to suggest more vegetation influence. The two island catchments reflect $f_{\text{diss}}^{\text{Si}}$ values so close to 1.0 that it remains difficult for any TTD to distinguish their behavior. As noted earlier, Providence remains strongly associated with a large fractionation factor and a piston-flow fluid transit time. There, the flux-weighted values of $f_{\text{diss}}^{\text{Si}}$ and $\Delta^{30}\text{Si}_{\text{diss-rock}}$ cannot be reasonably achieved with any of the other models.

The case of Providence is an interesting one in that two separate mass balance models appear to explain the same stream isotope dataset. Our analysis above shows that a fractionation factor based on experimental studies of secondary silicate formation (ϵ_{sec} of $-2.00\text{\textperthousand}$) together with a combined piston-flow TTD and Rayleigh-type fractionation matches observed storm stream Si isotope signatures at this site. Using a longer-term stream dataset yielding similar $\delta^{30}\text{Si}$ values, Frings et al. (2021) proposed that Providence stream Si isotope signatures could instead be explained by an open-flow through model with larger ϵ_{sec} of $-3\text{\textperthousand}$, consistent with the measured difference between clays and waters. Therefore, we are faced with a case where two models can explain the

observations, both in a way that is internally consistent, and each presenting their own caveats regarding the assumptions formulated based on the processes at play in the critical zone. This comparison underlines the need to further test these underlying assumptions when such simple models are the only option; as well as to develop and apply more realistic isotope models that encompass the variety of flowpaths and biogeochemical reactions in the critical zone, along with some description of their spatial distribution (e.g., Golla et al., 2021).

To our knowledge, this is the first attempt to combine a hydrologic model featuring non-uniform fluid transit representations with variability in the effective fractionation factor governing an isotopic signature. Given this novelty, it would seem reasonable to expect some additional testing of the model framework against an independent dataset. In pursuit of this requirement, we return to the Ge/Si ratios and ask whether the combined model can also describe this second metric for silica cycling in these catchments. Importantly, the partition coefficients for Ge/Si are not as tightly constrained as the fractionation factors for $\delta^{30}\text{Si}$ (Frings et al., 2021). However, in this test, our intent is to make use of the general capacity for Ge to enrich in secondary mineral phases, and thus produce a negative correlation between fluid phase Ge/Si and $\delta^{30}\text{Si}$ influenced by this reactive pathway. In contrast, the strong discrimination of Ge suggested to occur based on the phytolith composition of vegetation creates a very different correlation where both fluid phase Ge/Si and $\delta^{30}\text{Si}$ should enrich when subjected to biological uptake (Figure 7d). Such a marked difference in behavior should be observable regardless of the choice of TTD and inaccuracies in the Ge/Si partition coefficients are minimal relative to this fundamental difference between $\delta^{30}\text{Si}$ and Ge/Si. Once again, we make use of data measured for the same storm event samples in four of our catchments. For Providence, we again use the data reported by Aguirre (2019) and further use their corresponding $f_{\text{diss}}^{\text{Si}}$ values, applying the same atmospheric correction as the event-based dataset (Equation 3 with correction factor 0.183). To apply our combined model, we employ a partition coefficient of 6.0 for secondary mineral formation and discriminate Ge during uptake by vegetation using a value of 0.005 (Baronas et al., 2018, 2020; Frings et al., 2021; Perez-Fodich & Derry, 2020).

The resulting model, now adjusted to Ge/Si partition coefficients and with a $(\text{Ge/Si})_{\text{diss}}/(\text{Ge/Si})_{\text{rock}}$ ratio of 1.0 as a starting point, is applied to the five catchments using a parameter set based on the $\Delta^{30}\text{Si}_{\text{diss-rock}}$ versus $f_{\text{diss}}^{\text{Si}}$ model (Figure 8b). Hakai falls near the starting fluid composition in this model. Sapine, Providence and Elder present an interesting opportunity in that all three catchments appear to be strongly influenced by secondary clay formation in their $\Delta^{30}\text{Si}_{\text{diss-rock}}$ values (Figure 8a) but are differentiated by unique TTDs. Extending this inference to their $(\text{Ge/Si})_{\text{diss}}/(\text{Ge/Si})_{\text{rock}}$ ratios, we consider that secondary mineral precipitation constitutes 100% of the net effective fractionation factor (Figure 8b). The only difference between these three catchments is that Elder is modeled using an exponential TTD, Providence is considered a uniform flow field, and Sapine corresponds to a gamma TTD with shape factor of 0.25. Close agreement is noted for the $(\text{Ge/Si})_{\text{diss}}/(\text{Ge/Si})_{\text{rock}}$ versus $f_{\text{diss}}^{\text{Si}}$ values and the corresponding models across all three sites, creating a solution that is consistent across $\Delta^{30}\text{Si}_{\text{diss-rock}}$ and $(\text{Ge/Si})_{\text{diss}}/(\text{Ge/Si})_{\text{rock}}$ using the unified model. Finally, the La Jara dataset presents a distinct relationship between $\Delta^{30}\text{Si}_{\text{diss-rock}}$ and $(\text{Ge/Si})_{\text{diss}}/(\text{Ge/Si})_{\text{rock}}$ which was not immediately evident in the cross-plot (Figure 7d). Here, the combined model (Figure 8) highlights the fact that the $(\text{Ge/Si})_{\text{diss}}/(\text{Ge/Si})_{\text{rock}}$ values for La Jara (~ 0.09) are much lower than what would be expected given the corresponding $\Delta^{30}\text{Si}_{\text{diss-rock}}$ values of $\sim 1.0\text{‰}$, regardless of the chosen TTD. Elder already essentially defines the maximum effect of clay formation on the overall fractionation of $(\text{Ge/Si})_{\text{diss}}/(\text{Ge/Si})_{\text{rock}}$ for an exponential TTD and a partition coefficient of 6.0. Invoking a gamma distribution with the same strongly clay-dominated effects only further mutates the fractionation, resulting in a solution which would fall between the results shown for Elder and those shown for Sapine (Figure 8b). Thus, the apparent discrepancy between $(\text{Ge/Si})_{\text{diss}}/(\text{Ge/Si})_{\text{rock}}$ and $\Delta^{30}\text{Si}_{\text{diss-rock}}$ for La Jara appears to be a result of a difference in fractionating pathways affecting these two (pseudo)isotope systems in this catchment (or differences in the timescale of $\delta^{30}\text{Si}$ and Ge/Si partitioning; Fernandez et al., 2021), rather than a result of the choice of TTD. In our combined model, either the fractionation factor impacting $\Delta^{30}\text{Si}_{\text{diss-rock}}$ must be strongly muted at La Jara, or the partition coefficient impacting $(\text{Ge/Si})_{\text{diss}}/(\text{Ge/Si})_{\text{rock}}$ must be larger than the parameter values describing the rest of the streams analyzed in this study. As is apparent in Figure 8b, the 6.0 partition coefficient used to represent the affinity for secondary clays to preferentially incorporate Ge would require a TTD that is much closer to a uniform or piston flow model. In $\Delta^{30}\text{Si}_{\text{diss-rock}}$ versus $f_{\text{diss}}^{\text{Si}}$ solution space (Figure 8a), this would require a decrease in the Si isotope fractionation factor such that the value for secondary mineral formation would have to become even lower than the value used for uptake by vegetation. Further, as noted above, the fractionation factors for $\Delta^{30}\text{Si}_{\text{diss-rock}}$ are generally better constrained than the partition coefficients for $(\text{Ge/Si})_{\text{diss}}/(\text{Ge/Si})_{\text{rock}}$, making this explanation unlikely. Assuming instead that the inferences on TTD at La Jara made from the $\Delta^{30}\text{Si}_{\text{diss-rock}}$ versus

$f_{\text{diss}}^{\text{Si}}$ relationship are robust, the exponential TTD would also reproduce the La Jara $(\text{Ge/Si})_{\text{diss}} / (\text{Ge/Si})_{\text{rock}}$ ratios for a partition coefficient of 15.0, which is large, although plausible, relative to the range reported in prior studies (Aguirre et al., 2017; Ameijeiras-Mariño et al., 2017; Baronas et al., 2018, 2020; Kurtz et al., 2002; Lugolobi et al., 2010; Opfergelt et al., 2010; Perez-Fodich & Derry, 2020; Qi et al., 2019; Scribner et al., 2006). The La Jara regolith is highly enriched in well-crystallized smectite and zeolite, in which Si incorporation could lead to strong, uncharacterized Ge/Si fractionation (Moravec et al., 2020). Alternatively, we note that the La Jara dataset is the only example of a spring snowmelt-driven hydrograph in our study, which might have led to the export of a specific solute pool during the event at this site. This solute pool could be topsoil waters enriched in species derived from litter remineralization over the months of snowpack presence, which should lead to low Ge/Si ratios in the stream export. Overall, regardless of the cause, the La Jara system appears to have experienced stronger retention of Ge relative to the other catchments during this discharge event.

In total, the combined model is able to accurately distinguish between catchments that exhibit unique TTDs and are subject to unique fractionating pathways while maintaining consistency across $f_{\text{diss}}^{\text{Si}}$, $\Delta^{30}\text{Si}_{\text{diss-rock}}$ and $(\text{Ge/Si})_{\text{diss}} / (\text{Ge/Si})_{\text{rock}}$ values. We emphasize that the results of this unified TTD and variable fractionation model have been applied to the Ge/Si data without any effort to closely fit the models to the measured values. All parameters were consistent across the five sites, apart from the choice of TTDs (Sapine, Elder and Providence). We note the choice of TTD does not constitute a tuning parameter, but rather reflects three widely applied functional forms that are commonly employed to describe fluid transit times in small catchments (Kirchner et al., 2000, 2001; McGuire & McDonnell, 2006). A single exception is noted for La Jara, which appears to require a distinct $(\text{Ge/Si})_{\text{diss}} / (\text{Ge/Si})_{\text{rock}}$ partition coefficient, but at the cost of essentially creating a new tuning parameter. The apparent consistency across (pseudo)isotope metrics for silicon weathering despite the absence of tuning strongly supports the validity of the combined model framework and underscores the intertwined effects of fractionating pathways and hydrologic routing on observed stream silica signatures. Hence, the fundamental constant across our six sites are the combined effects of hydrology and biogeochemistry, which work in concert with one another to produce observed stream Si chemical and isotopic signals. Site-specific differences arise in how these hydrological and biogeochemical pathways are expressed, which is dictated by the distinct critical zone architecture and functionality of each site, including water drainage pathways, chemical weathering intensity and the balance between secondary mineral weathering and vegetation-driven nutrient cycling.

5.4. Resiliency of Silicate Solute Export Signatures During Storm Events

These six low-order streams exhibit remarkably distinct silicate weathering signatures even as they are subjected to storm events. Our model indicates that these distinctions derive from the unique architecture that is specific to each of these sites, rather than from systematic variation along a gradient in some overarching environmental variable. Here we take a holistic definition of critical zone “architecture” which encapsulates physical structure (drainage pathways, soil and regolith depth, lithology, spatial heterogeneity) as well as characteristic climate, vegetation, and biogeochemical reactivity (Anderson et al., 2007; Lin, 2010; Rasmussen et al., 2011; Riebe et al., 2017; Wlostowski et al., 2021) that combine to form the basis for ecosystem functioning and chemical weathering of a given catchment (Troch et al., 2015). The apparent significance of individual architecture in regulating silicate solute signatures complicates cross-site comparison. However, our study shows that within a given system, it appears that architectural controls are preserved even under extreme events. The Elder dataset, for example, reflects a period of time in which an “atmospheric river” established off the coast of northern California, leading to a storm that produced 14% of the total annual volumetric discharge of the stream in 7 days. The La Jara dataset is associated with spring snowmelt, which produced >60% of the total annual water exported through this system. Under such circumstances, biologically cycled solutes (e.g., N, P, DOC, K) and redox-sensitive elements (Fe, Mn, S) have been shown to exhibit significant variability and loss of coherent trends (Basu et al., 2011; Godsey et al., 2019; Knapp et al., 2020; Musolff et al., 2015; Olshansky et al., 2018; Raymond & Saiers, 2010; Rose et al., 2018; Thompson et al., 2011).

In all six of our catchments, we observe that $f_{\text{diss}}^{\text{Si}}$ and $\delta^{30}\text{Si}$ solute signatures remain remarkably stable and tightly clustered around their respective flux-weighted average (no overlap between sites). This is despite the fact that TTDs and the fluid flow pathways they describe are known to shift dramatically through the course of infiltration and discharge events, and differ from the TTDs that would describe the same system during periods of quiescence (Benettin, Bailey, et al., 2017; Birkel et al., 2012; Roa-García & Weiler, 2010; Tetzlaff et al., 2014). Further,

silicon is a bio-cycled element, participating in both abiotic weathering and plant uptake pathways (Alexandre et al., 1997; Conley, 2002; Derry et al., 2005; Street-Perrott & Barker, 2008). Thus, Si uptake by plants is considered an active process across sites contributing to observed fractionation (Frings et al., 2021) and we make no suggestion that this effect is negligible. Our model results suggest that in the studied catchments during storm events, the solute signatures exported by these streams are strongly influenced by secondary mineral formation, which appears to be a principal contributor to such tightly bounded $f_{\text{diss}}^{\text{Si}}$ and $\delta^{30}\text{Si}$ signatures.

We find that, even under extreme stress, the site-specific functioning of these catchments is preserved in the silicate solutes they export, indicating a resiliency of these signatures to perturbations. The critical zone architecture inherent in these catchments are imprinted into solute export fluxes where TTDs and reaction pathways still exert first-order control even as these systems are perturbed. Solute signatures of catchments influenced by secondary mineral formation (Sapine, Elder, Providence, La Jara) still differentiate from one another regardless of the stress inflicted. Resiliency, thus, is the preservation of CZ architecture even as storm events overprint the system on shorter timescales. At what point resiliency breaks down under the stress of more frequent and intense extreme events driven by a changing climate presents a substantial unknown that should guide future work.

6. Conclusions

Acknowledgments

This study is part of a cross-CZO (Critical Zone Observatory) international project (SAVI: Science Across Virtual Institutes) involving French, Canadian, and American Critical Zone observatories. Funding sources include NSF grants ICER 1445246 (SAVI), EAR 1331408, EAR 1660923, Agence Nationale de la Recherche project ANR-17-MPGA-0009, and the People Programme (Marie Curie Actions) of the European Union Seventh Framework Programme FP7/2007–2013/ under REA grant agreement n° [608,069]. This project also benefitted from support by the National Science Foundation Graduate Fellowship Program under Grant Nos. DGE-1144245 and by the Chateaubriand Fellowship of the Office of Science & Technology of the Embassy of France in the United States. N.M.F., J.B., and J.L.D. recognize support from US NSF-EAR-2047318. Special acknowledgment is given to Pascale Louvat, Thibaud Sontag, Jean-Sébastien Moquet, Zhengbin Deng, and Damien Guinoiseau for all their assistance with the silicon isotopic analyses. Analytical work was made possible by the IPGP multidisciplinary program PARI and Region Ile-de-France SESAME Grant No. 12015908. We are also thankful to Celine Dessert and Rachael James (Quiock), Jean-François Didon-Lescot, Nadine Grard, Jean-Marc Domergue, Pierre-Alain Ayral, Didier Josselin, and Philippe Martin (Sapine), Maartje Korver, Rob White, Emily Haughton, and Isabelle Desmarais (Hakai), and Carolyn Hunsaker (Providence) for all their collective efforts collecting and supplying the storm event samples. At the Hakai site, we thank William Floyd for the streamflow data and sampling equipment; Paul Sanborn for information about bedrock geology and geochemistry; Heiltsuk and Wuikinuxv Nations for data collected in their traditional territories.

Our cross-site analysis of 157 stream water samples representing seven different storm events from six headwater catchments across the international Critical Zone Observatory network demonstrates no global trend in $\delta^{30}\text{Si}$ as a function of discharge or dissolved Si concentrations, even when bedrock and atmospheric inputs are considered. Consistency between event-scale and longer-term datasets in three of our sites suggest storm events can serve as proxies of long-term silica weathering dynamics. This is consistent with recent cross-site work supporting the notion of events as “snapshots” into long-term variability (Knapp et al., 2020; Minaudo et al., 2019; Rose et al., 2018). Our results highlight the advantage of leveraging storm events, which can comprise significant portions of annual solute export fluxes (40%–80%, Larsen & Simon, 1993; Moatar et al., 2020; Raymond & Saiers, 2010; Yoon & Raymond, 2012), and high frequency geochemical sampling approaches.

A set of three model frameworks were evaluated to determine the underlying factors driving observed variability across sites. Mixing between global Si end members was ruled out as a viable explanation. However, models accounting for multiple fractionation pathways (i.e., reactivity) and variable transit time distributions (i.e., hydrological routing) achieved similar agreement with the observed cross-site behavior. Such accordance offered the opportunity to merge these two distinct conceptualizations, yielding a novel framework based on non-uniform travel time distributions and multiple fractionation pathways. This combined approach indicates that site-to-site differences in hydrological routing characteristics and fractionating reactions are the principal drivers of intra-site variability in observed stream Si solute fluxes and $\delta^{30}\text{Si}$ signatures. Site-specific controls invoked in this study advance recent interpretations from cross-site studies such as Hunsaker & Johnson (2017) and Godsey et al. (2019) who notably proposed that, although chemostasis is commonly observed, each catchment's chemostat is a site-specific signature. This study offers a foundation for further development and application of combined hydrological and biogeochemical models in application to catchment-scale isotopic signatures, suggesting a promising path forward in constraining silicate solute dynamics and weathering rates.

Data Availability Statement

Datasets for this research are hosted on the open source repository CUAHSI HydroShare: <http://www.hydroshare.org/resource/89cfde573936487a9ab4ff406638465b>. DOI for this published resource is 10.4211/hs.89cfde573936487a9ab4ff406638465b (shared under the Creative Commons Attribution CC BY).

References

- Aguirre, A. A. (2019). *Applying Ge/Si ratios to trace weathering reactions, hydrologic pathways and coal fly ash contamination in watersheds across the United States*. Cornell University. <https://doi.org/10.7298/gb60-7y43>
- Aguirre, A. A., Derry, L. A., Mills, T. J., & Anderson, S. P. (2017). Colloidal transport in the Gordon Gulch catchment of the Boulder Creek CZO and its effect on C-Q relationships for silicon. *Water Resources Research*, 53(3), 2368–2383. <https://doi.org/10.1002/2016WR019730>
- Alexandre, A., Meunier, J. D., Colin, F., & Koud, J. M. (1997). Plant impact on the biogeochemical cycle of silicon and related weathering processes. *Geochimica et Cosmochimica Acta*, 61(3), 677–682. [https://doi.org/10.1016/S0016-7037\(97\)00001-X](https://doi.org/10.1016/S0016-7037(97)00001-X)

- Ameijeiras-Maríño, Y., Opfergelt, S., Schoonejans, J., Vanacker, V., Sonnet, P., de Jong, J., & Delmelle, P. (2017). Impact of low denudation rates on soil chemical weathering intensity: A multiproxy approach. *Chemical Geology*, 456, 72–84. <https://doi.org/10.1016/j.chemgeo.2017.03.007>
- Ameli, A. A., Beven, K., Erlandsson, M., Creed, I. F., McDonnell, J. J., & Bishop, K. (2017). Primary weathering rates, water transit times, and concentration-discharge relations: A theoretical analysis for the critical zone. *Water Resources Research*, 53(1), 942–960. <https://doi.org/10.1029/2016WR019448>
- Amiotte Suchet, P., Probst, J.-L., & Ludwig, W. (2003). Worldwide distribution of continental rock lithology: Implications for the atmospheric/soil CO₂ uptake by continental weathering and alkalinity river transport to the oceans. *Global Biogeochemical Cycles*, 17(2). <https://doi.org/10.1029/2002gb001891>
- Anderson, S. P., Dietrich, W. E., Torres, R., Montgomery, D. R., & Loague, K. (1997). Concentration-discharge relationships in runoff from a steep, unchannelled catchment. *Water Resources Research*, 33(1), 211–225. <https://doi.org/10.1029/96WR02715>
- Anderson, S. P., von Blanckenburg, F., & White, A. F. (2007). Physical and chemical controls on the critical zone. *Elements*, 3(5), 315–319. <https://doi.org/10.2113/gselements.3.5.315>
- Arora, B., Burrus, M., Newcomer, M., Steefel, C. I., Carroll, R. W. H., Dwivedi, D., et al. (2020). Differential C-Q analysis: A new approach to inferring lateral transport and hydrologic transients within multiple reaches of a mountainous headwater catchment. *Frontiers in Water*, 2(August), 1–20. <https://doi.org/10.3389/frwa.2020.00024>
- Bales, R. C., Goulden, M. L., Hunsaker, C. T., Conklin, M. H., Hartsough, P. C., O'Geen, A. T., et al. (2018). Mechanisms controlling the impact of multi-year drought on mountain hydrology. *Scientific Reports*, 8(1), 1–8. <https://doi.org/10.1038/s41598-017-19007-0>
- Bales, R. C., Hopmans, J. W., O'Geen, A. T., Meadows, M., Hartsough, P. C., Kirchner, P., et al. (2011). Soil moisture response to snowmelt and rainfall in a Sierra Nevada mixed-conifer forest. *Vadose Zone Journal*, 10(3), 786–799. <https://doi.org/10.2136/vzj2011.10001>
- Bales, R. C., Molotch, N. P., Painter, T. H., Dettinger, M. D., Rice, R., & Dozier, J. (2006). Mountain hydrology of the western United States. *Water Resources Research*, 42(8), 1–13. <https://doi.org/10.1029/2005WR004387>
- Baronas, J. J., Torres, M. A., West, A. J., Rouxel, O., Georg, B., Bouchez, J., et al. (2018). Ge and Si isotope signatures in rivers: A quantitative multi-proxy approach. *Earth and Planetary Science Letters*, 503, 194–215. <https://doi.org/10.1016/j.epsl.2018.09.022>
- Baronas, J. J., West, A. J., Burton, K. W., Hammond, D. E., Opfergelt, S., Pogge von Strandmann, P. A. E., et al. (2020). Ge and Si isotope behavior during intense tropical weathering and ecosystem cycling. *Global Biogeochemical Cycles*, 34(8). <https://doi.org/10.1029/2019GB006522>
- Basu, N. B., Thompson, S. E., & Rao, P. S. C. (2011). Hydrologic and biogeochemical functioning of intensively managed catchments: A synthesis of top-down analyses. *Water Resources Research*, 47(10), 1–13. <https://doi.org/10.1029/2011WR010800>
- Benettin, P., Bailey, S. W., Rinaldo, A., Likens, G. E., McGuire, K. J., & Botter, G. (2017). Young runoff fractions control streamwater age and solute concentration dynamics. *Hydrological Processes*, 31(16), 2982–2986. <https://doi.org/10.1002/hyp.12143>
- Benettin, P., Soulsby, C., Birkel, C., Tetzlaff, D., Botter, G., & Rinaldo, A. (2017). Using SAS functions and high-resolution isotope data to unravel travel time distributions in headwater catchments. *Water Resources Research*, 53(3), 1864–1878. <https://doi.org/10.1002/2016WR020117>
- Birkel, C., Soulsby, C., Tetzlaff, D., Dunn, S., & Spezia, L. (2012). High-frequency storm event isotope sampling reveals time-variant transit time distributions and influence of diurnal cycles. *Hydrological Processes*, 26(2), 308–316. <https://doi.org/10.1002/hyp.8210>
- Blecker, S. W., King, S. L., Derry, L. A., Chadwick, O. A., Ippolito, J. A., & Kelly, E. F. (2007). The ratio of germanium to silicon in plant phytoliths: Quantification of biological discrimination under controlled experimental conditions. *Biogeochemistry*, 86(2), 189–199. <https://doi.org/10.1007/s10533-007-9154-7>
- Bluth, G. J. S., & Kump, L. R. (1994). Lithologic and climatologic controls of river chemistry. *Geochimica et Cosmochimica Acta*, 58(10), 2341–2359. [https://doi.org/10.1016/0016-7037\(94\)90015-9](https://doi.org/10.1016/0016-7037(94)90015-9)
- Bouchez, J., Von Blanckenburg, F., & Schuessler, J. A. (2013). Modeling novel stable isotope ratios in the weathering zone. *American Journal of Science*, 313(4), 267–308. <https://doi.org/10.2475/04.2013.01>
- Boudon, G., Semet, M. P., & Vincent, P. M. (1989). The evolution of La Grande Découverte (La Soufrière) Volcano, Guadeloupe (F.W.I.). In J. H. Latter (Ed.), *Volcanic hazards* (pp. 86–109). Berlin, Heidelberg: Springer. https://doi.org/10.1007/978-3-642-73759-6_5
- Brantley, S. L., Lebedeva, M. I., Balashov, V. N., Singha, K., Sullivan, P. L., & Stinchcomb, G. (2017). Toward a conceptual model relating chemical reaction fronts to water flow paths in hills. *Geomorphology*, 277, 100–117. <https://doi.org/10.1016/j.geomorph.2016.09.027>
- Brichau, S., Respaut, J. P., & Monié, P. (2008). New age constraints on emplacement of the Cévenol granitoids, South French Massif Central. *International Journal of Earth Sciences*, 97(4), 725–738. <https://doi.org/10.1007/s00531-007-0187-x>
- Broxton, D., Woldegabriel, G., Peters, L., Budahn, J., & Luedemann, G. (2007). New Mexico Geological Society volcanic field: Chemistry, petrography, and age constraints. *New Mexico Geological Society Fall Field Conference Guidebook*, 58, 284–295.
- Buss, H. L., White, A. F., Dessert, C., Gaillardet, J., Blum, A. E., & Sak, P. B. (2010). *Depth profiles in a tropical, volcanic critical zone observatory: Basse-Terre, Guadeloupe* (pp. 245–248). Water-Rock Interaction.
- Cardinal, D., Gaillardet, J., Hughes, H. J., Opfergelt, S., & André, L. (2010). Contrasting silicon isotope signatures in rivers from the Congo Basin and the specific behaviour of organic-rich waters. *Geophysical Research Letters*, 37(12), 1–6. <https://doi.org/10.1029/2010GL043413>
- Cenki-Tok, B., Chabaux, F., Lemarchand, D., Schmitt, A. D., Pierret, M. C., Viville, D., et al. (2009). The impact of water-rock interaction and vegetation on calcium isotope fractionation in soil- and stream waters of a small, forested catchment (the Strengbach case). *Geochimica et Cosmochimica Acta*, 73(8), 2215–2228. <https://doi.org/10.1016/j.gca.2009.01.023>
- Chadwick, O. A., Derry, L. A., Vitousek, P. M., Huebert, B. J., & Hedin, L. O. (1999). Changing sources of nutrients during four million years of ecosystem development. *Nature*, 397(6719), 491–497. <https://doi.org/10.1038/17276>
- Clergue, C., Dellinger, M., Buss, H. L., Gaillardet, J., Benedetti, M. F., & Dessert, C. (2015). Influence of atmospheric deposits and secondary minerals on Li isotopes budget in a highly weathered catchment, Guadeloupe (Lesser Antilles). *Chemical Geology*, 414, 28–41. <https://doi.org/10.1016/j.chemgeo.2015.08.015>
- Cognard-Plancq, A. L., Marc, V., Didon-Lescot, J. F., & Normand, M. (2001). The role of forest cover on streamflow down sub-Mediterranean mountain watersheds: A modelling approach. *Journal of Hydrology*, 254(1–4), 229–243. [https://doi.org/10.1016/S0022-1694\(01\)00494-2](https://doi.org/10.1016/S0022-1694(01)00494-2)
- Colmet-Daage, F., & Bernard, Z. (1979). Contribution à l'Atlas des départements d'Outre-mer: Guadeloupe. In *ORSTOM, Antilles, Cartes des sols de la Guadeloupe, Grand-Terre, Marie-Galante. Carte des pentes et du modèle de la Guadeloupe, Grand-Terre, Marie-Galante*.
- Conley, D. J. (2002). Terrestrial ecosystems and the global biogeochemical silica cycle. *Global Biogeochemical Cycles*, 16(4), 68–1–68–8. <https://doi.org/10.1029/2002gb001894>
- Coop, J. D., & Givnish, T. J. (2007). Gradient analysis of reversed treelines and grasslands of the Valles Caldera, New Mexico. *Journal of Vegetation Science*, 18(1), 43. <https://doi.org/10.1111/j.1654-1103.2007.tb02514.x>
- Coplen, T. B. (2011). Guidelines and recommended terms for expression of stable-isotope-ratio and gas-ratio measurement results. *Rapid Communications in Mass Spectrometry*, 25(17), 2538–2560. <https://doi.org/10.1002/rcm.5129>
- Dauphas, N., Pourmand, A., & Teng, F. Z. (2009). Routine isotopic analysis of iron by HR-MC-ICPMS: How precise and how accurate? *Chemical Geology*, 267(3–4), 175–184. <https://doi.org/10.1016/j.chemgeo.2008.12.011>

- Davis, S. N. (1964). Silica in streams and ground water. *American Journal of Science*, 262(7), 870–891. <https://doi.org/10.2475/ajs.262.7.870>
- De La Rocha, C. L., Brzezinski, M. A., & Deniro, M. J. (2000). A first look at the distribution of the stable isotopes of silicon in natural waters. *Geochimica et Cosmochimica Acta*, 64(14), 2467–2477. [https://doi.org/10.1016/S0016-7037\(00\)00373-2](https://doi.org/10.1016/S0016-7037(00)00373-2)
- Dellinger, M., Gaillardet, J., Bouchez, J., Calmels, D., Louvat, P., Dosseto, A., et al. (2015). Riverine Li isotope fractionation in the Amazon River basin controlled by the weathering regimes. *Geochimica et Cosmochimica Acta*, 164, 71–93. <https://doi.org/10.1016/j.gca.2015.04.042>
- Derry, L. A., & Chadwick, O. A. (2007). Contributions from Earth's atmosphere to soil. *Elements*, 3, 333–338. <https://doi.org/10.2113/gselements.3.5.333>
- Derry, L. A., Kurtz, A. C., Ziegler, K., & Chadwick, O. A. (2005). Biological control of terrestrial silica cycling and export fluxes to watersheds. *Nature*, 433(7027), 728–731. <https://doi.org/10.1038/nature03299>
- Dessert, C., Clergue, C., Roustéau, A., Crispé, O., & Benedetti, M. F. (2020). Atmospheric contribution to cations cycling in highly weathered catchment, Guadeloupe (Lesser Antilles). *Chemical Geology*, 531(November 2019), 119354. <https://doi.org/10.1016/j.chemgeo.2019.119354>
- Dessert, C., Dupré, B., Gaillardet, J., François, L. M., & Allègre, C. J. (2003). Basalt weathering laws and the impact of basalt weathering on the global carbon cycle. *Chemical Geology*, 202(3–4), 257–273. <https://doi.org/10.1016/j.chemgeo.2002.10.001>
- Dessert, C., Lajeunesse, E., Lloret, E., Clergue, C., Crispé, O., Gorge, C., & Quidelleur, X. (2015). Controls on chemical weathering on a mountainous volcanic tropical island: Guadeloupe (French West Indies). *Geochimica et Cosmochimica Acta*, 171, 216–237. <https://doi.org/10.1016/j.gca.2015.09.009>
- Dia, A., Chauvel, C., Bulourde, M., & Gérard, M. (2006). Eolian contribution to soils on Mount Cameroon: Isotopic and trace element records. *Chemical Geology*, 226(3–4), 232–252. <https://doi.org/10.1016/j.chemgeo.2005.09.022>
- Ding, T., Wan, D., Wang, C., & Zhang, F. (2004). Silicon isotope compositions of dissolved silicon and suspended matter in the Yangtze River, China. *Geochimica et Cosmochimica Acta*, 68(2), 205–216. [https://doi.org/10.1016/S0016-7037\(03\)00264-3](https://doi.org/10.1016/S0016-7037(03)00264-3)
- Ding, T. P., Zhou, J. X., Wan, D. F., Chen, Z. Y., Wang, C. Y., & Zhang, F. (2008). Silicon isotope fractionation in bamboo and its significance to the biogeochemical cycle of silicon. *Geochimica et Cosmochimica Acta*, 72(5), 1381–1395. <https://doi.org/10.1016/j.gca.2008.01.008>
- Dixon, J. L., Heimsath, A. M., & Amundson, R. (2009). The critical role of climate and saprolite weathering in landscape evolution. *Earth Surface Processes and Landforms*, 34(11), 1507–1521. <https://doi.org/10.1002/esp.1836>
- Drever, J. I., & Clow, D. W. (1995). Weathering rates in catchments. *Reviews in Mineralogy and Geochemistry*, 31(1), 463–483. <https://doi.org/10.1515/9781501509650-012>
- Drever, J. I., & Zobrist, J. (1992). Chemical weathering of silicate rocks as a function of elevation in the southern Swiss Alps. *Geochimica et Cosmochimica Acta*, 56(8), 3209–3216. [https://doi.org/10.1016/0016-7037\(92\)90298-W](https://doi.org/10.1016/0016-7037(92)90298-W)
- Druhan, J. L., & Maher, K. (2017). The influence of mixing on stable isotope ratios in porous media: A revised Rayleigh model. *Water Resources Research*, 53(2), 1101–1124. <https://doi.org/10.1002/2016WR019666>
- Druhan, J. L., Winnick, M. J., & Thullner, M. (2019). Stable isotope fractionation by transport and transformation. *Reviews in Mineralogy and Geochemistry*, 85(1), 239–264. <https://doi.org/10.2138/rmg.2019.85.8>
- Durand, P., Neal, C., & Lelong, F. (1992). Anthropogenic and natural contributions to the rainfall chemistry of a mountainous area in the Cevennes National Park (Mont-Lozère, southern France). *Journal of Hydrology*, 130(1–4), 71–85. [https://doi.org/10.1016/0022-1694\(92\)90104-4](https://doi.org/10.1016/0022-1694(92)90104-4)
- Dwivedi, D., Arora, B., Steefel, C. I., Dafflon, B., & Versteeg, R. (2018). Hot spots and hot moments of nitrogen in a riparian corridor. *Water Resources Research*, 54(1), 205–222. <https://doi.org/10.1002/2017WR022346>
- Edmond, J. M., Palmer, M. R., Measures, C. I., Grant, B., & Stallard, R. F. (1995). The fluvial geochemistry and denudation rate of the Guayana Shield in Venezuela, Colombia, and Brazil. *Geochimica et Cosmochimica Acta*, 59(16), 3301–3325. [https://doi.org/10.1016/0016-7037\(95\)00128-M](https://doi.org/10.1016/0016-7037(95)00128-M)
- Engelstaedter, S., Tegen, I., & Washington, R. (2006). North African dust emissions and transport. *Earth-Science Reviews*, 79(1–2), 73–100. <https://doi.org/10.1016/j.earscirev.2006.06.004>
- Engström, E., Rodushkin, I., Ingri, J., Baxter, D. C., Ecke, F., Österlund, H., & Öhländer, B. (2010). Temporal isotopic variations of dissolved silicon in a pristine boreal river. *Chemical Geology*, 271(3–4), 142–152. <https://doi.org/10.1016/j.chemgeo.2010.01.005>
- Fernandez, N. M., Perez-Fodich, A., Derry, L. A., & Druhan, J. L. (2021). A first look at Ge/Si partitioning during amorphous silica precipitation: Implications for Ge/Si as a tracer of fluid-silicate interactions. *Geochimica et Cosmochimica Acta*, 297, 158–178. <https://doi.org/10.1016/j.gca.2021.01.007>
- Fernandez, N. M., Zhang, X., & Druhan, J. L. (2019). Silicon isotopic re-equilibration during amorphous silica precipitation and implications for isotopic signatures in geochemical proxies. *Geochimica et Cosmochimica Acta*, 262, 104–127. <https://doi.org/10.1016/j.gca.2019.07.029>
- Floury, P., Gaillardet, J., Gayer, E., Bouchez, J., Tallec, G., Ansart, P., et al. (2017). The Potamochemical symphony: New progresses in the high frequency acquisition of stream chemical data. *Hydrology and Earth System Sciences Discussions*, 1–41. <https://doi.org/10.5194/hess-2017-12>
- Frick, D. A., Remus, R., Sommer, M., Augustin, J., Kaczorek, D., & Von Blanckenburg, F. (2020). Silicon uptake and isotope fractionation dynamics by crop species. *Biogeosciences*, 17(24), 6475–6490. <https://doi.org/10.5194/bg-17-6475-2020>
- Fries, D. M., James, R. H., Dessert, C., Bouchez, J., Beaumais, A., & Pearce, C. R. (2019). The response of Li and Mg isotopes to rain events in a highly-weathered catchment. *Chemical Geology*, 519(November 2018), 68–82. <https://doi.org/10.1016/j.chemgeo.2019.04.023>
- Frings, P. J., Clymans, W., Fontorbe, G., De La Rocha, C. L., & Conley, D. J. (2016). The continental Si cycle and its impact on the ocean Si isotope budget. *Chemical Geology*, 425, 12–36. <https://doi.org/10.1016/j.chemgeo.2016.01.020>
- Frings, P. J., Oelze, M., Schubring, F., Frick, D. A., & von Blanckenburg, F. (2021). Interpreting silicon isotopes in the critical zone. *American Journal of Science*, 321, 1164–1203. <https://doi.org/10.2475/08.2021.02>
- Gabrielli, C. P., Morgenstern, U., Stewart, M. K., & McDonnell, J. J. (2018). Contrasting groundwater and streamflow ages at the Maimai Watershed. *Water Resources Research*, 54(6), 3937–3957. <https://doi.org/10.1029/2017WR021825>
- Gaillardet, J., Braud, I., Hankard, F., Anquetin, S., Bour, O., Dorfliger, N., et al. (2018). OZCAR: The French network of critical zone observatories. *Vadose Zone Journal*, 17(1), 180067. <https://doi.org/10.2136/vzj2018.04.0067>
- Gaillardet, J., Dupré, B., Louvat, P., & Allègre, C. J. (1999). Global silicate weathering and CO₂ consumption rates deduced from the chemistry of large rivers. *Chemical Geology*, 159(1–4), 3–30. [https://doi.org/10.1016/S0009-2541\(99\)00031-5](https://doi.org/10.1016/S0009-2541(99)00031-5)
- Gaillardet, J., Rad, S., Rivé, K., Louvat, P., Gorge, C., Allègre, C. J., & Lajeunesse, E. (2011). Orography-driven chemical denudation in the lesser antilles: Evidence for a new feed-back mechanism stabilizing atmospheric CO₂. *American Journal of Science*, 311(10), 851–894. <https://doi.org/10.2475/10.2011.02>
- Garrels, R. M., & MacKenzie, F. T. (1971). *Evolution of Sedimentary Rocks*. New York: W.W. Norton and Company, Inc.
- Gaspard, F., Opfergelt, S., Dessert, C., Robert, V., Ameijeiras-Mariño, Y., & Delmelle, P. (2021). Imprint of chemical weathering and hydrothermalism on the Ge/Si ratio and Si isotope composition of rivers in a volcanic tropical island, Basse-Terre, Guadeloupe (French West Indies). *Chemical Geology*, 577(April). <https://doi.org/10.1016/j.chemgeo.2021.120283>

- Geilert, S., Vroon, P. Z., Roerdink, D. L., Van Cappellen, P., & van Bergen, M. J. (2014). Silicon isotope fractionation during abiotic silica precipitation at low temperatures: Inferences from flow-through experiments. *Geochimica et Cosmochimica Acta*, 142(1), 95–114. <https://doi.org/10.1016/j.gca.2014.07.003>
- Georg, R. B., Reynolds, B. C., Frank, M., & Halliday, A. N. (2006a). Mechanisms controlling the silicon isotopic compositions of river waters. *Earth and Planetary Science Letters*, 249(3–4), 290–306. <https://doi.org/10.1016/j.epsl.2006.07.006>
- Georg, R. B., Reynolds, B. C., Frank, M., & Halliday, A. N. (2006b). New sample preparation techniques for the determination of Si isotopic compositions using MC-ICPMS. *Chemical Geology*, 235(1–2), 95–104. <https://doi.org/10.1016/j.chemgeo.2006.06.006>
- Georg, R. B., Reynolds, B. C., West, A. J., Burton, K. W., & Halliday, A. N. (2007). Silicon isotope variations accompanying basalt weathering in Iceland. *Earth and Planetary Science Letters*, 261(3–4), 476–490. <https://doi.org/10.1016/j.epsl.2007.07.004>
- Georg, R. B., West, A. J., Basu, A. R., & Halliday, A. N. (2009). Silicon fluxes and isotope composition of direct groundwater discharge into the Bay of Bengal and the effect on the global ocean silicon isotope budget. *Earth and Planetary Science Letters*, 283(1–4), 67–74. <https://doi.org/10.1016/j.epsl.2009.03.041>
- Giesbrecht, I. J. W., Floyd, W. C., Tank, S. E., Lertzman, K. P., Hunt, B. P. V., Korver, M. C., et al. (2021). The Kwakshua Watersheds Observatory, central coast of British Columbia, Canada. *Hydrological Processes*, 35(6), 1–10. <https://doi.org/10.1002/hyp.14198>
- Gíslason, S. D. S. R., Arnórsson, S., & Ármannsson, H. (1996). Chemical weathering of basalt in Southwest Iceland: Effects of runoff, age of rocks and vegetative/glacial cover. *American Journal of Science*. <https://doi.org/10.2475/ajs.296.8.837>
- Godsey, S. E., Hartmann, J., & Kirchner, J. W. (2019). Catchment chemostasis revisited: Water quality responds differently to variations in weather and climate. *Hydrological Processes*, 33(24), 3056–3069. <https://doi.org/10.1002/hyp.13554>
- Godsey, S. E., Kirchner, J. W., & Clow, D. W. (2009). Concentration-discharge relationships reflect chemostatic characteristics of US catchments. *Hydrological Processes*, 23(13), 1844–1864. <https://doi.org/10.1002/hyp.7315>
- Golla, J. K., Kueßner, M. L., Henehan, M. J., Bouchez, J., Rempe, D. M., & Druhan, J. L. (2021). The evolution of lithium isotope signatures in fluids draining actively weathering hillslopes. *Earth and Planetary Science Letters*, 567, 116988. <https://doi.org/10.1016/j.epsl.2021.116988>
- Gu, X., Rempe, D. M., Dietrich, W. E., West, A. J., Lin, T. C., Jin, L., & Brantley, S. L. (2020). Chemical reactions, porosity, and microfracturing in shale during weathering: The effect of erosion rate. *Geochimica et Cosmochimica Acta*, 269, 63–100. <https://doi.org/10.1016/j.gca.2019.09.044>
- Guérin, A., Devauchelle, O., Robert, V., Kitou, T., Dessert, C., Quiquerez, A., et al. (2019). Stream-discharge surges generated by groundwater flow. *Geophysical Research Letters*, 46(13), 7447–7455. <https://doi.org/10.1029/2019GL082291>
- Guerzoni, S., Molinaroli, E., Rossini, P., Rampazzo, G., Quarantotto, G., de Falco, G., & Cristini, S. (1999). Role of desert aerosol in metal fluxes in the Mediterranean area. *Chemosphere*, 39(2), 229–246. [https://doi.org/10.1016/S0045-6535\(99\)00105-8](https://doi.org/10.1016/S0045-6535(99)00105-8)
- Hahn, W. J., Dralle, D. N., Lovill, S. M., Rose, J., Dawson, T. E., & Dietrich, W. E. (2017). Exploratory Tree Survey (2016—Eel River Critical Zone Observatory—Sagehorn—Central Belt Melange, Franciscan Complex, Northern California Coast Ranges, USA). *HydroShare*. <https://doi.org/10.4211/hs.7881821a5c0e4ae3822b96a59f4bf886>
- Hahn, W. J., Riebe, C. S., Lukens, C. E., & Araki, S. (2014). Bedrock composition regulates mountain ecosystems and landscape evolution. *Proceedings of the National Academy of Sciences of the United States of America*, 111(9), 3338–3343. <https://doi.org/10.1073/pnas.1315667111>
- Harman, C. J. (2015). Time-variable transit time distributions and transport: Theory and application to storage-dependent transport of chloride in a watershed. *Water Resources Research*, 51(1), 1–30. <https://doi.org/10.1002/2014WR015707>
- Henderson, A. K., & Shuman, B. N. (2010). Differing controls on river- and lake-water hydrogen and oxygen isotopic values in the western United States. *Hydrological Processes*, 24(26), 3894–3906. <https://doi.org/10.1002/hyp.7824>
- Holbrook, W. S., Riebe, C. S., Elwaseif, M., Hayes, J. L., Basler-Reeder, K., Harry, D. L., et al. (2014). Geophysical constraints on deep weathering and water storage potential in the Southern Sierra Critical Zone Observatory. *Earth Surface Processes and Landforms*, 39(3), 366–380. <https://doi.org/10.1002/esp.3502>
- Hornberger, G. M., Scanlon, T. M., & Raffensperger, J. P. (2001). Modelling transport of dissolved silica in a forested headwater catchment: The effect of hydrological and chemical time scales on hysteresis in the concentration-discharge relationship. *Hydrological Processes*, 15(10), 2029–2038. <https://doi.org/10.1002/hyp.254>
- Hughes, H. J., Bouillon, S., André, L., & Cardinal, D. (2012). The effects of weathering variability and anthropogenic pressures upon silicon cycling in an intertropical watershed (Tana River, Kenya). *Chemical Geology*, 308–309, 18–25. <https://doi.org/10.1016/j.chemgeo.2012.03.016>
- Hughes, H. J., Delvigne, C., Kornthauer, M., De Jong, J., André, L., & Cardinal, D. (2011). Controlling the mass bias introduced by anionic and organic matrices in silicon isotopic measurements by MC-ICP-MS. *Journal of Analytical Atomic Spectrometry*, 26(9), 1892–1896. <https://doi.org/10.1039/c1ja10110b>
- Hughes, H. J., Sondag, F., Santos, R. V., André, L., & Cardinal, D. (2013). The riverine silicon isotope composition of the Amazon Basin. *Geochimica et Cosmochimica Acta*, 121, 637–651. <https://doi.org/10.1016/j.gca.2013.07.040>
- Huh, Y., Chan, L. H., Zhang, L., & Edmond, J. M. (1998). Lithium and its isotopes in major world rivers: Implications for weathering and the oceanic budget. *Geochimica et Cosmochimica Acta*, 62(12), 2039–2051. [https://doi.org/10.1016/S0016-7037\(98\)00126-4](https://doi.org/10.1016/S0016-7037(98)00126-4)
- Hunsaker, C. (2013). The Kings River Experimental Watersheds: New findings about headwater streams of the southern Sierra Nevada. *Mountain Views*, 7(1), 6–9. Retrieved from <https://www.fs.usda.gov/treesearch/pubs/44859>
- Hunsaker, C. (2019). SSCZO—Streamflow/Discharge—Providence—(2003–2010). *HydroShare*.
- Hunsaker, C. T., & Johnson, D. W. (2017). Concentration-discharge relationships in headwater streams of the Sierra Nevada, California. *Water Resources Research*, 53(9), 7869–7884. <https://doi.org/10.1002/2016WR019693>
- Hunsaker, C. T., Whitaker, T. W., & Bales, R. C. (2012). Snowmelt runoff and water yield along elevation and temperature gradients in California's Southern Sierra Nevada. *Journal of the American Water Resources Association*, 48(4), 667–678. <https://doi.org/10.1111/j.1752-1688.2012.00641.x>
- Imbert, D., Roustau, A., & Labb  , P. (1998). Ouragans et diversit   biologique dans les for  ts tropicales. L'exemple de la Guadeloupe. *Acta Oecologica*, 19(3), 251–262. [https://doi.org/10.1016/S1146-609X\(98\)80029-5](https://doi.org/10.1016/S1146-609X(98)80029-5)
- Jochum, K. P., Weis, U., Schwager, B., Stoll, B., Wilson, S. A., Haug, G. H., et al. (2016). Reference values following ISO guidelines for frequently requested rock reference materials. *Geostandards and Geoanalytical Research*, 40(3), 333–350. <https://doi.org/10.1111/j.1751-908X.2015.00392.x>
- Kennedy, M. J., Chadwick, O. A., Vitousek, P. M., Derry, L. A., & Hendricks, D. M. (1998). Changing sources of base cations during ecosystem development, Hawaiian Islands. *Geology*, 26(11), 1015–1018. [https://doi.org/10.1130/0091-7613\(1998\)026<1015:csobed>2.3.co;2](https://doi.org/10.1130/0091-7613(1998)026<1015:csobed>2.3.co;2)
- Kennedy, V. C. (1971). Silica variation in stream water with time and discharge. In *Nonequilibrium systems in natural water chemistry* (Vol. 106, pp. 4–94). American Chemical Society. <https://doi.org/10.1021/ba-1971-0106.ch004>
- Keresztesi, A., Nita, I. A., Boga, R., Birsan, M. V., Bodor, Z., & Sz  p, R. (2020). Spatial and long-term analysis of rainwater chemistry over the conterminous United States. *Environmental Research*, 188. <https://doi.org/10.1016/j.envres.2020.109872>

- Kim, H., Bishop, J. K. B., Dietrich, W. E., & Fung, I. Y. (2014). Process dominance shift in solute chemistry as revealed by long-term high-frequency water chemistry observations of groundwater flowing through weathered argillite underlying a steep forested hillslope. *Geochimica et Cosmochimica Acta*, 140, 1–19. <https://doi.org/10.1016/j.gca.2014.05.011>
- Kim, H., Dietrich, W. E., Thurnhoffer, B. M., Bishop, J. K. B., & Yung, I. Y. (2017). Controls on solute concentration-discharge relationships revealed by simultaneous hydrochemistry observations of hillslope runoff and stream flow: The importance of critical zone structure. *Water Resources Research*, 53, 1424–1443. <https://doi.org/10.1002/2016WR019722>
- Kirchner, J. W., Feng, X., & Neal, C. (2000). Fractal chemistry and its implications for contaminant transport in catchments. *Nature*, 403(6769), 524–527. <https://doi.org/10.1038/35000537>
- Kirchner, J. W., Feng, X., & Neal, C. (2001). Catchment-scale advection and dispersion as a mechanism for fractal scaling in stream tracer concentrations. *Journal of Hydrology*, 254(1–4), 82–101. [https://doi.org/10.1016/S0022-1694\(01\)00487-5](https://doi.org/10.1016/S0022-1694(01)00487-5)
- Knapp, J. L. A., Von Freyberg, J., Studer, B., Kiewiet, L., & Kirchner, J. W. (2020). Concentration-discharge relationships vary among hydrological events, reflecting differences in event characteristics. *Hydrology and Earth System Sciences*, 24(5), 2561–2576. <https://doi.org/10.5194/hess-24-2561-2020>
- Korver, M. C., Floyd, W. C., & Brunsting, R. (2020). *Discharge time series (2013–2019)—Calvert Island—Archived Version 4.1*. Hakai Institute. <https://doi.org/10.21966/zvwt-qn04>
- Küßner, M. L. (2018). *The interplay between chemical weathering and hydrology in the Critical Zone- insight from trace elements and lithium isotopes*.
- Kurtz, A. C., Derry, L. A., & Chadwick, O. A. (2001). Accretion of Asian dust to Hawaiian soils: Isotopic, elemental, and mineral mass balances. *Geochimica et Cosmochimica Acta*, 65(12), 1971–1983. [https://doi.org/10.1016/S0016-7037\(01\)00575-0](https://doi.org/10.1016/S0016-7037(01)00575-0)
- Kurtz, A. C., Derry, L. A., & Chadwick, O. A. (2002). Germanium—Silicon fractionation in the weathering environment. *Geochimica et Cosmochimica Acta*, 66(9), 1525–1537. [https://doi.org/10.1016/s0016-7037\(01\)00869-9](https://doi.org/10.1016/s0016-7037(01)00869-9)
- Kurtz, A. C., Lugolobi, F., & Salvucci, G. (2011). Germanium-silicon as a flow path tracer: Application to the Rio Icacos watershed. *Water Resources Research*, 47(6), 1–16. <https://doi.org/10.1029/2010WR009853>
- Larsen, M. C., & Simon, A. (1993). A rainfall intensity-duration threshold for landslides in a humid-tropical environment, Puerto Rico. *Geografiska Annaler: Series A, Physical Geography*, 75(1–2), 13–23. <https://doi.org/10.1080/04353676.1993.11880379>
- Levy-Booth, D. J., Giesbrecht, I. J. W., Kellogg, C. T. E., Heger, T. J., D'Amore, D. V., Keeling, P. J., et al. (2019). Seasonal and ecohydrological regulation of active microbial populations involved in DOC, CO₂, and CH₄ fluxes in temperate rainforest soil. *ISME Journal*, 13(4), 950–963. <https://doi.org/10.1038/s41396-018-0334-3>
- Lin, H. (2010). Earth's Critical Zone and hydropedology: Concepts, characteristics, and advances. *Hydrology and Earth System Sciences*, 14(1), 25–45. <https://doi.org/10.5194/hess-14-25-2010>
- Liu, F., Hunsaker, C., & Bales, R. C. (2013). Controls of streamflow generation in small catchments across the snow-rain transition in the Southern Sierra Nevada, California. *Hydrological Processes*, 27(14), 1959–1972. <https://doi.org/10.1002/hyp.9304>
- Liu, F., Parmenter, R., Brooks, P. D., Conklin, M. H., & Bales, R. C. (2008). Seasonal and interannual variation of streamflow pathways and biogeochemical implications in semi-arid, forested catchments in Valles Caldera, New Mexico. *Ecohydrology*, 1(3), 239–252. <https://doi.org/10.1002/eco.22>
- Lloret, E., Dessert, C., Gaillardet, J., Albéric, P., Crispi, O., Chaduteau, C., & Benedetti, M. F. (2011). Comparison of dissolved inorganic and organic carbon yields and fluxes in the watersheds of tropical volcanic islands, examples from Guadeloupe (French West Indies). *Chemical Geology*, 280(1–2), 65–78. <https://doi.org/10.1016/j.chemgeo.2010.10.016>
- Lugolobi, F., Kurtz, A. C., & Derry, L. A. (2010). Germanium-silicon fractionation in a tropical, granitic weathering environment. *Geochimica et Cosmochimica Acta*, 74(4), 1294–1308. <https://doi.org/10.1016/j.gca.2009.11.027>
- Maher, K. (2010). The dependence of chemical weathering rates on fluid residence time. *Earth and Planetary Science Letters*, 294(1–2), 101–110. <https://doi.org/10.1016/j.epsl.2010.03.010>
- Maher, K. (2011). The role of fluid residence time and topographic scales in determining chemical fluxes from landscapes. *Earth and Planetary Science Letters*, 312(1–2), 48–58. <https://doi.org/10.1016/j.epsl.2011.09.040>
- Maloszewski, P., & Zuber, A. (1996). *Lumped parameter models for the interpretation of environmental tracer data*. International Atomic Energy Agency (IAEA). Retrieved from http://inis.iaea.org/search/search.aspx?orig_q=RN:28020904
- Marc, V., Didon-Lescot, J. F., & Michael, C. (2001). Investigation of the hydrological processes using chemical and isotopic tracers in a small Mediterranean forested catchment during autumn recharge. *Journal of Hydrology*, 247(3–4), 215–229. [https://doi.org/10.1016/S0022-1694\(01\)00386-9](https://doi.org/10.1016/S0022-1694(01)00386-9)
- Martin, C., Didon-Lescot, J.-F., Cosandey, C., & Le, C. C. (2003). *Le fonctionnement hydrologique des petits bassins versants granitiques du Mont-Lozère: Influence du couvert végétal sur les crues et les étiages*. Retrieved from <https://hal.archives-ouvertes.fr/hal-00312824>
- McClain, M. E., Boyer, E. W., Dent, C. L., Gergel, S. E., Grimm, N. B., Groffman, P. M., et al. (2003). Biogeochemical hot spots and hot moments at the interface of terrestrial and aquatic ecosystems. *Ecosystems*, 6(4), 301–312. <https://doi.org/10.1007/s10021-003-0161-9>
- McGuire, K. J., & McDonnell, J. J. (2006). A review and evaluation of catchment transit time modeling. *Journal of Hydrology*, 330(3–4), 543–563. <https://doi.org/10.1016/j.jhydrol.2006.04.020>
- McGuire, K. J., & McDonnell, J. J. (2010). Hydrological connectivity of hillslopes and streams: Characteristic time scales and nonlinearities. *Water Resources Research*, 46(10), 1–17. <https://doi.org/10.1029/2010WR009341>
- McIntosh, J., Brooks, P., Amistadi, M. K., Corley, T., Zapata-Rios, X., Perdrial, J., et al. (2020). Water chemistry for La Jara Creek and nearby springs in the Jemez River Basin Critical Zone Observatory, Valles Caldera Preserve, New Mexico (2010–2013). *HydroShare*. Retrieved from <http://www.hydroshare.org/resource/88816227c50141a298192a3b75863008%0A>
- McIntosh, J. C., Schaumberg, C., Perdrial, J., Harpold, A., Vázquez-Ortega, A., & Rasmussen, C. (2017). Geochemical evolution of the Critical Zone across variable time scales informs concentration-discharge relationships: Jemez River Basin Critical Zone Observatory. *Water Resources Research*, 53(5), 4169–4196. <https://doi.org/10.1002/2016WR019712>
- McLaughlin, R. J., Ellen, S. D., Blake, M. C., Jr., Jayko, A. S., Irwin, W. P., Aalto, K. R., et al. (2000). Geology of the Cape Mendocino, Eureka, Garberville, and southwestern part of the Hayfork 30 × 60 minute quadrangles and adjacent offshore area, northern California (online version 1.0.). *Miscellaneous Field Studies Map*. <https://doi.org/10.3133/mf2336>
- Meek, K., Derry, L., Sparks, J., & Cathles, L. (2016). 87Sr/86Sr, Ca/Sr, and Ge/Si ratios as tracers of solute sources and biogeochemical cycling at a temperate forested shale catchment, central Pennsylvania, USA. *Chemical Geology*, 445, 84–102. <https://doi.org/10.1016/j.chemgeo.2016.04.026>
- Meybeck, M. (1987). Global chemical weathering of surficial rocks estimated from river dissolved loads. *American Journal of Science*. <https://doi.org/10.2475/ajs.287.5.401>

- Millot, R., Gaillardet, J., Dupré, B., & Allègre, C. J. (2002). The global control of silicate weathering rates and the coupling with physical erosion: New insights from rivers of the Canadian Shield. *Earth and Planetary Science Letters*, 196(1–2), 83–98. [https://doi.org/10.1016/S0012-821X\(01\)00599-4](https://doi.org/10.1016/S0012-821X(01)00599-4)
- Minaudo, C., Dupas, R., Gascuel-Odoux, C., Roubeix, V., Danis, P. A., & Moatar, F. (2019). Seasonal and event-based concentration-discharge relationships to identify catchment controls on nutrient export regimes. *Advances in Water Resources*, 131(July), 103379. <https://doi.org/10.1016/j.advwatres.2019.103379>
- Moatar, F., Floury, M., Gold, A. J., Meybeck, M., Renard, B., Ferréol, M., et al. (2020). Stream solutes and particulates export regimes: A new framework to optimize their monitoring. *Frontiers in Ecology and Evolution*, 7(January), 1–19. <https://doi.org/10.3389/fevo.2019.00516>
- Moravec, B. G., White, A. M., Root, R. A., Sanchez, A., Olshansky, Y., Paras, B. K., et al. (2020). Resolving deep critical zone architecture in complex volcanic terrain. *Journal of Geophysical Research: Earth Surface*, 125(1), 1–24. <https://doi.org/10.1029/2019JF005189>
- Mortlock, R. A., & Froelich, P. N. (1996). Determination of germanium by isotope dilution-hydride generation inductively coupled plasma mass spectrometry. *Analytica Chimica Acta*, 332(2–3), 277–284. [https://doi.org/10.1016/0003-2670\(96\)00230-9](https://doi.org/10.1016/0003-2670(96)00230-9)
- Muldavin, E., Tonne, P., Jackson, C., & Neville, T. (2006). A vegetation map of the Valles Caldera National Preserve, New Mexico. *Final Report for Cooperative Agreement*. Retrieved from <http://scholar.google.com/scholar?hl=en&btnG=Search&q=intitle:A+vegetation+map+of+the+Valles+Caldera+National+Preserve++New+Mexico#>
- Musolff, A., Schmidt, C., Selle, B., & Fleckenstein, J. H. (2015). Catchment controls on solute export. *Advances in Water Resources*, 86, 133–146. <https://doi.org/10.1016/j.advwatres.2015.09.026>
- National Atmospheric Deposition Program (NRSP-3). (2020). *Wisconsin State Laboratory of Hygiene*. NADP Program Office.
- National Research Council. (2001). Basic research opportunities in Earth Science. *Basic Research Opportunities in Earth Science*. <https://doi.org/10.17226/9981>
- Nelson, L. A., Sanborn, P., Cade-Menun, B. J., Walker, I. J., & Lian, O. B. (2021). Pedological trends and implications for forest productivity in a Holocene soil chronosequence, Calvert Island, British Columbia, Canada. *Canadian Journal of Soil Science*, 101(4), 654–672. <https://doi.org/10.1139/cjss-2021-0033>
- O'Geen, A. T., Safeeq, M., Wagenbrenner, J., Stacy, E., Hartsough, P., Devine, S., et al. (2018). Southern sierra critical zone observatory and kings river experimental watersheds: A synthesis of measurements, new insights, and future directions. *Vadose Zone Journal*, 17(1), 180081. <https://doi.org/10.2136/vzj2018.04.0081>
- Oelze, M., Schuessler, J. A., & Von Blanckenburg, F. (2016). Mass bias stabilization by Mg doping for Si stable isotope analysis by MC-ICP-MS. *Journal of Analytical Atomic Spectrometry*, 31(10), 2094–2100. <https://doi.org/10.1039/cfja00218h>
- Oliva, P., Viers, J., & Dupré, B. (2003). Chemical weathering in granitic environments. *Chemical Geology*, 202(3–4), 225–256. <https://doi.org/10.1016/j.chemgeo.2002.08.001>
- Oliver, A. A., Tank, S. E., Giesbrecht, I., Korver, M. C., Floyd, W. C., Sanborn, P., et al. (2017). A global hotspot for dissolved organic carbon in hypermaritime watersheds of coastal British Columbia. *Biogeosciences*, 14(15), 3743–3762. <https://doi.org/10.5194/bg-14-3743-2017>
- Olshansky, Y., White, A. M., Moravec, B. G., McIntosh, J., & Chorover, J. (2018). Subsurface pore water contributions to stream concentration-discharge relations across a snowmelt hydrograph. *Frontiers in Earth Science*, 6(November), 1–18. <https://doi.org/10.3389/feart.2018.00181>
- Olyphant, J., Pelletier, J. D., & Johnson, R. (2016). Topographic correlations with soil and regolith thickness from shallow-seismic refraction constraints across upland hillslopes in the Valles Caldera, New Mexico. *Earth Surface Processes and Landforms*, 41(12), 1684–1696. <https://doi.org/10.1002/esp.3941>
- Opfergelt, S., Cardinal, D., André, L., Delvigne, C., Bremond, L., & Delvaux, B. (2010). Variations of 630Si and Ge/Si with weathering and biogenic input in tropical basaltic ash soils under monoculture. *Geochimica et Cosmochimica Acta*, 74(1), 225–240. <https://doi.org/10.1016/j.gca.2009.09.025>
- Opfergelt, S., & Delmelle, P. (2012). Silicon isotopes and continental weathering processes: Assessing controls on Si transfer to the ocean. *Comptes Rendus—Geoscience*, 344(11–12), 723–738. <https://doi.org/10.1016/j.crte.2012.09.006>
- Opfergelt, S., Georg, R. B., Delvaux, B., Cabidoche, Y. M., Burton, K. W., & Halliday, A. N. (2012). Silicon isotopes and the tracing of desilication in volcanic soil weathering sequences, Guadeloupe. *Chemical Geology*, 326–327, 113–122. <https://doi.org/10.1016/j.chemgeo.2012.07.032>
- Orem, C. A., & Pelletier, J. D. (2016). The predominance of post-wildfire erosion in the long-term denudation of the Valles Caldera, New Mexico. *Journal of Geophysical Research: Earth Surface*, 121, 843–864. <https://doi.org/10.1002/2015JF003663>
- Perez-Fodich, A., & Derry, L. A. (2020). A model for germanium-silicon equilibrium fractionation in kaolinite. *Geochimica et Cosmochimica Acta*, 288, 199–213. <https://doi.org/10.1016/j.gca.2020.07.046>
- Pett-Ridge, J. C. (2009). Contributions of dust to phosphorus cycling in tropical forests of the Luquillo Mountains, Puerto Rico. *Biogeochemistry*, 94(1), 63–80. <https://doi.org/10.1007/s10533-009-9308-x>
- Pokrovsky, O. S., Reynolds, B. C., Prokushkin, A. S., Schott, J., & Viers, J. (2013). Silicon isotope variations in Central Siberian rivers during basalt weathering in permafrost-dominated larch forests. *Chemical Geology*, 355, 103–116. <https://doi.org/10.1016/j.chemgeo.2013.07.016>
- Pringle, E. A., Moynier, F., Savage, P. S., Badro, J., & Barrat, J. A. (2014). Silicon isotopes in angrites and volatile loss in planetesimals. *Proceedings of the National Academy of Sciences of the United States of America*, 111(48), 17029–17032. <https://doi.org/10.1073/pnas.1418889111>
- Prokushkin, A. S., Pokrovsky, O. S., Shirokova, L. S., Korets, M. A., Viers, J., Prokushkin, S. G., et al. (2011). Sources and the flux pattern of dissolved carbon in rivers of the Yenisey basin draining the Central Siberian Plateau. *Environmental Research Letters*, 6(4). <https://doi.org/10.1088/1748-9326/6/4/045212>
- Qi, H. W., Hu, R. Z., Jiang, K., Zhou, T., Liu, Y. F., & Xiong, Y. W. (2019). Germanium isotopes and Ge/Si fractionation under extreme tropical weathering of basalts from the Hainan Island, South China. *Geochimica et Cosmochimica Acta*, 253, 249–266. <https://doi.org/10.1016/j.gca.2019.03.022>
- Rasmussen, C., Troch, P. A., Chorover, J., Brooks, P., Pelletier, J., & Huxman, T. E. (2011). An open system framework for integrating critical zone structure and function. *Biogeochemistry*, 102(1), 15–29. <https://doi.org/10.1007/s10533-010-9476-8>
- Raymond, P. A., & Sayers, J. E. (2010). Event controlled DOC export from forested watersheds. *Biogeochemistry*, 100(1), 197–209. <https://doi.org/10.1007/s10533-010-9416-7>
- Rempe, D. M., & Dietrich, W. E. (2014). A bottom-up control on fresh-bedrock topography under landscapes. *Proceedings of the National Academy of Sciences of the United States of America*, 111(18), 6576–6581. <https://doi.org/10.1073/pnas.1404763111>
- Riebe, C. S., Hahm, W. J., & Brantley, S. L. (2017). Controls on deep critical zone architecture: A historical review and four testable hypotheses. *Earth Surface Processes and Landforms*, 42(1), 128–156. <https://doi.org/10.1002/esp.4052>
- Riebe, C. S., Kirchner, J. W., & Finkel, R. C. (2003). Long-term rates of chemical weathering and physical erosion from cosmogenic nuclides and geochemical mass balance. *Geochimica et Cosmochimica Acta*, 67(22), 4411–4427. [https://doi.org/10.1016/S0016-7037\(03\)00382-X](https://doi.org/10.1016/S0016-7037(03)00382-X)
- Riebe, C. S., Kirchner, J. W., Granger, D. E., & Finkel, R. C. (2001). Strong tectonic and weak climatic control of long-term chemical weathering rates. *Geology*, 29(6), 511–514. [https://doi.org/10.1130/0091-7613\(2001\)029<0511:stawcc>2.0.co;2;2](https://doi.org/10.1130/0091-7613(2001)029<0511:stawcc>2.0.co;2;2)

- Riley, J. P., & Tongudai, M. (1967). The major cation/chlorinity ratios in sea water. *Chemical Geology*, 2(2–3), 263–269. [https://doi.org/10.1016/0009-2541\(67\)90026-5](https://doi.org/10.1016/0009-2541(67)90026-5)
- Riotte, J., Meunier, J. D., Zambardi, T., Audry, S., Barboni, D., Anupama, K., et al. (2018). Processes controlling silicon isotopic fractionation in a forested tropical watershed: Mule Hole Critical Zone Observatory (Southern India). *Geochimica et Cosmochimica Acta*, 228, 301–319. <https://doi.org/10.1016/j.gca.2018.02.046>
- Roa-García, M. C., & Weiler, M. (2010). Integrated response and transit time distributions of watersheds by combining hydrograph separation and long-term transit time modeling. *Hydrology and Earth System Sciences*, 14(8), 1537–1549. <https://doi.org/10.5194/hess-14-1537-2010>
- Roddick, J. A. (1983). Geophysical review and composition of the coast plutonic complex, south of latitude 55°N. *Memoir of the Geological Society of America*, 159(1), 195–212. <https://doi.org/10.1130/MEM159-p195>
- Roddick, J. A. (1996). Geology, Rivers Inlet (92M)—Queens Sound (102P) map areas, British Columbia. <https://doi.org/10.4095/208189>
- Roerdink, D. L., van den Boorn, S. H. J. M., Geilert, S., Vroon, P. Z., & van Bergen, M. J. (2015). Experimental constraints on kinetic and equilibrium silicon isotope fractionation during the formation of non-biogenic chert deposits. *Chemical Geology*, 402, 40–51. <https://doi.org/10.1016/j.chemgeo.2015.02.038>
- Rose, L. A., Karwan, D. L., & Godsey, S. E. (2018). Concentration-discharge relationships describe solute and sediment mobilization, reaction, and transport at event and longer timescales. *Hydrological Processes*, 32(18), 2829–2844. <https://doi.org/10.1002/hyp.13235>
- Rudnick, R. L., & Gao, S. (2013). Composition of the continental crust. *Treatise on geochemistry* (2nd ed., Vol. 4). Elsevier Ltd. <https://doi.org/10.1016/B978-0-08-095975-7.00301-6>
- Safeeq, M., & Hunsaker, C. T. (2016). Characterizing runoff and water yield for headwater catchments in the southern Sierra Nevada. *Journal of the American Water Resources Association*, 52(6), 1327–1346. <https://doi.org/10.1111/1752-1688.12457>
- Salve, R., Rempe, D. M., & Dietrich, W. E. (2012). Rain, rock moisture dynamics, and the rapid response of perched groundwater in weathered, fractured argillite underlying a steep hillslope. *Water Resources Research*, 48(11), 1–25. <https://doi.org/10.1029/2012WR012583>
- Savage, P. S., Georg, R. B., Williams, H. M., Burton, K. W., & Halliday, A. N. (2011). Silicon isotope fractionation during magmatic differentiation. *Geochimica et Cosmochimica Acta*, 75(20), 6124–6139. <https://doi.org/10.1016/j.gca.2011.07.043>
- Savage, P. S., Georg, R. B., Williams, H. M., & Halliday, A. N. (2013). The silicon isotope composition of the upper continental crust. *Geochimica et Cosmochimica Acta*, 109, 384–399. <https://doi.org/10.1016/j.gca.2013.02.004>
- Savage, P. S., Georg, R. B., Williams, H. M., Turner, S., Halliday, A. N., & Chappell, B. W. (2012). The silicon isotope composition of granites. *Geochimica et Cosmochimica Acta*, 92, 184–202. <https://doi.org/10.1016/j.gca.2012.06.017>
- Scanlon, T. M., Raffensperger, J. P., & Hornberger, G. M. (2001). Modeling transport of dissolved silica in a forested headwater catchment: Implications for defining the hydrochemical response of observed flow pathways. *Water Resources Research*, 37(4), 1071–1082. <https://doi.org/10.1029/2000WR900278>
- Schuessler, J. A., von Blanckenburg, F., Bouchez, J., Uhlig, D., & Hewawasam, T. (2018). Nutrient cycling in a tropical montane rainforest under a supply-limited weathering regime traced by elemental mass balances and Mg stable isotopes. *Chemical Geology*, 497(September), 74–87. <https://doi.org/10.1016/j.chemgeo.2018.08.024>
- Scribner, A. M., Kurtz, A. C., & Chadwick, O. A. (2006). Germanium sequestration by soil: Targeting the roles of secondary clays and Fe-oxy-hydroxides. *Earth and Planetary Science Letters*, 243(3–4), 760–770. <https://doi.org/10.1016/j.epsl.2006.01.051>
- Stallard, R. F. (1980). *Major element geochemistry of the Amazon River System* (p. 366). Retrieved from <http://hdl.handle.net/1721.1/58120>
- Stallard, R. F. (1985). River chemistry, geology, geomorphology, and soils in the Amazon and Orinoco Basins. In *The Chemistry of Weathering* (pp. 293–316). Dordrecht: Springer Netherlands. https://doi.org/10.1007/978-94-009-5333-8_17
- Stallard, R. F., & Edmond, J. M. (1981). Geochemistry of the Amazon: 1. Precipitation chemistry and the marine contribution to the dissolved load at the time of peak discharge. *Journal of Geophysical Research*, 86(C10), 9844. <https://doi.org/10.1029/JC086iC10p09844>
- Stallard, R. F., & Edmond, J. M. (1983). Geochemistry of the Amazon: 2. The influence of geology and weathering environment on the dissolved load. *Journal of Geophysical Research: Oceans*, 88(C14), 9671–9688. <https://doi.org/10.1029/JC088iC14p09671>
- Stallard, R. F., & Edmond, J. M. (1987). Geochemistry of the Amazon: 3. Weathering chemistry and limits to dissolved inputs. *Journal of Geophysical Research*, 92(C8), 8293. <https://doi.org/10.1029/JC092iC08p08293>
- Steinboeck, G., Breuer, J., von Blanckenburg, F., Horn, I., & Sommer, M. (2017). The dynamics of Si cycling during weathering in two small catchments in the Black Forest (Germany) traced by Si isotopes. *Chemical Geology*, 466(January), 389–402. <https://doi.org/10.1016/j.chemgeo.2017.06.026>
- Stewart, B. W., Capo, R. C., & Chadwick, O. A. (2001). Effects of rainfall on weathering rate, base cation provenance, and Sr isotope composition of Hawaiian soils. *Geochimica et Cosmochimica Acta*, 65(7), 1087–1099. [https://doi.org/10.1016/S0016-7037\(00\)00614-1](https://doi.org/10.1016/S0016-7037(00)00614-1)
- St. Pierre, K. A., Hunt, B. P. V., Tank, S. E., Giesbrecht, I., Korver, M. C., Floyd, W. C., et al. (2021). Rain-fed streams dilute inorganic nutrients but subsidise organic-matter-associated nutrients in coastal waters of the northeast Pacific Ocean. *Biogeosciences*, 18(10), 3029–3052. <https://doi.org/10.5194/bg-18-3029-2021>
- Street-Perrott, F. A., & Barker, P. A. (2008). Biogenic silica: A neglected component of the coupled global continental biogeochemical cycles of carbon and silicon. *Earth Surface Processes and Landforms*, 33, 1436–1457. <https://doi.org/10.1002/esp.1712>
- Sun, L., Wu, L. H., Ding, T. P., & Tian, S. H. (2008). Silicon isotope fractionation in rice plants, an experimental study on rice growth under hydroponic conditions. *Plant and Soil*, 304(1–2), 291–300. <https://doi.org/10.1007/s11104-008-9552-1>
- Sun, Y., Wu, L. H., & Li, X. Y. (2016). Experimental determination of silicon isotope fractionation in rice. *PLoS ONE*, 11(12), 1–12. <https://doi.org/10.1371/journal.pone.0168970>
- Tetzlaff, D., Birkel, C., Dick, J., Geris, J., & Soulsby, C. (2014). Storage dynamics in hydropedological units control hillslope connectivity, runoff generation, and the evolution of catchment transit time distributions. *Water Resources Research*, 50(2), 969–985. <https://doi.org/10.1002/2013WR014147>
- Thompson, S. D., Nelson, T. A., Giesbrecht, I., Frazer, G., & Saunders, S. C. (2016). Data-driven regionalization of forested and non-forested ecosystems in coastal British Columbia with LiDAR and RapidEye imagery. *Applied Geography*, 69, 35–50. <https://doi.org/10.1016/j.apgeog.2016.02.002>
- Thompson, S. E., Basu, N. B., Lascurain, J., Aubeneau, A., & Rao, P. S. C. (2011). Relative dominance of hydrologic versus biogeochemical factors on solute export across impact gradients. *Water Resources Research*, 47(7), 1–20. <https://doi.org/10.1029/2010WR009605>
- Tipper, E. T., Calmels, D., Gaillardet, J., Louvat, P., Capmas, F., & Dubacq, B. (2012). Positive correlation between Li and Mg isotope ratios in the river waters of the Mackenzie Basin challenges the interpretation of apparent isotopic fractionation during weathering. *Earth and Planetary Science Letters*, 333–334. <https://doi.org/10.1016/j.epsl.2012.04.023>
- Troch, P. A., Broxton, P., Zapata-Rios, X., Losleben, M., & Durcik, M. (2021). CJCZO—Streamflow/discharge—Jemez River Basin—(2007–2021). HydroShare. Retrieved from <http://www.hydroshare.org/resource/c0e5094d1de54547a304d4dec3a7b3ff>

- Troch, P. A., Lahmers, T., Meira, A., Mukherjee, R., Pedersen, J. W., Roy, T., & Valdés-Pineda, R. (2015). Catchment coevolution: A useful framework for improving predictions of hydrological change? *Water Resources Research*, 51, 4903–4922. <https://doi.org/10.1029/2015wr017032>
- Tune, A. K., Druhan, J. L., Wang, J., Bennett, P. C., & Rempe, D. M. (2020). Carbon dioxide production in bedrock beneath soils substantially contributes to forest carbon cycling. *Journal of Geophysical Research: Biogeosciences*, 125(12), 1–13. <https://doi.org/10.1029/2020JG005795>
- Uhlig, D., Schuessler, J. A., Bouchez, J., Dixon, J. L., & Von Blanckenburg, F. (2017). Quantifying nutrient uptake as driver of rock weathering in forest ecosystems by magnesium stable isotopes. *Biogeosciences*, 14(12), 3111–3128. <https://doi.org/10.5194/bg-14-3111-2017>
- National Water Information System data available on the World Wide Web (USGS Water Data for the Nation). U.S. Geologic Survey. <https://doi.org/10.5066/F7P55KJN>
- Van Den Boorn, S. H. J. M., Vroon, P. Z., Van Belle, C. C., Van Der Wagt, B., Schwieters, J., & Van Bergen, M. J. (2006). Determination of silicon isotope ratios in silicate materials by high-resolution MC-ICP-MS using a sodium hydroxide sample digestion method. *Journal of Analytical Atomic Spectrometry*, 21(8), 734–742. <https://doi.org/10.1039/b600933f>
- Van der Hoven, S. J., & Quade, J. (2002). Tracing spatial and temporal variations in the sources of calcium in pedogenic carbonates in a semiarid environment. *Geoderma*, 108(3–4), 259–276. [https://doi.org/10.1016/S0016-7061\(02\)00134-9](https://doi.org/10.1016/S0016-7061(02)00134-9)
- Van Der Velde, Y., Torfs, P. J. J. F., Van Der Zee, S. E. A. T. M., & Uijlenhoet, R. (2012). Quantifying catchment-scale mixing and its effect on time-varying travel time distributions. *Water Resources Research*, 48(6), 1–13. <https://doi.org/10.1029/2011WR011310>
- Vázquez-Ortega, A., Perdrial, J., Harpold, A., Zapata-Ríos, X., Rasmussen, C., McIntosh, J., et al. (2015). Rare earth elements as reactive tracers of biogeochemical weathering in forested rhyolitic terrain. *Chemical Geology*, 391, 19–32. <https://doi.org/10.1016/j.chemgeo.2014.10.016>
- Vet, R., Artz, R. S., Carou, S., Shaw, M., Ro, C. U., Aas, W., et al. (2014). A global assessment of precipitation chemistry and deposition of sulfur, nitrogen, sea salt, base cations, organic acids, acidity and pH, and phosphorus. *Atmospheric Environment*, 93, 3–100. <https://doi.org/10.1016/j.atmosenv.2013.10.060>
- West, A. J., Galy, A., & Bickle, M. (2005). Tectonic and climatic controls on silicate weathering. *Earth and Planetary Science Letters*, 235(1–2), 211–228. <https://doi.org/10.1016/j.epsl.2005.03.020>
- White, A., Moravec, B., McIntosh, J., Olshansky, Y., Paras, B., Sanchez, R. A., et al. (2019). Storage and routing of water in the deep critical zone of a snow dominated volcanic catchment. *Hydrology and Earth System Sciences Discussions*, 1–38. <https://doi.org/10.5194/hess-2019-140>
- White, A. F., & Blum, A. E. (1995). Effects of climate on chemical weathering in watersheds. *Water-Rock Interaction. Proc. Symposium, Vladivostok*, 59(9), 57–60. <https://doi.org/10.1201/9780203734049-13>
- White, A. F., Blum, A. E., Bullen, T. D., Vivit, D. V., Schulz, M., & Fitzpatrick, J. (1999). The effect of temperature on experimental and natural chemical weathering rates of granitoid rocks. *Geochimica et Cosmochimica Acta*, 63(19–20), 3277–3291. [https://doi.org/10.1016/S0016-7037\(99\)00250-1](https://doi.org/10.1016/S0016-7037(99)00250-1)
- White, T., Brantley, S., Banwart, S., Chorover, J., Dietrich, W., Derry, L., et al. (2015). *The role of critical zone observatories in critical zone science. Developments in earth surface processes* (Vol. 19). Elsevier B.V. <https://doi.org/10.1016/B978-0-444-63369-9.00002-1>
- Wiederhold, J. G. (2015). Metal stable isotope signatures as tracers in environmental geochemistry. *Environmental Science and Technology*, 49(5), 2606–2624. <https://doi.org/10.1021/es504683e>
- Wilcock, J., Goff, F., Minarik, W. G., & Stix, J. (2013). Magmatic recharge during the formation and resurgence of the Valles Caldera, New Mexico, USA: Evidence from quartz compositional zoning and geothermometry. *Journal of Petrology*, 54(4), 635–664. <https://doi.org/10.1093/petrology/egs078>
- Włostowski, A. N., Molotch, N., Anderson, S. P., Brantley, S. L., Chorover, J., Dralle, D., et al. (2021). Signatures of hydrologic function across the critical zone observatory network. *Water Resources Research*, 57(3). <https://doi.org/10.1029/2019WR026635>
- Yanhe, L., Tiping, D., & Defang, W. (1995). Experimental study of silicon isotope dynamic fractionation and its application in geology. *Chinese Journal of Geochemistry*, 14(3), 212–219. <https://doi.org/10.1007/BF02842044>
- Yoon, B., & Raymond, P. A. (2012). Dissolved organic matter export from a forested watershed during Hurricane Irene. *Geophysical Research Letters*, 39(17), 1–6. <https://doi.org/10.1029/2012GL052785>
- Zahibo, N., Pelinovsky, E., Talipova, T., Rabinovich, A., Kurkin, A., & Nikolkina, I. (2007). Statistical analysis of cyclone hazard for Guadeloupe, Lesser Antilles. *Atmospheric Research*, 84(1), 13–29. <https://doi.org/10.1016/j.atmosres.2006.03.008>
- Zapata-Ríos, X., McIntosh, J., Rademacher, L., Troch, P. A., Brooks, P. D., Rasmussen, C., & Chorover, J. (2015). Climatic and landscape controls on water transit times and silicate mineral weathering in the critical zone. *Water Resources Research*, 51(8), 6036–6051. <https://doi.org/10.1002/2015WR017018>
- Ziegler, K., Chadwick, O. A., Brzezinski, M. A., & Kelly, E. F. (2005). Natural variations of ^{83}Si ratios during progressive basalt weathering, Hawaiian Islands. *Geochimica et Cosmochimica Acta*, 69(19), 4597–4610. <https://doi.org/10.1016/j.gca.2005.05.008>
- Ziegler, K., Chadwick, O. A., White, A. F., & Brzezinski, M. A. (2005). ^{83}Si systematics in a granitic saprolite, Puerto Rico. *Geology*, 33(10), 817–820. <https://doi.org/10.1130/G21707.1>